

Copyright
by
Robert James Rabb
2007

The Dissertation Committee for Robert James Rabb
certifies that this is the approved version of the following dissertation:

**A Mesomechanical Particle-Element Model of Impact
Dynamics in Neat and Shear Thickening Fluid Kevlar**

Committee:

Eric P. Fahrenthold, Supervisor

Jeffrey K. Bennighof

Michael D. Bryant

Richard H. Crawford

Alfred E. Traver

**A Mesomechanical Particle-Element Model of Impact
Dynamics in Neat and Shear Thickening Fluid Kevlar**

by

Robert James Rabb, B.S.; M.S.E.

DISSERTATION

Presented to the Faculty of the Graduate School of
The University of Texas at Austin
in Partial Fulfillment
of the Requirements
for the Degree of

DOCTOR OF PHILOSOPHY

THE UNIVERSITY OF TEXAS AT AUSTIN

August 2007

Dedicated to my family.

Acknowledgments

I wish to thank the many people who helped me. Time would fail me to tell of all the assistance received from my advisor, Dr. Eric P. Fahrenthold, for his guidance, insight, and encouragement throughout this journey. His patience and understanding have been tremendous. I would also like to thank the members of my dissertation committee for their service: Dr. Jeffrey K. Bennighof, Dr. Michael D. Bryant, Dr. Richard H. Crawford, and Dr. Alfred E. Traver.

I would like to thank the Office of Naval Research and NASA Johnson Space Center for their support of this research.

Special gratitude is extended to Dr. Eric Wetzel with the Army Research Laboratory, Weapons and Materials Research Directorate for his preparation of STF Kevlar and insight to this area of research and to Don Grosch, Explosives and Ballistics Range Manager at Southwest Research Institute, for his time and assistance in the impact experiments.

I also express my appreciation to the Texas Advanced Computing Center at the University of Texas at Austin and the Arctic Region Supercomputing Center at the University of Alaska Fairbanks for their generous computer time support.

Finally, I wish to thank BG (Ret.) Kip Nygren and COL (Ret.) Wayne

Whiteman, Department of Civil and Mechanical Engineering, United States Military Academy, for allowing me to attend graduate school and pursue this degree. Their support and recommendations have allowed the U.S. Army to fund this degree program.

A Mesomechanical Particle-Element Model of Impact Dynamics in Neat and Shear Thickening Fluid Kevlar

Publication No. _____

Robert James Rabb, Ph.D.
The University of Texas at Austin, 2007

Supervisor: Eric P. Fahrenthold

Advanced impact protection systems can experience serious damage due to contact with projectiles such as fragments or entire fan blades. To prevent catastrophic damage of such systems will require sophisticated materials and complex designs. The development of advanced ballistic protection systems will place increased emphasis on the use of composite materials and on numerical simulations to assess these new systems due to the cost and limitations of testing facilities and the increased capability of computing power. Example applications include the design of body armor for the protection of personnel, the design of fragment containment systems for aircraft engines, and the design of orbital debris shielding for the protection of manned spacecraft. The current research has developed a new mesomechanical particle-element material model for woven material impact response, a velocity dependent friction model to simulate yarn interactions, and a strain rate dependent model for Kevlar. In recent research, a new class of shear-thickening fluid (STF)

composites has been developed for use in impact protection systems. Advancements in the current work include a Bingham shear stress model for STF effects and a new mixture equation of state for the STF Kevlar that captures the thermodynamic properties of the constituents. The numerical methods and material model developed in this research have been validated through the simulation of three dimensional impact experiments on different Kevlar target geometries. This dissertation also provides new data for fragment simulating projectile impacts on Kevlar with different boundary conditions and new data for aluminum cylinder and steel disk projectile impacts on neat and STF Kevlar with different boundary conditions.

Table of Contents

Acknowledgments	v
Abstract	vii
List of Tables	xii
List of Figures	xiv
Chapter 1. Introduction	1
1.1 Introduction	1
1.2 Motivation	2
1.3 Scope of the Research	5
1.3.1 Experiments	5
1.3.2 Numerical Methods Development	5
1.3.3 Material Model Development	6
1.3.4 Validation Simulations	7
1.4 Dissertation Organization	8
Chapter 2. Fragment Simulating Projectile Impact Tests and Analysis of Neat Kevlar	11
2.1 Introduction	11
2.2 Materials	13
2.2.1 Kevlar	13
2.2.2 Projectile	14
2.3 Target Preparation and Experimental Procedure	14
2.4 Results of Impact Experiments	16
2.5 Analysis and Scaling	18
2.5.1 Two Fixed / Two Free Edges Experiments	18
2.5.2 Clamped Edges Experiments	21

2.5.3	Boundary Conditions	22
2.6	Summary	23
Chapter 3. Comparison and Analysis of Neat and Shear Thickening Fluid Kevlar Impacts		49
3.1	Introduction	49
3.2	Materials	52
3.2.1	Kevlar	52
3.2.2	Shear Thickening Fluid	52
3.2.3	Projectiles	53
3.3	Target Preparation and Experimental Procedure	53
3.4	Results of Ballistic Experiments	56
3.5	Analysis	57
3.5.1	Aluminum Cylinder Impact Experiments with Clamped Edges	57
3.5.2	Aluminum Cylinder Impact Experiments with Two Clamped and Two Free Edges	58
3.5.3	Steel Disk Impact Experiments with Clamped Edges	59
3.5.4	Boundary Conditions	60
3.6	Summary	61
Chapter 4. Development and Validation of a Hybrid Particle-Element Mesomechanical Model for Kevlar Fabric		82
4.1	Introduction	82
4.2	Geometry	88
4.2.1	Modeled Yarn Geometry	90
4.2.2	Modeled Particle Geometry	93
4.3	Particle Kinematics	96
4.4	Potential Energy	97
4.5	Failure Criteria	100
4.6	Irreversible Entropy Production	102
4.7	Equation of State	103
4.8	Rate Dependent Strength Model	105
4.9	Simulation Results	106
4.10	Summary	108

Chapter 5. Development and Validation of a Particle-Element Model for Shear Thickening Fluid (STF) Treated Kevlar Fabric	127
5.1 Introduction	127
5.2 Mixture Equation of State	130
5.2.1 Mass Fractions of the Constituents	131
5.2.2 Internal Energy Equation	132
5.3 Velocity Dependent Friction Model	135
5.4 Bingham Fluid Model	139
5.5 Irreversible Entropy Production	141
5.6 Seventh Order Polynomial Mie-Gruneisen Equation of State .	142
5.7 Simulation Results	143
5.7.1 Aluminum Cylinder Projectile	144
5.7.2 Steel Disk Projectile	146
5.7.3 Multilayer Model	147
5.8 Summary	148
Chapter 6. Conclusion	168
Appendices	172
Appendix A. Residual Velocity Correlation for the FSP Impact Experiments	173
Appendix B. Strain Rate Dependent Strength Model	175
Bibliography	178
Vita	196

List of Tables

2.1	Style 706 Kevlar fabric construction specifications	25
2.2	Experimental results: FSP impacts on two fixed and two free edges of neat Kevlar	26
2.3	Experimental results: FSP impacts on clamped edges of neat Kevlar	27
2.4	Residual velocity equation parameters for the FSP experimental data	28
3.1	Properties of STF Kevlar constituents used in experiments . .	63
3.2	Experimental results: aluminum cylinder impacts on neat and STF Kevlar with all edges clamped	63
3.3	Experimental results: aluminum cylinder impacts on neat and STF Kevlar with two edges clamped and two edges free	64
3.4	Experimental results: steel disk impacts on neat and STF Kevlar with all edges clamped	64
4.1	Material properties used in the FSP impact simulations	110
4.2	Kevlar KM-2 tensile strength data	111
4.3	Mechanical properties of Kevlar KM-2 yarn as a function of strain rate	111
4.4	Simulation results: FSP impacts on two fixed and two free edges of neat Kevlar	112
5.1	Coefficients for a seven term polynomial Mie-Gruneisen equation of state for silica	150
5.2	Material properties used in the STF impact simulations	151
5.3	Simulation results: aluminum cylinder impacts on neat and STF Kevlar with two edges clamped and two edges free	152
5.4	Simulation results: steel disk impacts on neat and STF Kevlar with all edges clamped	152
5.5	Simulation results: aluminum cylinder impacts on multiple layers modeled as a single layer	153

5.6	Computer resource requirements for the aluminum cylinder impact simulations	153
5.7	Computer resource requirements for the steel disk impact simulations	154

List of Figures

2.1	Fragment simulating projectile	29
2.2	Target frame for the Kevlar with clamped edges	30
2.3	Cinch buckles for mounting the Kevlar in the two fixed and two free edges experiments	31
2.4	Target frame for the Kevlar with two fixed and two free edges	32
2.5	Experimental setup for FSP impact tests	33
2.6	Post-impact damage for one layer of Kevlar with two fixed and two free edges	34
2.7	Images for a FSP impact at 297 <i>m/s</i> on one layer of Kevlar with two fixed and two free edges	35
2.8	Experimental results: FSP impacts on one layer of Kevlar with two fixed and two free edges	36
2.9	Experimental results: FSP impacts on two layers of Kevlar with two fixed and two free edges	37
2.10	Experimental results: FSP impacts on four layers of Kevlar with two fixed and two free edges	38
2.11	Experimental results: FSP impacts on Kevlar with two fixed and two free edges	39
2.12	Post-impact damage for one layer of Kevlar with clamped edges	40
2.13	Images for a FSP impact at 340 <i>m/s</i> on two layers of Kevlar with clamped edges	41
2.14	Experimental results: FSP impacts on one layer of Kevlar with clamped edges	42
2.15	Experimental results: FSP impacts on two layers of Kevlar with clamped edges	43
2.16	Experimental results: FSP impacts on four layers of Kevlar with clamped edges	44
2.17	Experimental results: FSP impacts on Kevlar with clamped edges	45
2.18	Comparison of FSP impacts on one layer of Kevlar with two fixed/two free edges and clamped edges	46

2.19	Comparison of FSP impacts on two layers of Kevlar with two fixed/two free edges and clamped edges	47
2.20	Comparison of FSP impacts on four layers of Kevlar with two fixed/two free edges and clamped edges	48
3.1	Softwall fan containment system concept	65
3.2	Target frame for the aluminum cylinder and steel disk impact tests on Kevlar with clamped edges	66
3.3	Southwest Research Institute (SwRI) compressed gas gun . . .	67
3.4	Sabot trap with a steel disk projectile sabot	68
3.5	Aluminum cylinder projectile and polystyrene sabot	69
3.6	Steel disk projectile and Noryl sabot	70
3.7	Experimental setup for the STF impact tests	71
3.8	Post-impact damage by a steel disk projectile	72
3.9	Yarn damage from an aluminum cylinder projectile impact on one layer of neat Kevlar	73
3.10	Yarn damage from an aluminum cylinder projectile impact on one layer of STF Kevlar	74
3.11	STF debris cloud from an aluminum cylinder projectile impact	75
3.12	Comparison of aluminum cylinder impacts on neat and STF Kevlar with all clamped edges	76
3.13	Images of an aluminum cylinder impact at 367 <i>m/s</i> on two layers of STF Kevlar with all clamped edges	77
3.14	Comparison of aluminum cylinder impacts on neat and STF Kevlar with two clamped and two free edges	78
3.15	Images of an aluminum cylinder impact at 298 <i>m/s</i> on one layer of STF Kevlar with two clamped and two free edges	79
3.16	Comparison of steel disk impacts on neat and STF Kevlar with all clamped edges	80
3.17	Images of a steel disk impact at 294 <i>m/s</i> on three layers of STF Kevlar with all clamped edges	81
4.1	Hybrid Particle-Element Method	113
4.2	Hexcel Schwebel Style 706 fabric, Kevlar KM-2 fiber, 600 denier, 400 fibers per yarn, 34 yarns per inch	114
4.3	Crimp in Kevlar KM-2 yarn after removal from the woven fabric	114

4.4	Kevlar KM-2 yarn model	115
4.5	Simulation results: FSP impacts on one layer of two fixed and two free edges of neat Kevlar	116
4.6	Simulation results: FSP impacts on two layers of two fixed and two free edges of neat Kevlar	117
4.7	Simulation results: FSP impacts on four layers of two fixed and two free edges of neat Kevlar	118
4.8	FSP impact simulation at 300 <i>m/s</i> on one layer of Kevlar with two fixed and two free edges at 0 μsec	119
4.9	FSP impact simulation at 300 <i>m/s</i> on one layer of Kevlar with two fixed and two free edges at 50 μsec after impact	120
4.10	FSP impact simulation at 300 <i>m/s</i> on one layer of Kevlar with two fixed and two free edges at 100 μsec after impact	121
4.11	FSP impact experiment at 297 <i>m/s</i> on one layer of Kevlar with two fixed and two free edges at 0 - 100 μsec after impact	122
4.12	FSP impact simulation at 400 <i>m/s</i> on four layers of Kevlar with two fixed and two free edges at 0 μsec	123
4.13	FSP impact simulation at 400 <i>m/s</i> on four layers of Kevlar with two fixed and two free edges at 93 μsec after impact	124
4.14	FSP impact simulation at 400 <i>m/s</i> on four layers of Kevlar with two fixed and two free edges at 120 μsec after impact	125
4.15	FSP impact experiment at 386 <i>m/s</i> on four layers of Kevlar with two fixed and two free edges at 0 - 120 μsec after impact	126
5.1	Velocity dependent friction model	155
5.2	Experiment and simulation results: aluminum cylinder impacts on neat targets	156
5.3	Experiment and simulation results: aluminum cylinder impacts on STF targets	157
5.4	Aluminum cylinder impact simulation at 303 <i>m/s</i> on two layers of STF Kevlar with two clamped and two free edges at 0 μsec	158
5.5	Aluminum cylinder impact simulation at 303 <i>m/s</i> on two layers of STF Kevlar with two clamped and two free edges at 73 μsec after impact	159
5.6	Aluminum cylinder impact simulation at 303 <i>m/s</i> on two layers of STF Kevlar with two clamped and two free edges at 138 μsec after impact	160

5.7	Aluminum cylinder impact experiment at 303 m/s on two layers of STF Kevlar with two clamped and two free edges at 125 μsec after impact	161
5.8	Experiment and simulation results: steel disk impacts on neat targets	162
5.9	Experiment and simulation results: steel disk impacts on STF targets	163
5.10	Steel disk impact simulation at 296 m/s on three layers of neat Kevlar with clamped edges at 0 μsec	164
5.11	Steel disk impact simulation at 296 m/s on three layers of neat Kevlar with clamped edges at 110 μsec after impact	165
5.12	Steel disk impact simulation at 296 m/s on three layers of neat Kevlar with clamped edges at 188 μsec after impact	166
5.13	Steel disk impact experiment at 296 m/s on three layers of neat Kevlar with clamped edges at 200 μsec after impact	167
B.1	Strain and failure strain versus time for a constant strain rate test	177
B.2	Normalized failure strain versus strain rate for a constant strain rate test	177

Chapter 1

Introduction

1.1 Introduction

Various high velocity contact-impact events attract much mechanical engineering interest and are difficult to model and simulate. Debris impacts against flying structures, vehicular collisions, and bullet impacts against various targets can be included in this general area of engineering concern. Bullet and fragmentation impacts against ballistic textiles are different from many other impact events due to the energy concentrated at the relatively small projectile area and the physical properties of the textile targets [71]. The ballistic textiles, usually referred to under the trade names as Kevlar, Twaron, and Spectra to name a few, are shaped and sewn as a protective outerwear and must protect the wearer from a penetrating bullet or fragment as well as reduce blunt force trauma from the impact. In order to protect military and law enforcement personnel from high energy bullets and fragments, new materials and designs must be developed to provide better protection while allowing the wearer to move in response to threat conditions.

Many studies have examined ballistic impacts on various textiles over the last several decades [18, 85, 86]. Simulation and modeling of ballistic im-

pacts on textiles such as Kevlar is complex due to the detailed mesoscale modeling of the textile geometry and textile composition [93, 120]. Simulation and modeling of the ballistic impact response of Kevlar is a nontrivial matter due to the cost of developing new varieties of ballistic materials, the constraints and availability of experimental facilities, and the advancements in computer capability. Additionally, advanced body armor design often features multilayer Kevlar geometry, and new developments in aircraft engine containment systems may include the possible treatment of the Kevlar with shear thickening fluid (STF).

1.2 Motivation

Current computational tools [9, 31, 47, 76, 108, 119] used to evaluate the ballistic performance of body armor lack the material models and/or kinematics required for virtual prototyping of advanced body armor technology. At the fabric level, membrane models such as those used by Lim et al. [63] and Phoenix [83] cannot account for yarn interactions. These membrane models treat the fabric as continuum of finite elements and lack the details of the intricate weave pattern of the yarns. Another method used to model fabric includes a pure particle model [76]. This method represents the fabric as an assembly of geometrically spaced particles. Like membrane models, this approach does not represent the medium at the yarn level but captures the bulk response of the fabric.

On the other hand, yarn level models can replicate the weave pattern

of particular fabrics. Finite element models (FEM) such as those used by Duan et al. [31], Raftenberg [87], and Shockey et al. [100] often employ hex elements at the yarn level in commercial packages such as LS-DYNA3D. However, these hex elements have inherent bending stiffness problems for the modeled yarn. Finite element models representing the individual yarn as a membrane [9] cannot capture detailed yarn dynamics. Another FEM approach is to employ bar elements to represent the yarns, but these models represent the yarn crossovers with pin-joints [47] or springs [25], neglecting the sliding interface between the yarns. These finite element models also have slideline and mass and energy discard issues associated with failed elements that may be important on multiple layer geometries. More recently, digital element analysis (DEA) [19, 119] has been introduced to represent the yarns as multiple fibers, but no published validation results exist. Although DEA appears promising, it currently lacks a thermo-mechanical formulation.

Recent research [46, 78, 97] has developed an alternative numerical approach. The hybrid particle-element technique described by Shivarama and Fahrenthold [97], Park and Fahrenthold [78], and Horban and Fahrenthold [46] employs particles and hex elements in tandem, to model high velocity impact effects in complex materials. It provides a true Lagrangian description of all material strength effects, including large strain elastic-plastic deformation and fracture. Unlike finite element methods [42], it incorporates a general description of all contact-impact effects, without the introduction of slidelines or interface tracking algorithms which hinder the application of alternative

numerical simulation techniques. Mass diffusion and strength modeling problems of Eulerian methods are avoided [68]. Additionally, tensile instability and numerical fracture problems of pure particle methods are avoided and no particle-to-element mapping algorithms are necessary [10, 106]. However, this method does not include the mesomechanical geometry to capture the inter-yarn interaction necessary in this class of contact-impact events, nor does it describe STF composites in terms of the individual STF component properties.

Advanced composites offer opportunities for significant improvements in impact protection systems. An important example is in the development of improved body armor for personnel protection in law enforcement and military applications. Next generation body armor must be light and flexible for general wear and to provide full body protection. The Office of Technology Assessment reported that wearing body armor has saved approximately 30 police officers each year from fatal gunshot wounds, and that most police officers who do not wear their body armor complain that body armor is heavy, stiff, and generally uncomfortable [111]. Additionally, softwall containment systems for aircraft engines can benefit from the impact protection and lightweight characteristics of advanced composites. Research to date indicates that significant improvements in impact protection may come from the introduction of shear-thickening fluid (STF) composites [72]. It is essential to model advanced composite materials for impact protection systems. However, it is also necessary to develop the mesomechanical model of the fabric architecture and capture the yarn geometry to accurately assess the ballistic performance.

1.3 Scope of the Research

The research built upon numerical methods and parallel code development work completed in previous research by Park and Fahrenthold [78]. The research extended the latter work by developing a new mesomechanical particle-element model and a new composite material model for use in the simulation of ballistic impact problems.

1.3.1 Experiments

The first task was to obtain impact test data. Impact and residual velocities were measured using different projectile and target geometries. These measurements were used to assess the effectiveness of the material and provided a database of different projectile and target geometries. Simulations could be validated with these experimental correlations.

1.3.2 Numerical Methods Development

The next task was the development of particle-bar elements, for use in impact simulation. The work employed the particle-elements in a three dimensional hybrid particle-element code. Particles modeled all contact-impact, thermodynamics, and inertia, while the elements modeled all strength effects to include tensile inter-particle forces. Unlike previous work which employed hex elements [78], an advancement in this application was to incorporate bar elements to represent the woven fabric model in the code and capture the mesoscale architecture of the Kevlar fabric used in impact protection sys-

tems. A layer of Kevlar was modeled by weaving together the particle-bar elements, replicating the Kevlar yarn crimp and geometry. Multiple layers of these particle-bar elements were superimposed, and their interaction modeled to simulate multiple layers of impact protection. Additionally, the particles were modeled as ellipsoids, whose geometry was a function of specific yarn parameters. Next, a velocity dependent friction model was developed for the yarn-yarn and projectile-yarn interactions. The particles and bar elements were used together to model the three dimensional kinematics of yarn interactions. A particle-element formulation has several advantages in this application, cited previously. The unique Hamiltonian method used to develop the formulation was well suited for application to STF composite modeling problems.

1.3.3 Material Model Development

The third task was the development of a rate dependent material model for the Kevlar yarn and shear thickening fluid (STF) composites. Ballistic impacts involve high strain rate loading, so a material model parameter dependence on strain rate is important in order to predict system performance. Unlike previous research that has accounted for STF effects by friction [107, 114], the new material model employs a Bingham shear stress model using experimental STF data. The material model describes the rate dependent strength and viscosity of the STF composite in terms of physical properties of the material constituents at the sub-continuum scale. In the case of STF composites,

the principal subscale variables are the fiber mechanical and thermal properties, the yarn diameter, aspect ratio, crimp, and the fiber volume fraction. The effect of these variables on the strength and viscosity of the composite was established by embedding published experimental data on STF composites in a thermodynamically consistent framework. The general material model was applied in a transient three dimensional computer code for the simulation of impact experiments. Of particular concern in this work, for their effect on the impact performance of the fluid-solid composite, were rate dependent strength and friction as well as the thermomechanical response under adiabatic compression.

1.3.4 Validation Simulations

The last task was application and validation of the mesomechanical particle-element model and material model, via simulation of tests conducted by Southwest Research Institute (SwRI). General simulation work of this type required a three dimensional impact code and an efficient and portable parallel implementation. The code employed here was based on a highly portable OpenMP-MPI implementation. It had been validated in a variety of engineering applications, including ordnance impacts. The particle-element method used here also had been applied with success to model hypervelocity impact effects on various materials, using hex elements, in previous research focused on orbital debris shielding [78]. Validation included simulation of experiments with impacts of three different types of projectiles on varying layers of neat

and STF Kevlar targets.

1.4 Dissertation Organization

The different components of this work are: (i) development, conduct, and analysis of impact experiments on neat Kevlar to include the design of the target fixture, (ii) development, conduct, and analysis of impact experiments on STF Kevlar, (iii) development of a new hybrid particle-element model for woven ballistic textile and validation of the model via simulation, and (iv) development of a new material model for rate dependent neat and STF Kevlar and validation of the overall model with simulation. Accordingly, the remaining chapters of this dissertation are organized as follows:

Chapter 2 describes a series of experiments conducted at Southwest Research Institute (SwRI) to obtain data on impact phenomena. Specifically, targets consisted of one, two, and four layers of neat Kevlar with two different types of boundary conditions. The targets were impacted by fragment simulating projectiles (FSP) with various velocities to obtain corresponding residual velocities. Analysis of the experimental results concluded in a general equation relating the residual velocity of the FSP to the impact velocity and number of layers. This correlation was used to validate future simulations. A comparison of the results showed boundary conditions affect the overall performance of the Kevlar targets.

Chapter 3 describes a series of experiments conducted at Southwest Research Institute (SwRI) to obtain data on STF Kevlar and for comparison

to neat Kevlar. Specifically, the targets consisted of differing layers of neat and STF Kevlar and were impacted by aluminum cylinder and steel disk projectiles. Comparisons were made of the neat and STF Kevlar performance. A comparison of the aluminum cylinder impacts shows the effect of different boundary conditions. The results of these experiments were used to validate the simulations.

Chapter 4 describes the mesoscale model for Kevlar fabric and the numerical development of the new yarn level model. The numerical method utilized a hybrid-particle finite element formulation and a parallel computer code specifically tailored to model the ballistic event. An extension of previous work introduced particle-bar elements rather than particle-hex elements. The formulation used ellipsoid shaped particles for the Kevlar and captured the mesoscale geometry of the woven yarn including the yarn crimp and the contact-impact dynamics of the ballistic event. Additionally, a rate dependent strength model specifically developed for the Kevlar was employed. The material model was validated in three dimensional simulations of impact experiments over a wide range of velocities and on multiple layers of fabric. A residual velocity correlation, developed in Chapter 2, was used for the validation.

Chapter 5 describes further advancement to the model by incorporating STF components in the target material. The development of a mixture equation of state allowed the problem to be solved without the introduction of additional thermodynamic internal state variables. The formulation used

an equation of state requiring constituent properties only for input. This approach was developed to deal with the STF Kevlar but is applicable to a wide range of composites. Additionally, a rate dependent friction model was employed to capture the yarn interactions as well as a Bingham fluid model to model STF effects. The model can be used to simulate other friction models such as coulomb and viscous friction and is not specific to STF composites. The model was validated in simulations of experiments with aluminum cylinder and steel disk impacts on multiple layers of neat and STF Kevlar.

Chapter 6 presents a summary of the work completed and recommendations for future work.

Chapter 2

Fragment Simulating Projectile Impact Tests and Analysis of Neat Kevlar

2.1 Introduction

Advanced body armor construction is often an arrangement of composite materials assembled in multiple layers that are encased in an outer cover [69]. An example of this arrangement is the “bulletproof vest” or “flak vest” commonly used by law enforcement and military organizations. Kevlar is one of the most widely used soft, ballistic materials with applications in these areas, although other fabrics such as Spectra and Twaron are also generating interest in these applications [34, 95, 107, 117]. Increased ballistic protection from these fabrics can be realized through more layers, but it also increases the weight of the system and decreases the mobility of the wearer. Until recently, much of the ballistic textile development has evolved from experiments. Modeling and simulating ballistic impact effects on these designs and materials are difficult, due to both the geometry and the material composition. Although the yarns used in these fabrics behave elastically in tension, the woven nature of the fabric allows for large displacements even though the individual yarn strains are small. This large displacement capability provides the fabric with a resistive capability to absorb a large amount of energy [49]. The pro-

cesses of yarn axial tension and out of plane deformation (displacement along the projectile trajectory) both contribute to the spatial extension of the load transmitted and to energy loss from the projectile. Additionally, composite materials used in protective armor design can cause difficulties for simulation when one must consider: (a) the mechanical response of the composite material may be only described by existing, incomplete material property databases, and (b) the increased number of state variables required for numerical simulation of nonhomogeneous or anisotropic materials [36, 104]. However, there is much interest in developing mathematical models to simulate the behavior of the different types of fabric armor since these models make it easier to evaluate new concepts, and computational resources offer a more rapid assessment of armor materials and designs. The savings in time and materials required for testing is clear [12].

Regardless of the difficulties, simulation of ballistic impacts on Kevlar fabric is of engineering interest due to Kevlar's effectiveness as a flexible, soft armor system. In order to model the behavior of Kevlar fabric under ballistic loading and validate the model through simulation, an understanding of Kevlar's ballistic response was necessary through a series of experiments. The present work describes a systematic series of experiments conducted to analyze the ballistic impact performance of Hexcel Schwebel Style 706 fabric (Kevlar KM-2 fiber, 600 denier, 400 fibers per yarn, 34 yarns per inch) and for validation of future simulations. Denier refers to the unit of linear density, equal to the mass in grams of 9000 m of textile strand [4]. Simulations are a valuable

tool as an adjunct to experimental work when testing facilities and resources are expensive or have limited availability. With this experimental setup, the impact velocity and residual velocity (remaining projectile velocity after penetration of the target) were easily measured, and the projectile interaction with the Kevlar target could be observed. The sensitivity of boundary condition effects is not always appreciated in ballistic testing [23]. However, the testing apparatus allowed data collection for two different target boundary conditions: (a) a rectangular target with two fixed edges and two free edges, and (b) a circular target with clamped edges. Additionally, an empirical fit of the data was generated over the range of test conditions which accurately replicated the experimental data. This empirical fit is used in a subsequent chapter to validate the simulations and correlate the results to the experimental data.

2.2 Materials

2.2.1 Kevlar

Kevlar aramid fiber was introduced by the Du Pont Company in 1972 as a miracle fiber and has been used in a wide variety of industrial and civilian applications [115]. The specific Kevlar fabric used in all target constructions was plain-woven Hexcel Schwebel Aramid (paraphenylene terephthalamide) Style 706 fabric (Kevlar KM-2 fiber, 600 denier, 34 yarns per in), commonly marketed for ballistics and protection products [116]. Kevlar Style 706 fabric construction specifications are in Table 2.1 [33, 45]. The term 'neat' when describing Kevlar refers to a plain material that is not mixed with other sub-

stances. Yarn crimp, a measure of the waviness in the yarn, for this particular fabric is 2.3% [44].

2.2.2 Projectile

The projectile was a NATO standard fragment simulation projectile (FSP) MIL-P-46593A, consisting of a chisel-pointed 4340 steel cylinder of 1.1 grams (17 grains) and 0.56 cm diameter (.22 caliber), Fig 2.1 [2].

2.3 Target Preparation and Experimental Procedure

The University of Texas developed the test plan and prepared the Kevlar test panels. Actual ballistic testing was conducted by Southwest Research Institute with assistance provided by the University of Texas. The design of the target fixtures was a collaborative effort by the two organizations: the University of Texas led the design for the two fixed and two free edges target fixture, while Southwest Research Institute led the design of the all clamped edges target fixture. The University of Texas emplaced all targets in fixtures for consistency and supervised the experiments. Actual operation of test equipment (universal gun, cameras, and chronographs) was performed by Grosch [39, 40], SwRI Project No. 18071.02.001 and SwRI Project No. 18054.01.020, in which FSPs impacted various layers of Kevlar fabric at different velocities to achieve penetration. All impacts were at normal obliquity. In the clamped edge tests, Kevlar was cut into 38.1 cm panels and assembled between 22.86 cm steel confinement plates with 10.16 cm circular apertures.

The plates were held together with vise-grip style clamps, Figure 2.2. Testing of the all clamped edges configuration was conducted initially. However, due to the slipping of the target material in the all clamped edges tests, the target fixtures were redesigned by the University of Texas for targets with two fixed and two free edges. In the two fixed and two free edges tests, to minimize fabric slip at the fixed edges of the target, the target frame consisted of a 0.635 cm thick steel plate with a 6.35 cm x 10.16 cm rectangular aperture in the middle. Commercially available two inch wide buckles with locking slide bars (cinch buckles) [75] were bolted to the short edges of the target window, Figure 2.3. A review of the literature showed no other target fixture design similar to this one with cinch buckles. Unlike staples [27] or glue [60] used by other researchers to hold the Kevlar, these buckles were the best method found to secure the Kevlar targets. Kevlar was cut into strips 5.08 cm x 25.4 cm from the same sheet obtained from the manufacturer and assembled into the target frame in accordance with the specified number of layers. The Kevlar was tightened to minimize any slack, but not stretched, to the point where the buckle slide bars were engaged in the locked position to immobilize the target material. The long edges of the Kevlar strips were unconstrained, Figure 2.4.

The ballistic tests were performed at Southwest Research Institute (SwRI) using a Universal Receiver chambered for a .22 Hornet centerfire cartridge. The barrel was eight inches in length with 1:16 rifling. The rifling grooves imparted a rotational velocity on the FSP for flight stability, equivalent to one revolution for every 16 inches in barrel length. All tests were

performed at room temperature. The barrel was aimed on the target center, and a laser was used to confirm target obliquity and align the gun with the desired impact location. The impact velocity (V_i) of each projectile was measured using two sets of chronographs positioned between the gun muzzle and the target. The impact velocities were adjusted to provide penetration of the target and a range of residual velocities (V_r). The performance of the Kevlar could be assessed on a continuum by evaluating the residual velocities and differentiating between the number of layers.

Two Vision Research Phantom V7 monochrome cameras recorded the impact event at 40,000 frames per second with a resolution of 192 x 192 pixels per image. One camera provided a side view of the target and measured residual velocity of the FSP after it penetrated the target. A fixed ruler mounted to the target frame showed the distance and time the projectile traveled when the film was reviewed. A second camera provided an oblique view of the rear of the target and recorded target deflection and the projectile and target interaction. A third chronograph positioned between the second camera and bullet trap also measured the residual velocity. Figure 2.5 shows the experimental setup for the FSP impact tests.

2.4 Results of Impact Experiments

A series of tests for one, two, and four layer Kevlar targets were conducted with various impact velocities to obtain corresponding residual velocities. In general, with increasing layers of Kevlar, a higher impact velocity

was necessary to achieve penetration. In each case, the impact velocities were obtained directly from two chronographs, and the residual velocities were measured from a side view camera and directly with a single chronograph. Tables 2.2 (two fixed and two free edges) and 2.3 (all clamped edges) summarize the data from the ballistic experiments. Tests that resulted in edge of target impacts (Table 2.2 Test # 6) or no velocity measurements (Table 2.2 Test # 1) due to equipment malfunction are not included in the tables. In several cases where the impact velocities were nearly the same value, the residual velocities were consistently close as well. This is indicative of the uniform target preparation and materials and the level of reliability and repeatability achieved in these experiments.

The performance of the fabric undergoing impact is reflected in observations of post-impact damage. Post-impact observations of the Kevlar target revealed lateral movement of impacted yarns relative to the fabric structure but in other cases, especially for the lower velocities, the damage of impacted yarns included more yarn pull-out. This observation shows that the fabric failure is a result of the projectile velocity, and matching the Kevlar structure and geometry to the threat projectile is critical to achieving maximum impact protection [53]. The Kevlar fabric had drawn toward the vicinity of the impact, maintaining contact with the projectile until failure. In the experiments with two fixed and two free edges, yarns parallel to the free edges were freed by the ballistic impact, exposing the ends of the shorter cross-yarns, Figure 2.6. Review of the video presented the well documented cone shaped deformation

of the Kevlar and showed the Kevlar yarns pulled and strained until failure. Figure 2.7 shows a FSP impact at 297 m/s on one layer of Kevlar with two fixed and two free edges. Yarn pull-out is most prominent in the direction where the yarn length is short and the edges are unrestricted.

2.5 Analysis and Scaling

These experiments do show the effects of Kevlar target geometry in response to impact loading. The sensitivity of the residual velocity increased as the impact velocity decreased. When the impact velocity was high enough to cause the Kevlar to fail quickly, the fabric deformation was localized at the impact area. At low velocity, Kevlar failure was delayed. The delay of Kevlar failure and time increase of impact loading allowed the fabric to deform more and absorb more energy. At low velocities, target deformation reached the target boundaries before failure. These experiments also indicate that target boundary conditions affected ballistic performance. In general, the Kevlar more effectively reduced the projectile velocity and absorbed more energy with two fixed and two free edges compared to the all clamped edges experiments.

2.5.1 Two Fixed / Two Free Edges Experiments

FSP impact results on one, two and four layers are shown in Figures 2.8 - 2.10, and a combined plot with all layers is in Figure 2.11. A nonlinear relationship is present between the impact and residual velocities for all cases [55]. The data forms a curve in each case that intersects the horizontal axis,

implying a limit where there is no residual velocity for any impact velocity below this value. This threshold is commonly known as the ballistic limit or V_{50} , where a projectile has a 50% probability of penetrating a target at that given impact velocity [73]. Physically, the projectile's kinetic energy is being transferred to the target material, so a higher V_{50} value signifies a target with enhanced ballistic performance that can absorb more energy [11, 26].

To maintain conservation of energy, the projectile's kinetic energy must be transferred into several factors during the impact event. Several energy absorbing components are present, and collectively they reduce the projectile velocity and hence energy. A certain amount of kinetic energy is converted into fiber elongation and eventually failure, kinetic energy in the fabric, heat, and noise. If the velocity of the projectile is great enough to achieve penetration, the remaining energy consists of the residual velocity of the projectile. The experiments indicate that at high impact velocities, the residual velocity approaches the impact velocity. Most of the material failure at high velocities is localized since the material has little time to elongate and deform [95]. Hence, the energy absorbed would be very small and the projectile residual velocity can be expected to approach the impact velocity.

This residual velocity relationship for the particular FSP impact experiments can be expressed for each number of layers as

$$V_r = V_i \left(1 - e^{-\beta \left(\frac{V_i}{\alpha} - 1 \right)} - \frac{V_0}{V_i} \right) \quad (2.1)$$

where V_i is the impact velocity and α , β , and V_0 are parameters relating the shape of the residual velocity curve. These values for α , β and V_0 are fit to the number of layers, and the values of these parameters are specific to the target and projectile materials and geometry.

Use of Equation 2.1 requires α and β which were calculated with the following equations. As parameters describing the shape of the residual velocity curve, their values represent the best fit of the experimental data. As described in the Appendix, α can be calculated using

$$\alpha = \frac{\lambda V_{50} - V_i}{\lambda - 1} \quad (2.2)$$

where

$$\lambda = \frac{\ln\left(1 - \frac{V_r}{V_i} - \frac{V_0}{V_i}\right)}{\ln\left(1 - \frac{V_0}{V_{50}}\right)} \quad (2.3)$$

Values for V_0 were selected and proportionally scaled based on the number of layers. Similarly, the V_{50} values were estimated from the experimental data. With V_0 and V_{50} established, α was calculated for each data point and averaged for the number of layers for further calculations. Once α was computed, β could be calculated with the following equation

$$\beta = -\frac{\ln\left(1 - \frac{V_0}{V_{50}}\right)}{\left(\frac{V_{50}}{\alpha} - 1\right)} \quad (2.4)$$

For the two fixed and two free edges experiments with .22 cal FSP projectiles and one, two, and four layers of Kevlar, the V_{50} values increased from 120 m/s , to 190 m/s , and to 315 m/s , respectively. The other parameters used in Equation 2.1 can be found in Table 2.4.

2.5.2 Clamped Edges Experiments

Figure 2.12 shows the post-impact result of a clamped edge experiment revealing the amount of deformation and damage. With clamped boundary conditions, the target cannot deform as much as a target with free edges. Figure 2.13 shows a FSP impact at 340 m/s on two layers of Kevlar with clamped edges.

Figures 2.14 - 2.16 show a similar trend in the clamped edge experiments, where increased layers require higher velocities to achieve penetration and residual velocities approach impact velocities at high velocity. A combined plot with all layers is in Figure 2.17. The two fixed and two free edges boundary conditions gave better ballistic performance (lower residual velocities) than the all clamped edges boundary conditions.

This residual velocity relationship for the particular FSP impact experiments can be expressed for each case with Equation 2.1. For the clamped edges experiments, calculating the parameters for the correlation differed slightly as follows. Values for V_0 were selected and proportionally scaled based on the number of layers. Due to the scatter of the clamped FSP data, values for β were chosen to give the best fit of the experimental data. Rearranging Equa-

tion 2.1 in the following form allows α to be calculated for each data point and averaged for the corresponding number of layers.

$$\alpha = \frac{V_i}{1 - \frac{1}{\beta} \ln \left(1 - \frac{V_r}{V_i} - \frac{V_0}{V_i} \right)} \quad (2.5)$$

Since $V_r = 0$ at $V_i = V_{50}$, substitution into Equation 2.1 gives the following expression for V_{50}

$$V_{50} = \alpha - \frac{\alpha}{\beta} \ln \left(1 - \frac{V_0}{V_{50}} \right) \quad (2.6)$$

The V_{50} values were calculated from the previous equation at 120 *m/s*, 163 *m/s*, and 275 *m/s*, respectively for FSP impacts on one, two, and four layers of Kevlar with all clamped edges.

A summary of the fitted parameters by layer and boundary conditions is in Table 2.4. These correlations will be used in a subsequent chapter to validate FSP impact simulations.

2.5.3 Boundary Conditions

Residual velocities of the two fixed and two free edges and all clamped edges by layers are presented in Figures 2.18 - 2.20. In general, the Kevlar with all clamped edges resulted in higher V_r values, indicative of poorer ballistic performance. Overall, the results are consistent with other research that have shown targets with free edges have a higher ballistic limit and absorb

more impact energy than targets with all clamped edges [23, 31, 117]. Boundary condition effects are most significant at lower velocities where the fabric deformation is the greatest before failure. At high velocities, fabric deformation and failure is localized near the point of impact, and fabric deformation has not reached the target boundaries. The processes of yarn axial tension and yarn interaction both contribute to the spatial and temporal spreading of the load and to energy extraction from the projectile [89]. When all edges are clamped, the yarns have more limited ability to move. On impact, the yarns deform and decelerate the projectile until they reach their failure strain. However, free edges allow greater movement of the Kevlar target so that the kinetic energy transferred to the target is much higher than for targets with constrained boundaries. This process further decelerates the projectile as the fabric is in contact with the projectile over a greater distance and time. When the fabric can deform and shroud the projectile, the fabric layers are carried along the path of the projectile, adding mass and drag.

2.6 Summary

The present work has described a series of experiments consisting of a standard shaped projectile impacting specified layers of plain woven Kevlar Style 706 fabric to analyze impact phenomena and for validation of future simulations. Targets included rectangular panels with two fixed and two free edges as well as circular panels with all clamped edges. The experiments measured the impact and residual velocities of the projectile, and cameras

recorded the event. The experimental results provide a relationship between the impact velocity and the number of layers of target material that can be used to estimate residual velocities for FSP impacts from the ballistic limit to beyond the range of experiments. Boundary condition effects are more evident at lower velocities when the Kevlar deformation is delayed and not localized, and the constrained target system has more limited mobility to deform and absorb the projectile's energy.

A new target fixture not seen before in published reports was used to secure the target material. A database of FSP impacts on different layers of Kevlar and different boundary conditions was obtained. Finally, a correlation of the experimental data was generated for use in future validation of simulations.

Several suggestions specific to FSP impact testing and modeling on Kevlar fabric are given to include: (1) additional experiments should be conducted with different target designs and boundary conditions to investigate further the effects of target geometry and the boundary conditions, (2) additional experiments should be performed over a wider range of impact velocities and number of layers to extend the range for future validation, and (3) additional experiments are needed with oblique impacts and different shaped projectiles to validate future computational analysis methods and simulations.

Table 2.1: Style 706 Kevlar fabric construction specifications

Property	Value	Reference
Areal Density (g/cm^2)	0.0180	[45]
Thickness (cm)	0.023	[45]
Warp and fill count ($yarns/in$)	34	[45]
Fiber Density (g/cm^3)	1.45	[33], p.3

Table 2.2: Experimental results: FSP impacts on two fixed and two free edges of neat Kevlar

Test #	Number of Layers	V_i (m/s)	V_r (m/s)
2	1	185	127
3	1	175	124
4	1	297	254
5	1	299	249
7	1	364	322
8	1	294	250
23	1	226	142
24	1	213	145
9	2	282	184
10	2	294	201
11	2	304	219
12	2	428	374
13	2	172	39
14	2	253	76
15	2	376	313
16	2	309	221
17	4	339	113
18	4	446	347
19	4	538	474
20	4	382	236
21	4	465	387
22	4	386	255

Table 2.3: Experimental results: FSP impacts on clamped edges of neat Kevlar

Test #	Number of Layers	V_i (m/s)	V_r (m/s)
1	1	164	0
2	1	210	128
3	1	215	150
4	1	348	312
17	1	115	0
18	1	195	130
19	1	257	205
20	1	272	233
5	2	179	0
6	2	141	0
7	2	340	297
8	2	315	256
21	2	372	326
22	2	323	264
23	2	262	186
24	2	296	235
9	4	264	0
10	4	356	246
11	4	328	52
12	4	348	230
13	4	441	379
14	4	397	312
15	4	404	292
16	4	324	181

Table 2.4: Residual velocity equation parameters for the FSP experimental data

Number of Layers	Boundary Condition	V_0 (m/s)	α (m/s)	β
1	2 fix/2 free	36	99.8	1.77
2	2 fix/2 free	44	172	2.61
4	2 fix/2 free	60	304	5.97
1	clamped	30	104	1.75
2	clamped	36	149	2.50
4	clamped	40	264	4.00

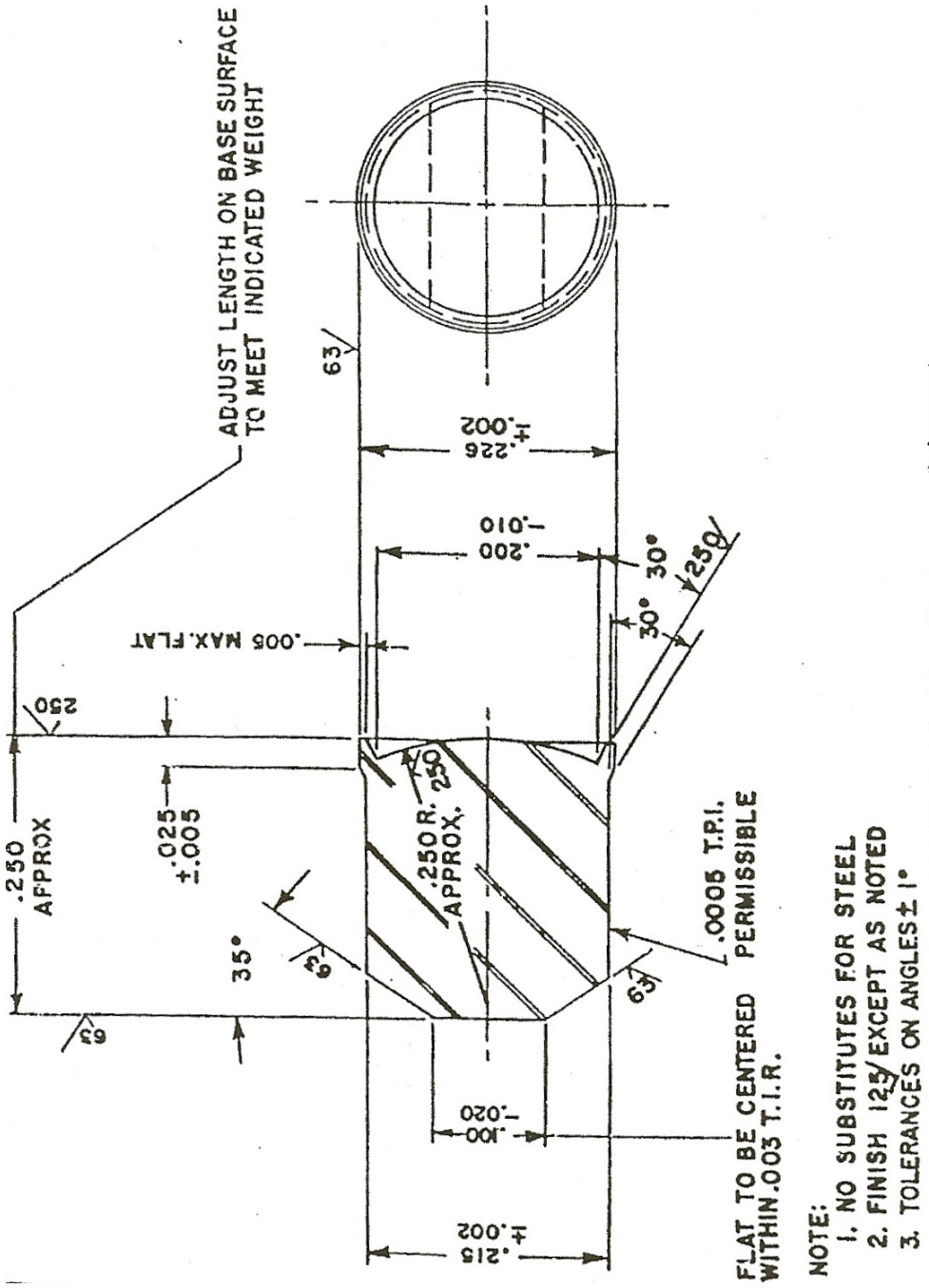


Figure 2.1: Fragment simulating projectile [2]

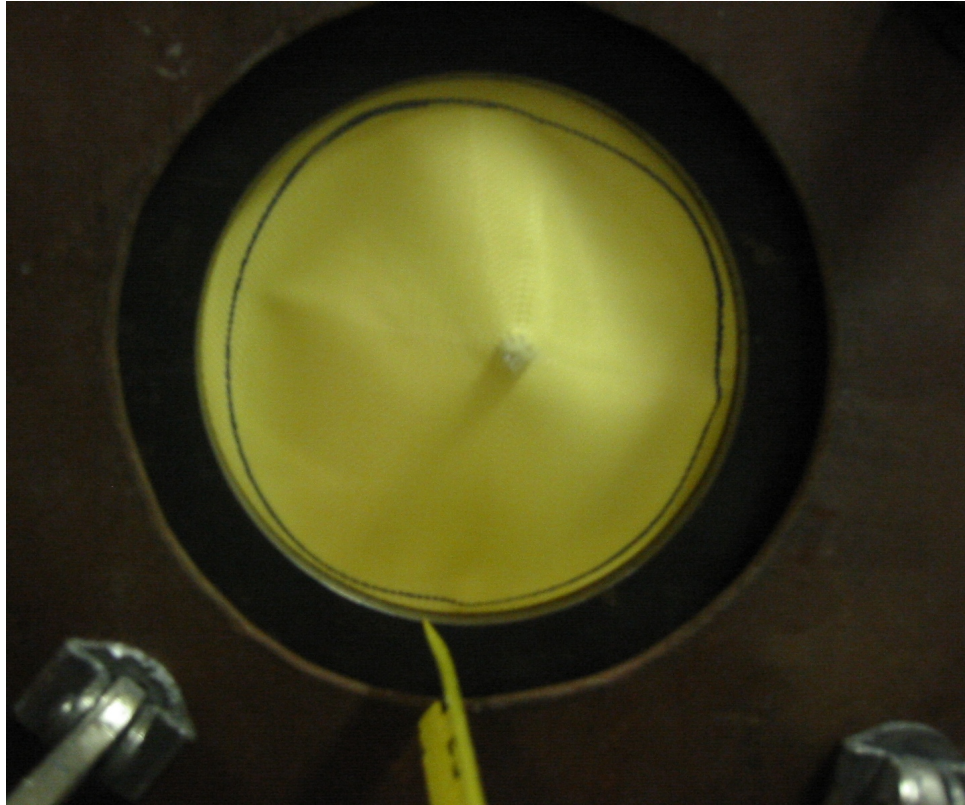


Figure 2.2: Target frame for the Kevlar with clamped edges



Figure 2.3: Cinch buckles for mounting the Kevlar in the two fixed and two free edges experiments

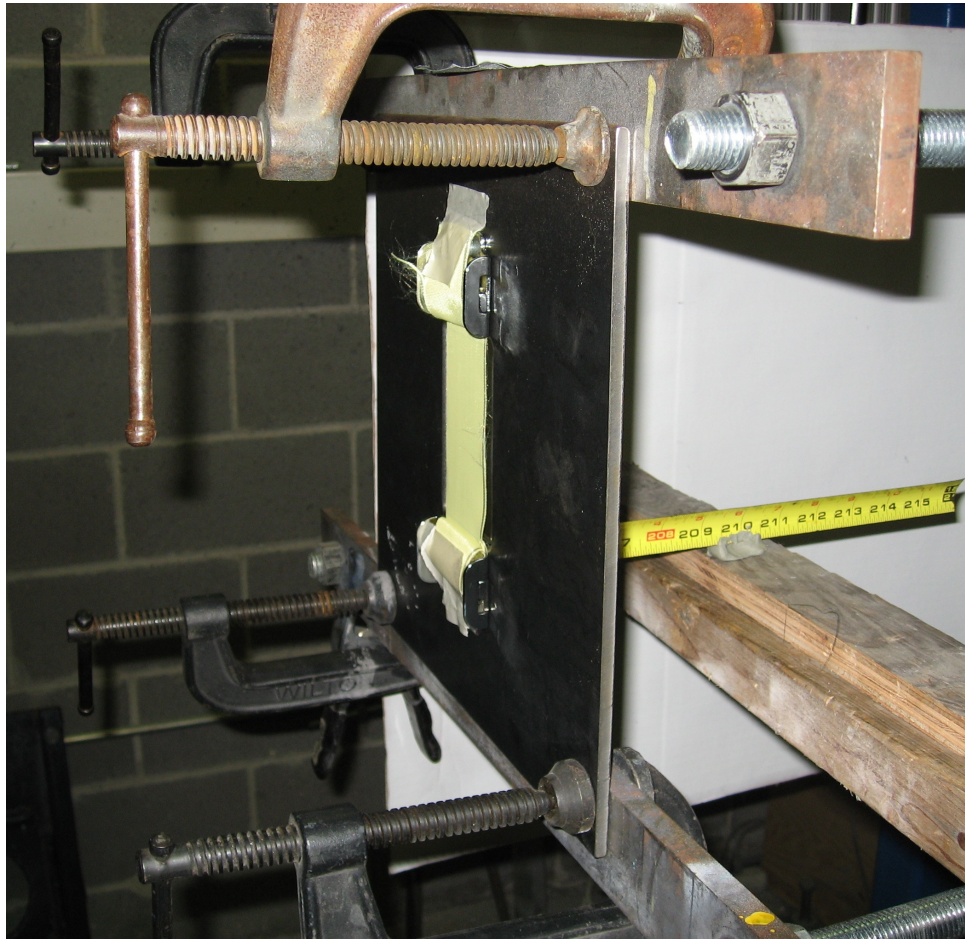


Figure 2.4: Target frame for the Kevlar with two fixed and two free edges

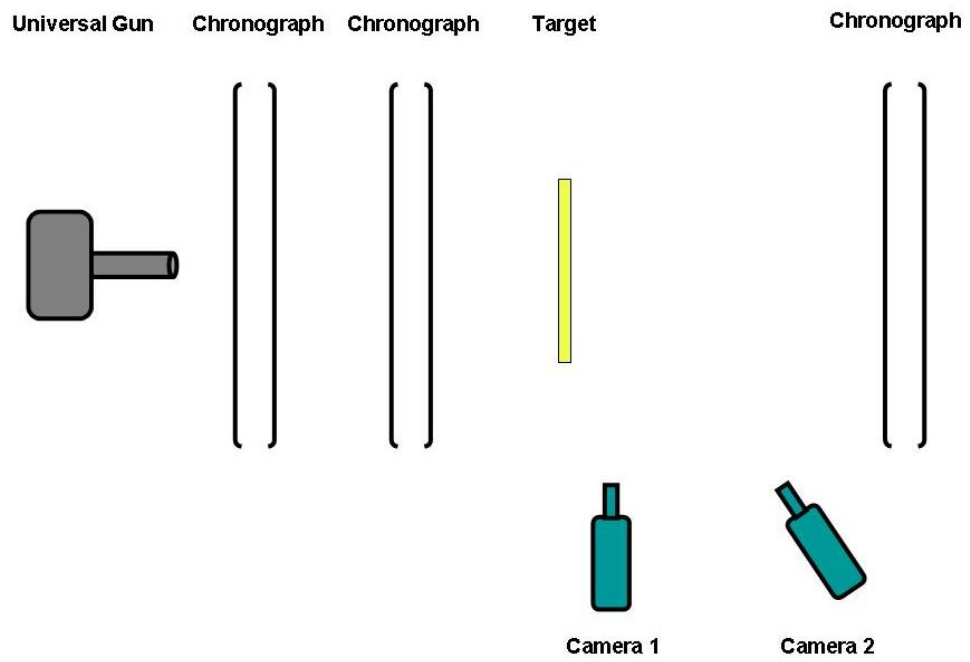


Figure 2.5: Experimental setup for FSP impact tests

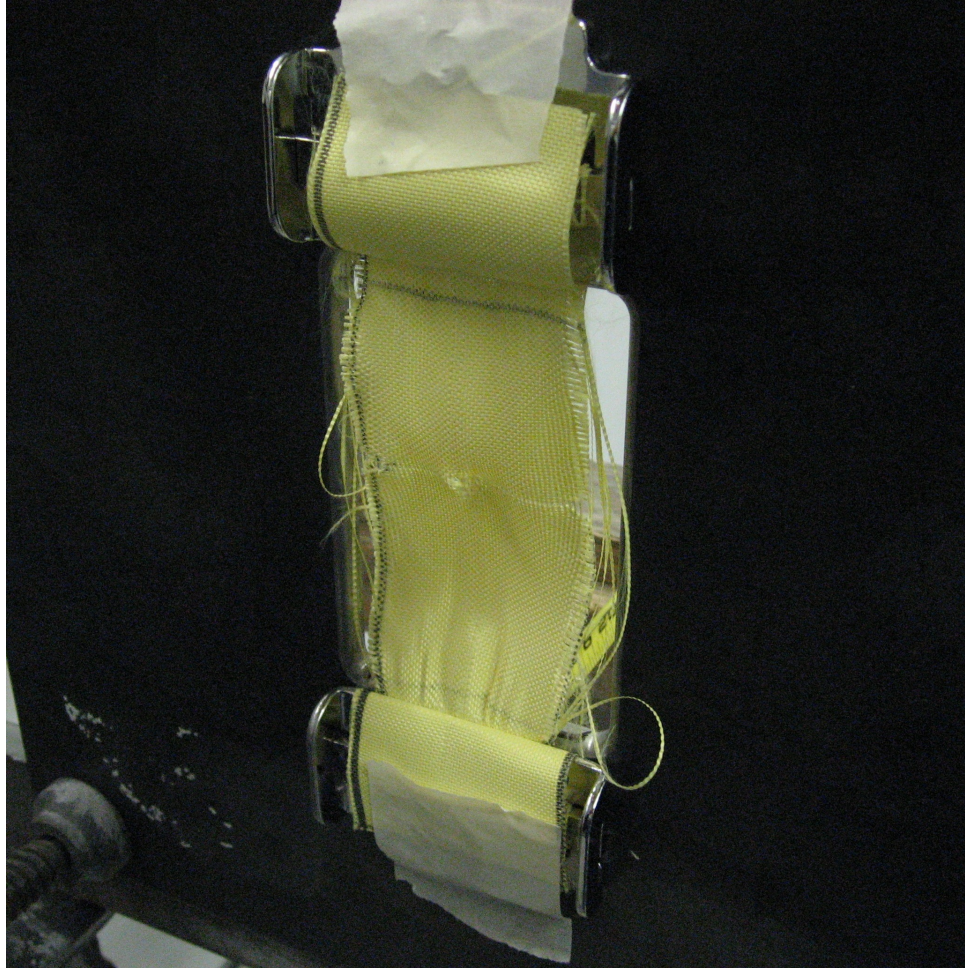


Figure 2.6: Post-impact damage for one layer of Kevlar with two fixed and two free edges

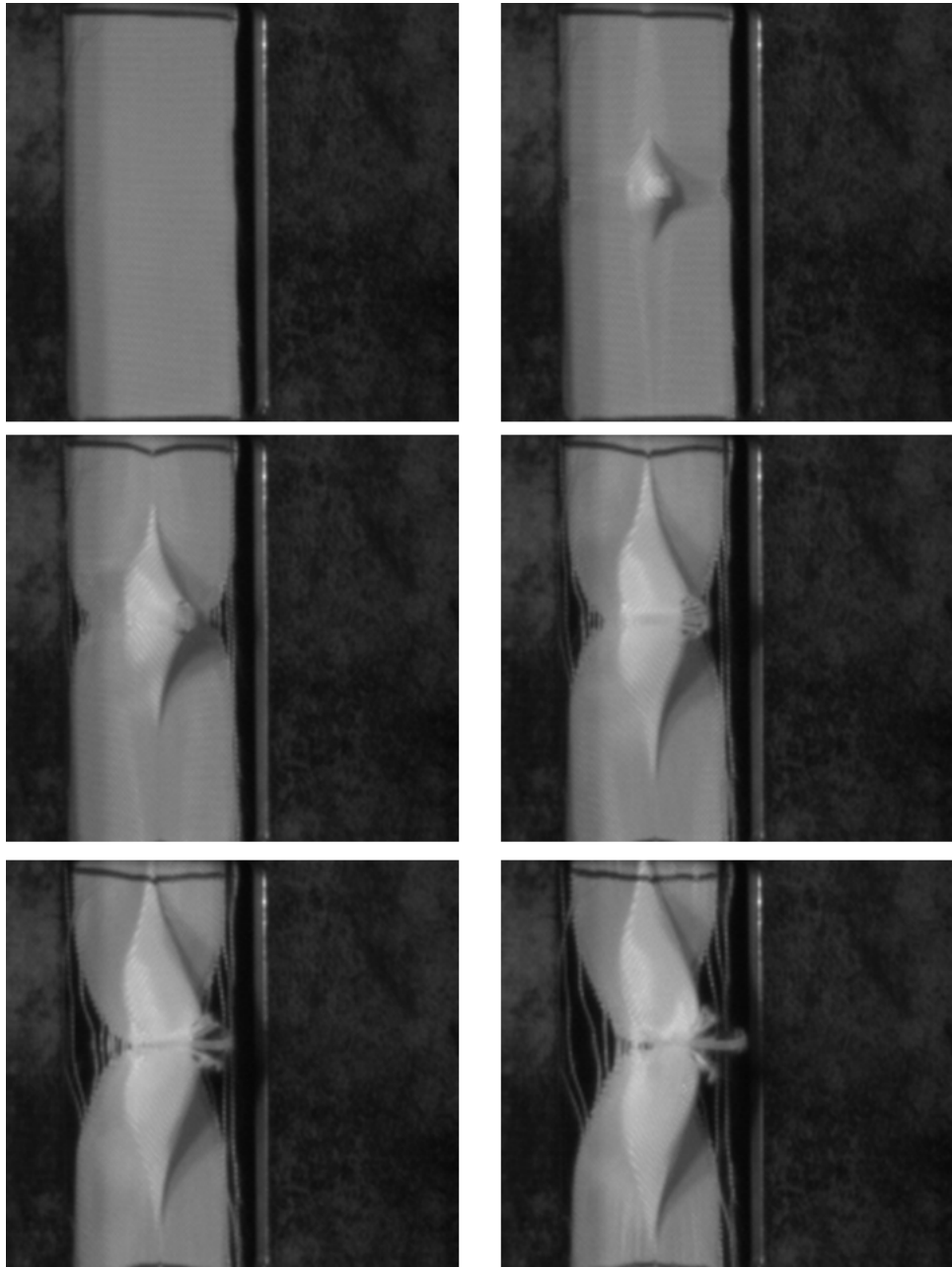


Figure 2.7: Images for a FSP impact at 297 m/s on one layer of Kevlar with two fixed and two free edges

One layer FSP data (2 fixed, 2 free edges)

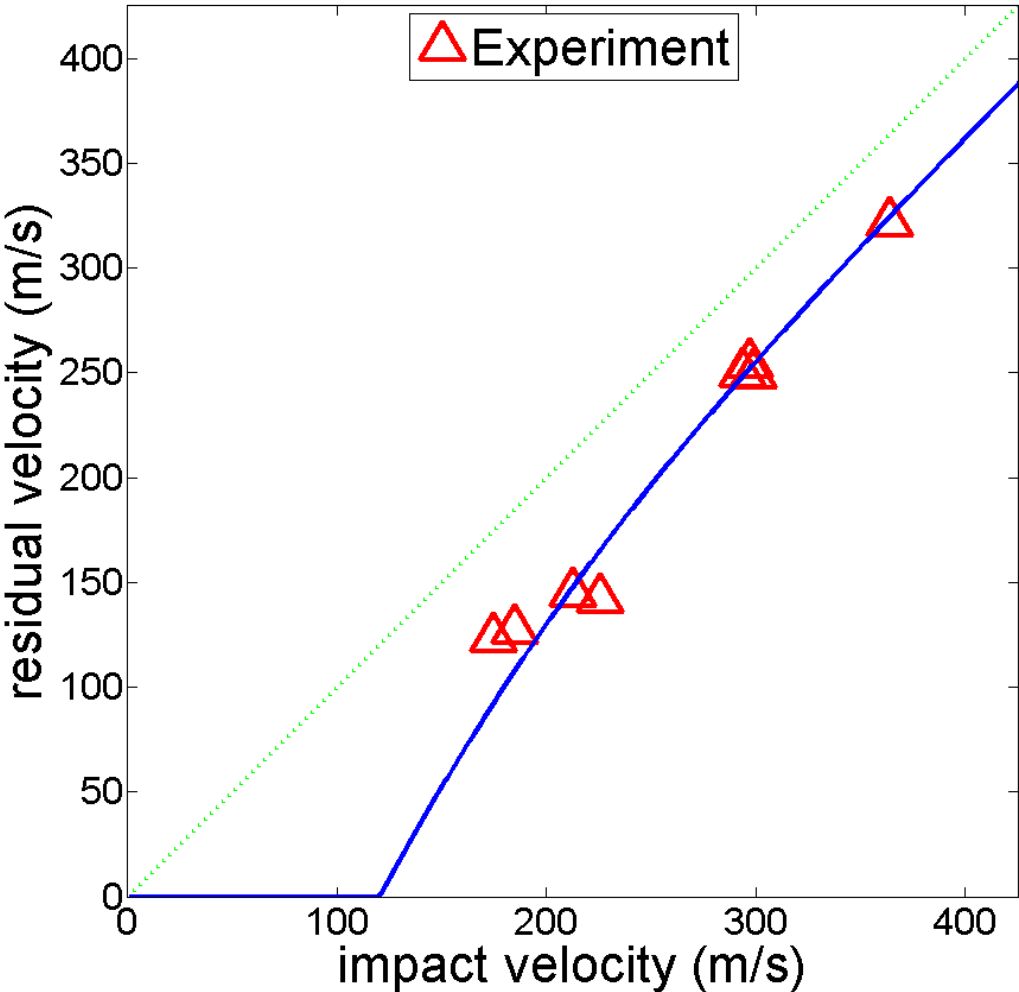


Figure 2.8: Experimental results: FSP impacts on one layer of Kevlar with two fixed and two free edges

Two layer FSP data (2 fixed, 2 free edges)

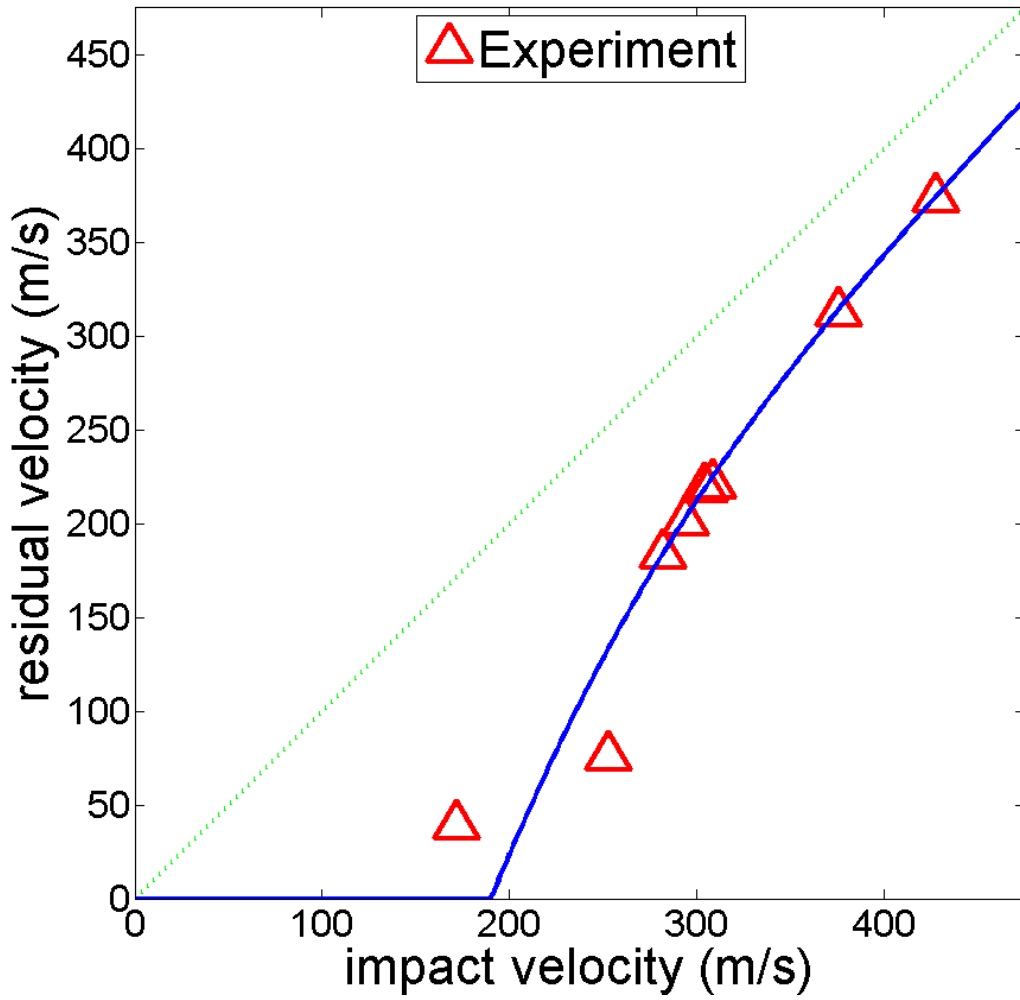


Figure 2.9: Experimental results: FSP impacts on two layers of Kevlar with two fixed and two free edges

Four layer FSP data (2 fixed, 2 free edges)

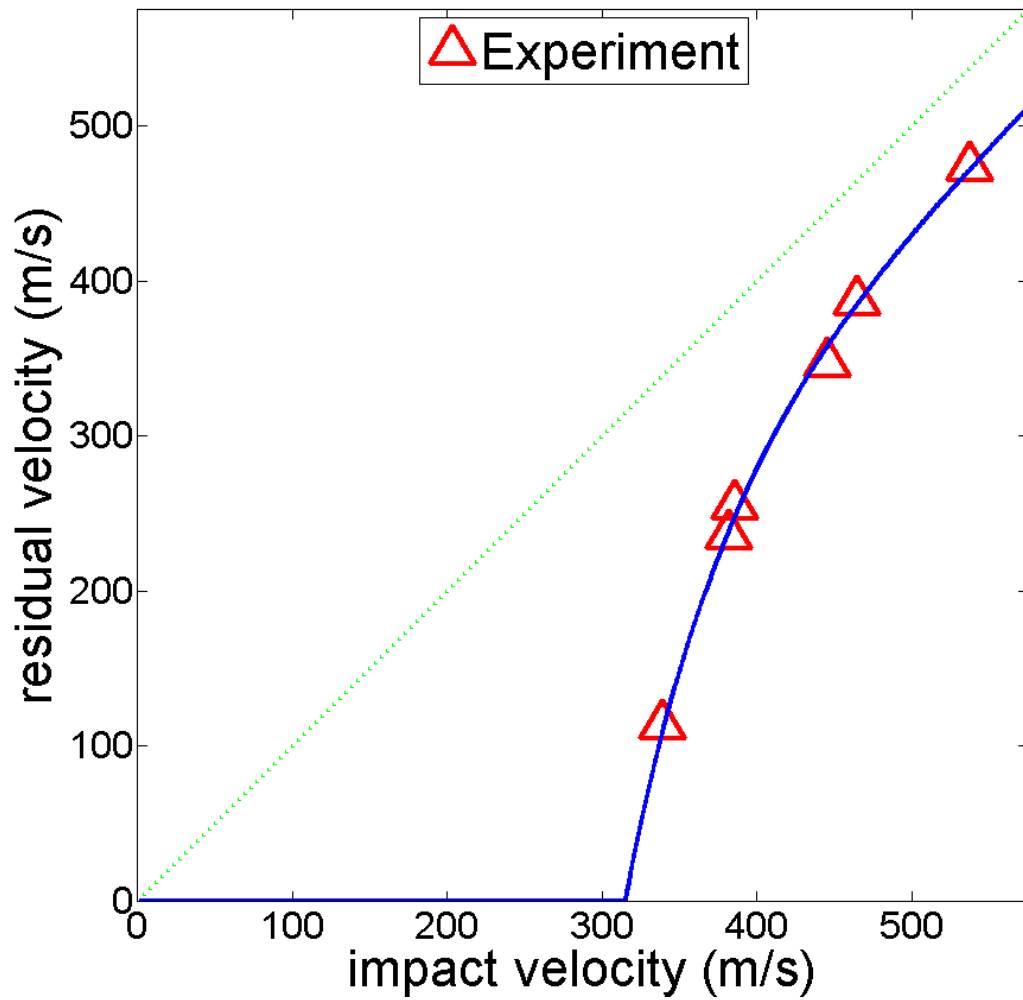


Figure 2.10: Experimental results: FSP impacts on four layers of Kevlar with two fixed and two free edges

FSP data (2 fixed, 2 free edges)

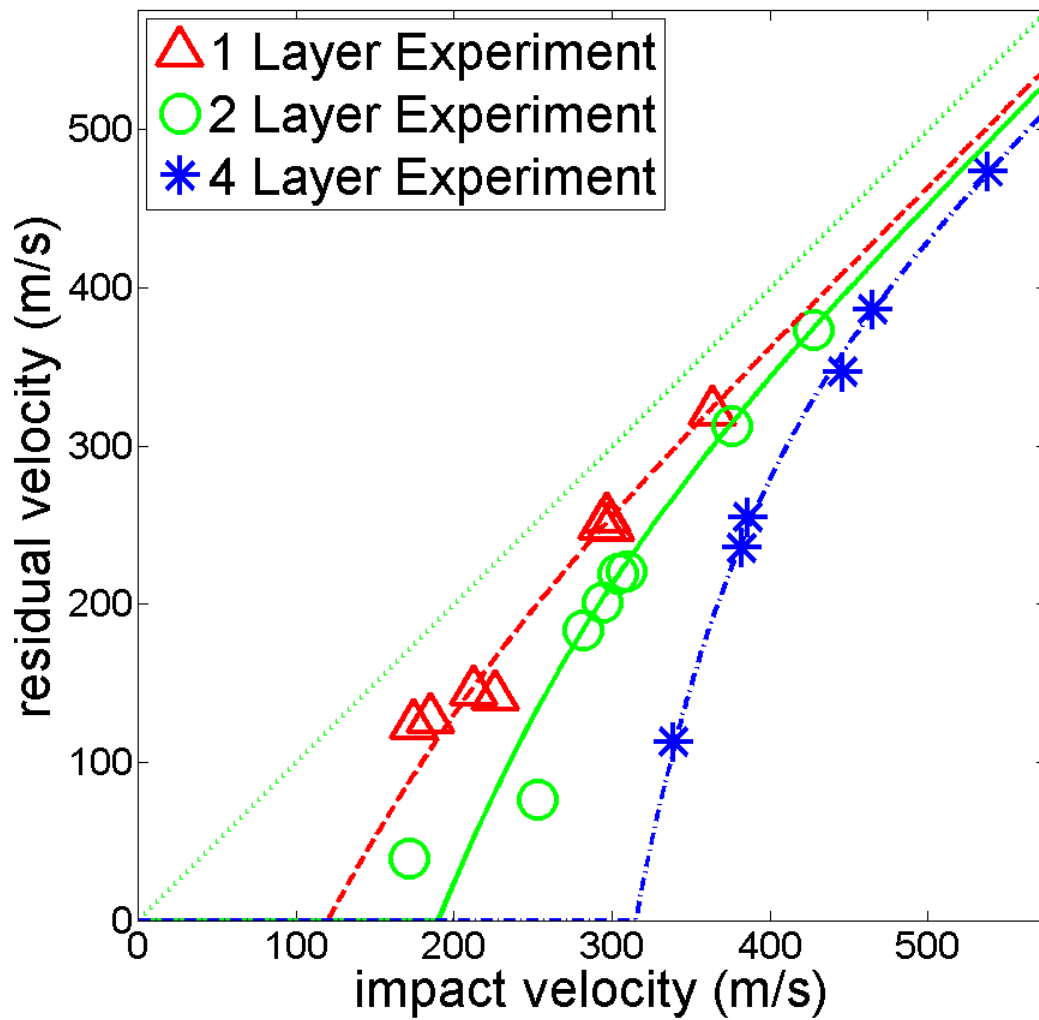


Figure 2.11: Experimental results: FSP impacts on Kevlar with two fixed and two free edges



Figure 2.12: Post-impact damage for one layer of Kevlar with clamped edges

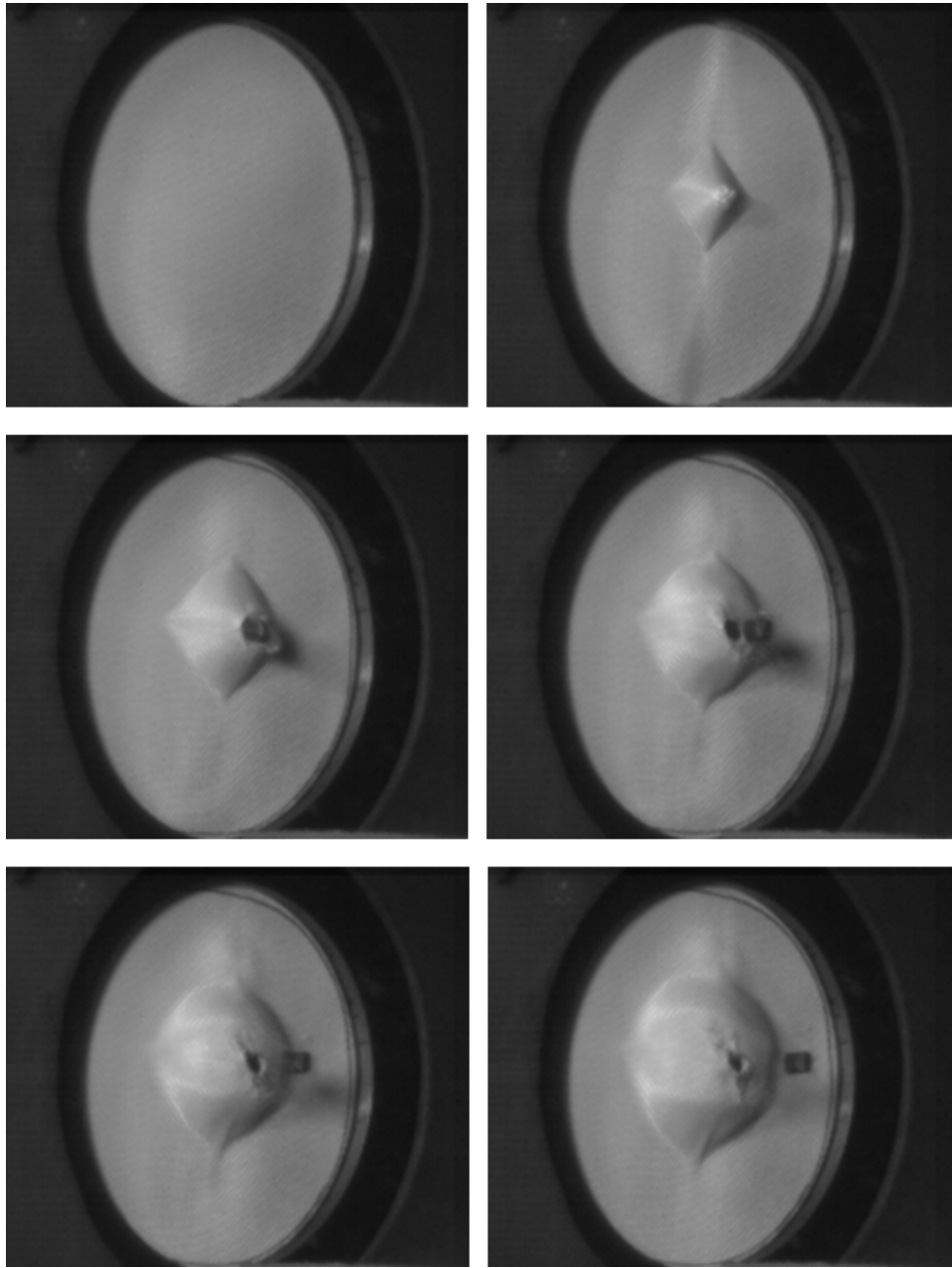


Figure 2.13: Images for a FSP impact at 340 m/s on two layers of Kevlar with clamped edges

One layer FSP data (clamped)

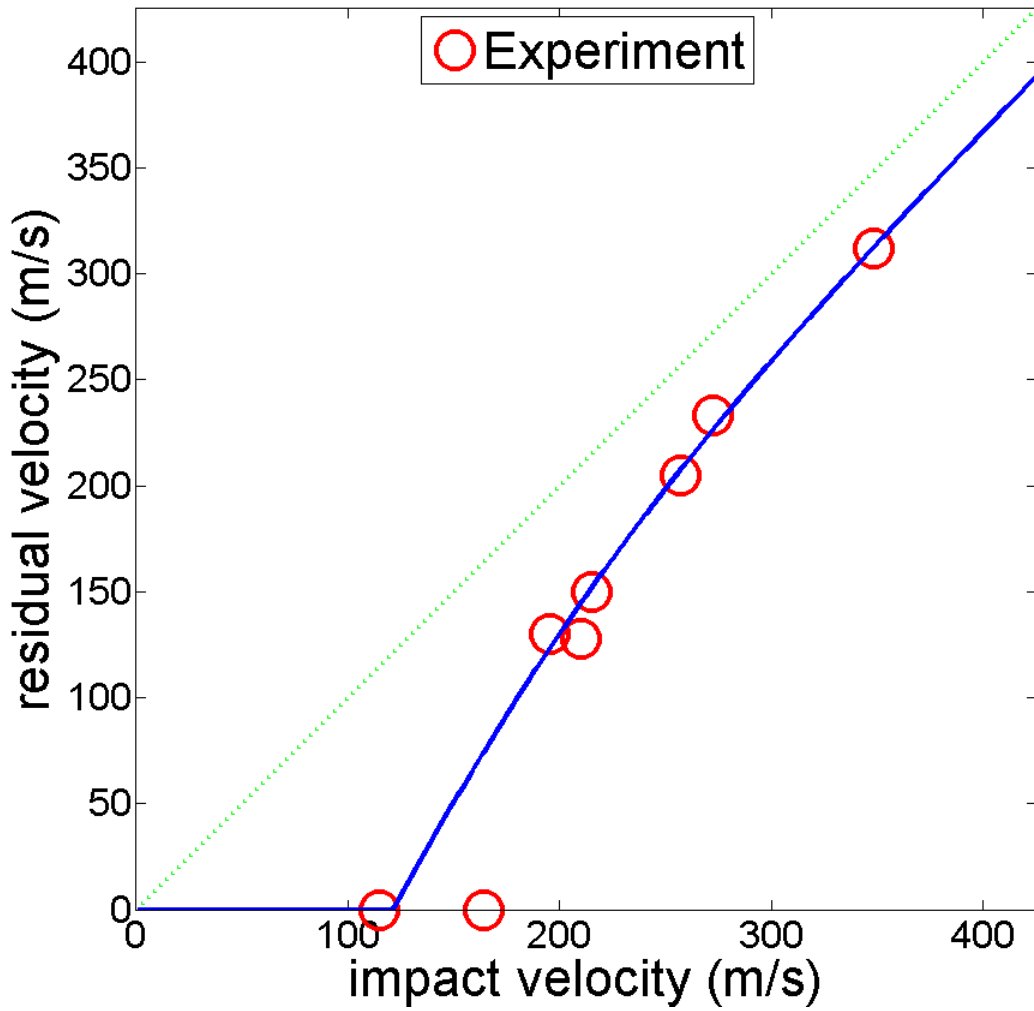


Figure 2.14: Experimental results: FSP impacts on one layer of Kevlar with clamped edges

Two layer FSP data (clamped)

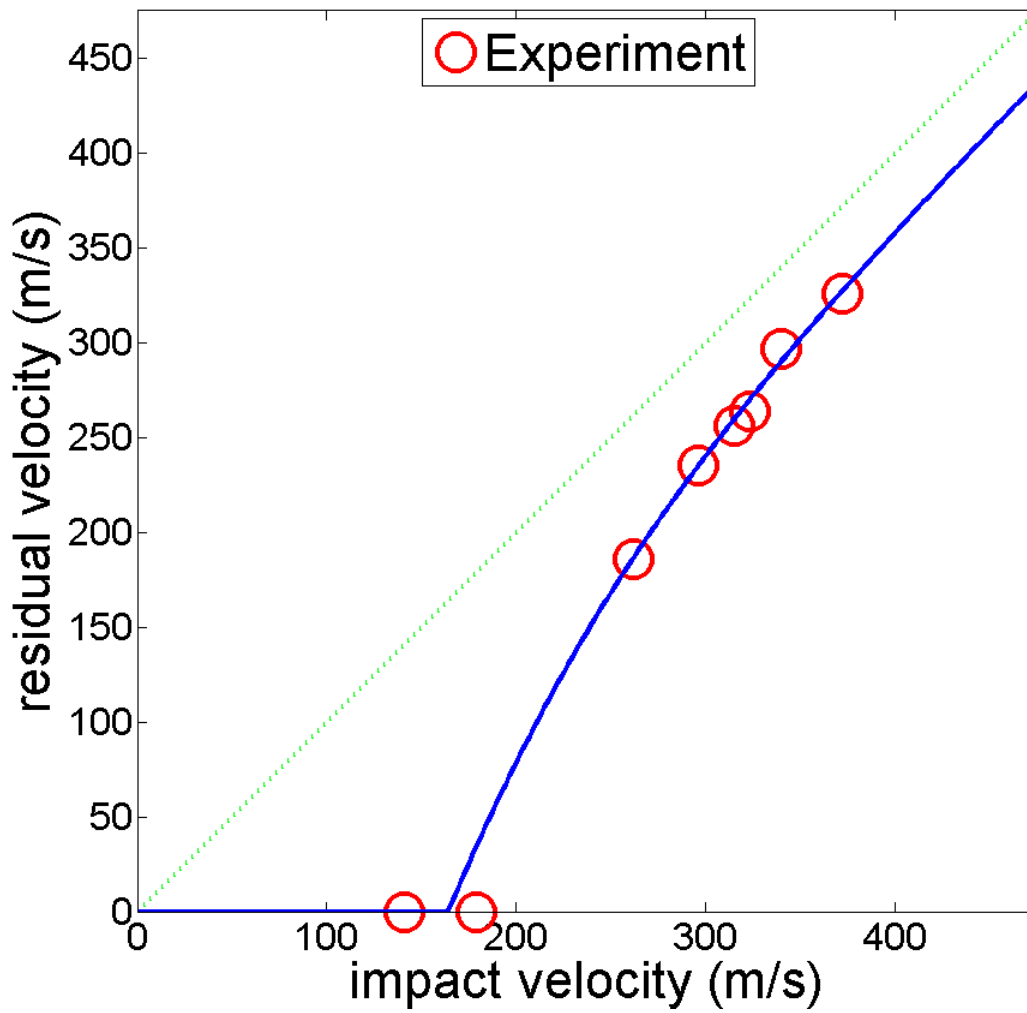


Figure 2.15: Experimental results: FSP impacts on two layers of Kevlar with clamped edges

Four layer FSP data (clamped)

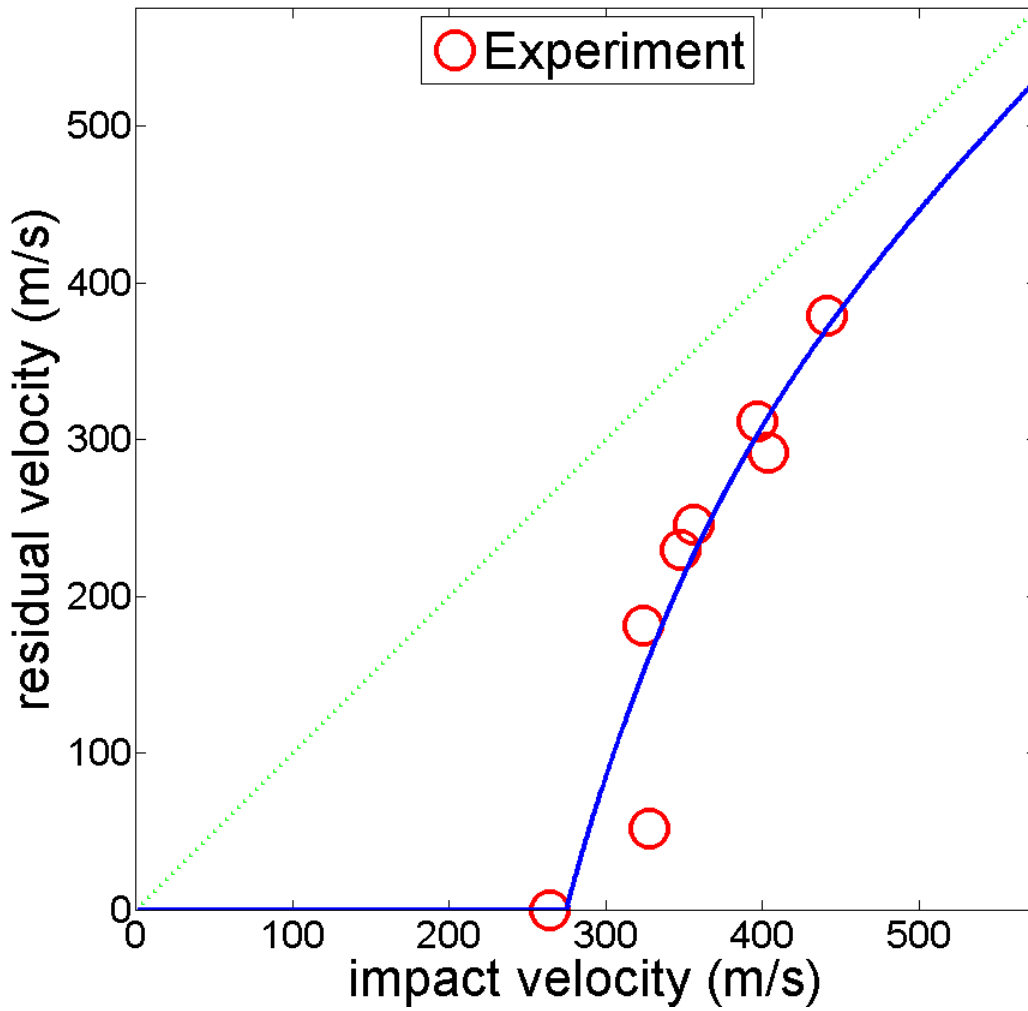
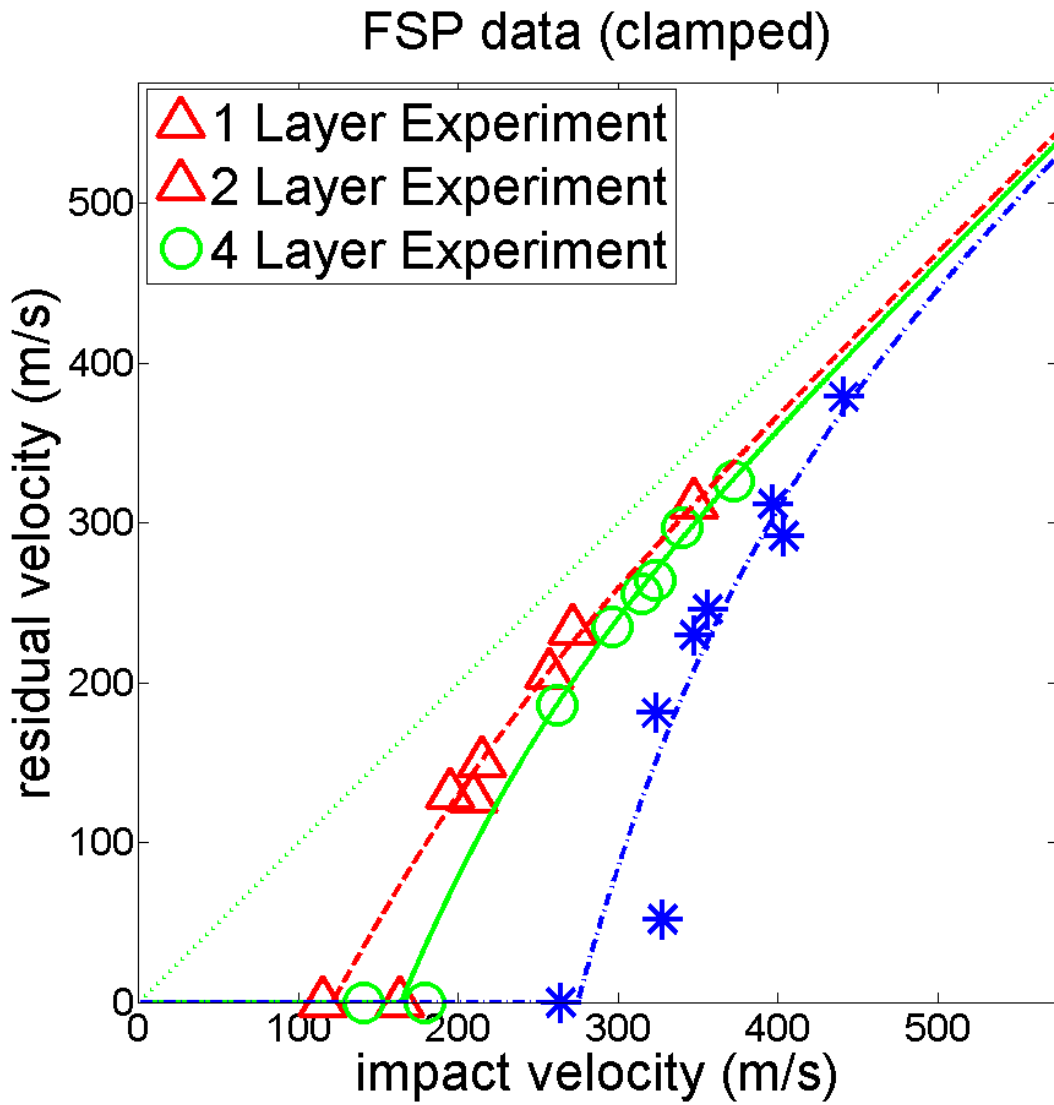


Figure 2.16: Experimental results: FSP impacts on four layers of Kevlar with clamped edges



One layer FSP data (clamped and fixed/free edges)

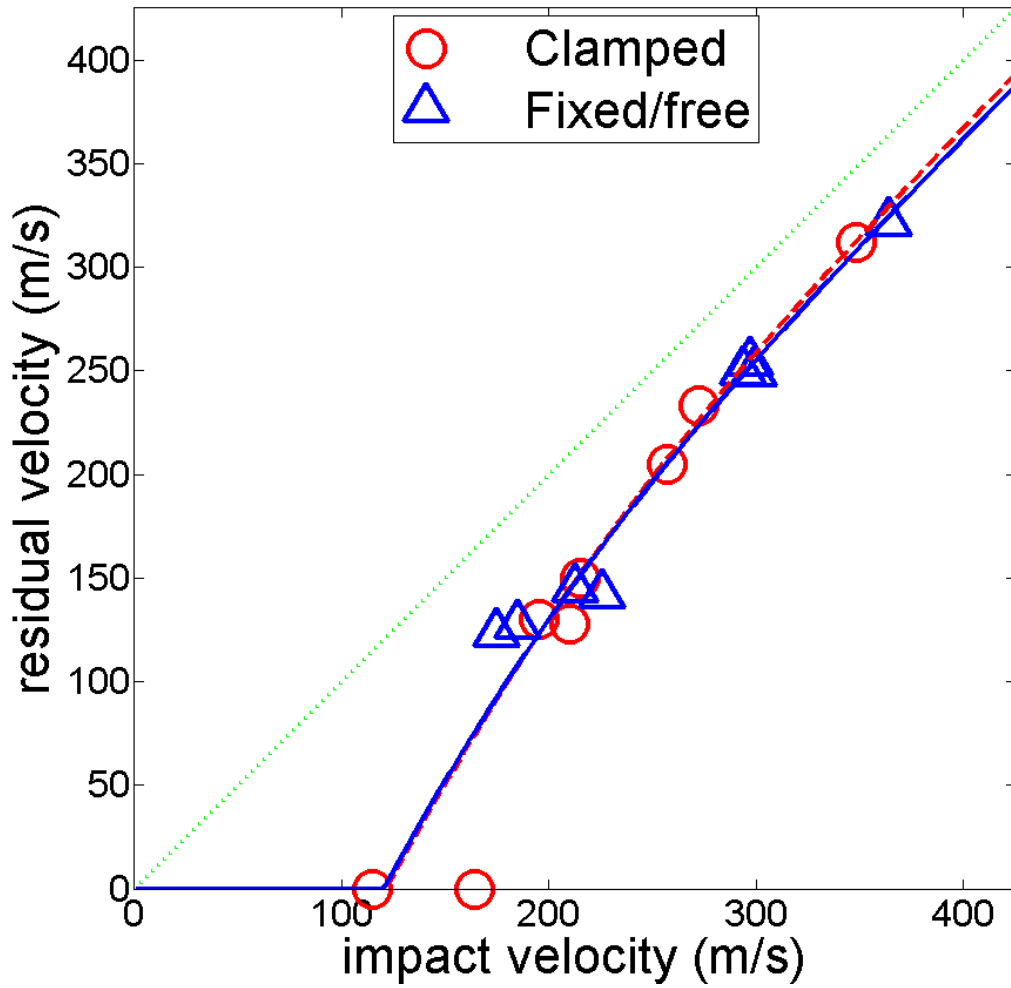


Figure 2.18: Comparison of FSP impacts on one layer of Kevlar with two fixed/two free edges and clamped edges

Two layer FSP data (clamped and fixed/free edges)

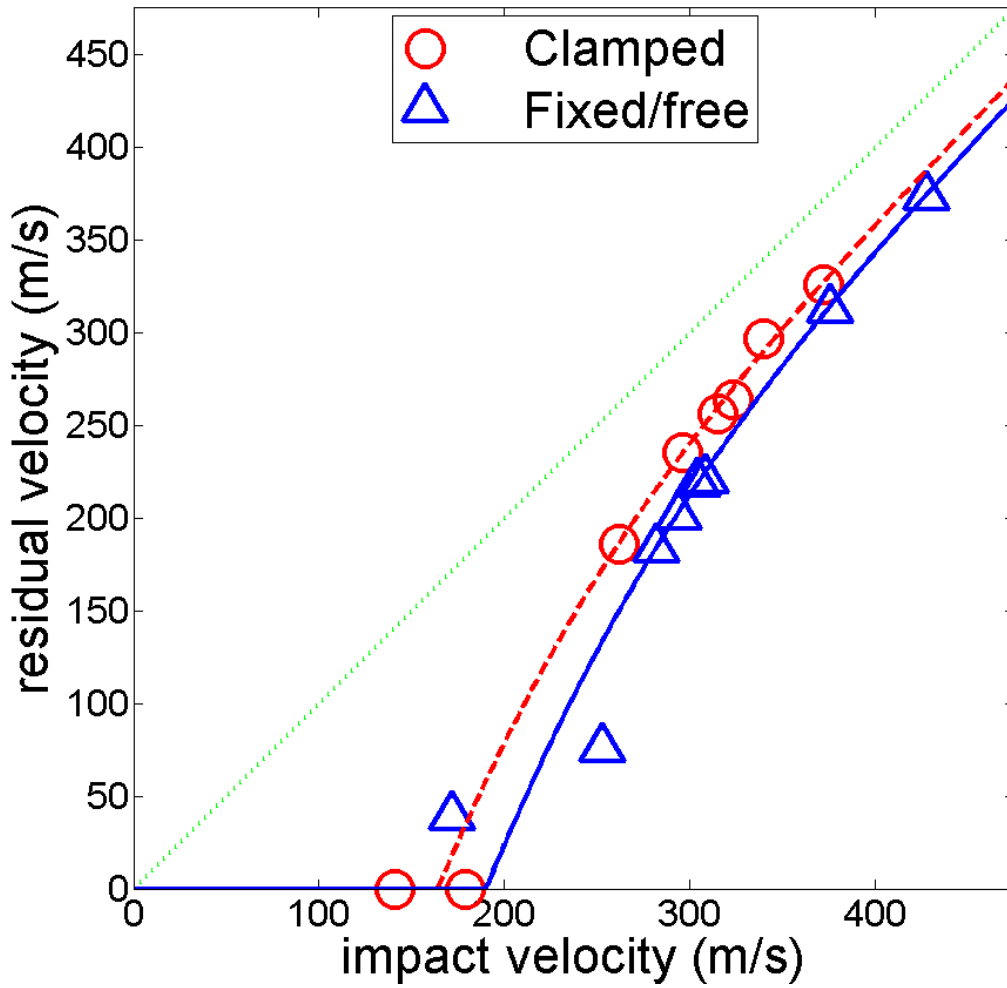


Figure 2.19: Comparison of FSP impacts on two layers of Kevlar with two fixed/two free edges and clamped edges

Four layer FSP data (clamped and fixed/free edges)

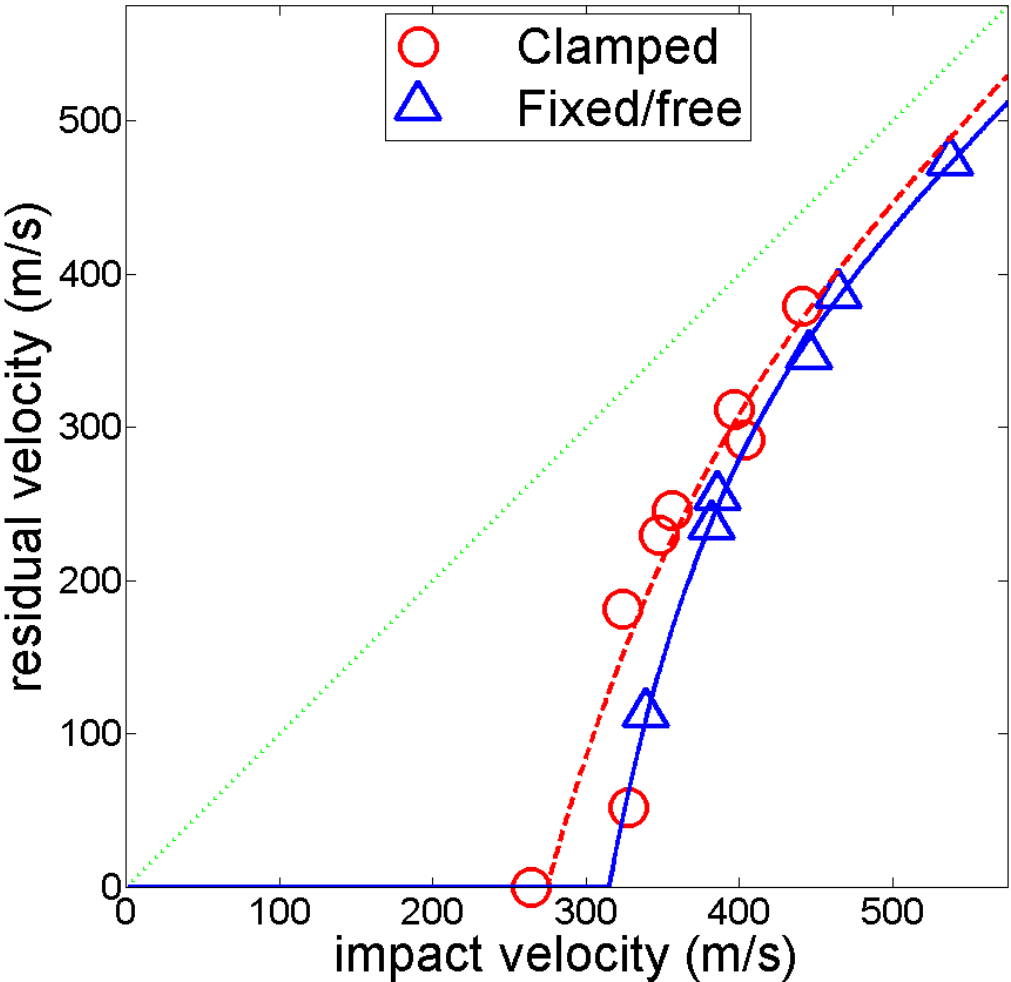


Figure 2.20: Comparison of FSP impacts on four layers of Kevlar with two fixed/two free edges and clamped edges

Chapter 3

Comparison and Analysis of Neat and Shear Thickening Fluid Kevlar Impacts

3.1 Introduction

The aviation industry has seen in-flight engine failure fragments damage critical aircraft components, resulting in aircraft accidents with catastrophic consequences. From 1976 - 1983 there were a total of 315 reported uncontained rotor failures in commercial, general, and rotorcraft aviation according to the Aerospace Information Report 4003 [56]. One method to mitigate such accidents has been to create a fragment barrier to prevent low-energy fragments from penetrating the fuselage wall and rupturing control lines, power units, or damaging other engines. One proposed system consists of multilayers of high-strength polymer fibers with specified spacing and boundary conditions. The barrier system seeks to minimize added weight and cost by replacing existing materials in the fuselage wall with impact absorbing materials.

Experiments in which projectiles impacted these fabric impediments substantiated that selected fabrics made from strong polymer fibers can absorb significant fragment energy. Additionally, some of these materials appear to have sufficient flame resistance, water absorption resistance, and thermal and

acoustic insulation properties to serve as building blocks for barriers [92, 101] and serve dual functions.

Regulatory organizations, such as the Federal Aviation Administration, require that commercial jet engines must be designed with a system that will not allow any single compressor or turbine blade failure to penetrate the engine case during engine operation. Additionally, jet engine manufacturers must demonstrate that the engine fan blade can be contained within the engine when a blade is released with the engine running at full-rated thrust. The system designed to prevent it from penetrating the engine is called the fan containment system. There are generally two types of fan containment systems, referred to as hardwall and softwall systems. Hardwall systems consist of a relatively stiff section of the engine case that has sufficient strength to prevent penetration if impacted by a blade, resulting in relatively little deflection of the hardwall system during impact. Softwall systems usually consist of a thin inner ring, surrounded by layers of dry fabric, most commonly Kevlar. Between the inner ring and the fabric there is usually some honeycomb structure to provide rigidity to the case. Fan blade failure in softwall systems usually results in large deformation of the fabric [81]. One softwall system concept is in Figure 3.1 with 30 plies of Kevlar and aluminum rods for the system structure [80].

Recent development offers a new material choice for impact protection. Shear thickening fluid (STF) [59, 65] treated Kevlar may be used as the fabric in a softwall containment system. A shear thickening fluid is a non-Newtonian fluid

whose viscosity increases when the shear stress increases. Shear thickening can occur on a large scale such that the fluid will act more like a rigid solid. When saturated into a woven fabric, the unloaded STF fabric will remain flexible. However, upon a projectile impact producing a high strain rate in the fabric, there may be a localized transformation to a near-rigid state, allowing various mechanisms to absorb projectile energy. A STF requires high colloidal concentrations, and the transition can be a factor of the carrier fluid, particle volume fraction, and particle size [24]. Other recent research by the Army Research Laboratory [61, 114] and others [59, 107] suggest that STF treated fabrics may absorb more energy during impact events than neat fabrics. The term 'neat' when describing Kevlar refers to plain fabric that is not mixed with other substances.

The following sections describe a series of experiments in which different projectiles impacted various layers of neat and STF treated Kevlar Style 706 fabric for comparison with future simulations. These experiments provided test results on different projectile geometries, important in this area since published STF experimental work has been with significantly smaller spherical and fragment simulating projectiles [27, 60, 61, 107, 114]. In order to model the behavior of the STF Kevlar under impact loading and validate the model through future simulations, the experiments were necessary to provide the ballistic performance data. Additionally, this investigation helped in the understanding of STF Kevlar's response for larger projectiles. The experimental setup allowed measuring the impact and residual velocities and observing the

projectile interaction with the Kevlar target. The testing apparatus allowed different target boundary conditions and projectile impact experiments: (a) an aluminum cylinder impacting a circular target surrounded by clamped edges, (b) an aluminum cylinder impacting a rectangular target with two clamped edges and two free edges, and (c) a steel disk impacting a circular target surrounded by clamped edges. Additionally, comparisons were made of the neat and STF Kevlar performance as well as boundary conditions. This information is used in a subsequent chapter to correlate simulation and experimental results.

3.2 Materials

3.2.1 Kevlar

The specific Kevlar fabric used in all target constructions was plain-woven Hexcel Schwebel Aramid (paraphenylene terephthalamide) Style 706 fabric (Kevlar KM-2 fiber, 600 denier, 34 yarns per in), commonly marketed for ballistics and protection products. Neat KM-2 fabric construction specifications are in Table 2.1

3.2.2 Shear Thickening Fluid

The shear thickening fluid (STF) used in the following experiments was prepared by the Army Research Laboratory (ARL) and composed of silica particles (Nissan Chemicals MP4540) [43, 60] suspended in polyethylene glycol (PEG 200) [6, 27]; the silica to PEG 200 mass ratio being 2:1. The

mass fraction of the STF in the STF Kevlar composite was 0.200. Rheological measurements have shown that this particular STF undergoes a shear thickening transition at a shear rate of $10^2 - 10^3 s^{-1}$ [60]. It is worth noting that the strain rate of a Kevlar yarn in a typical experiment that follows is $1.11 \times 10^3 s^{-1}$ in the axial direction and $2.70 \times 10^2 s^{-1}$ in the radial direction, well above the transition rate for shear thickening. Neat KM-2 fiber, silica, and PEG 200 properties are in Table 3.1.

3.2.3 Projectiles

Projectiles used in the STF impact tests were a cylinder and disk. The cylinder projectile was Aluminum 6061-T6, 2.54 cm in length, 1.27 cm in diameter, and 8.69 grams. The disk projectile was 4340 steel, 3.81 cm in diameter, 0.635 cm thick, and 56.68 grams.

3.3 Target Preparation and Experimental Procedure

Impregnation of Kevlar by STF was performed by the Weapons and Materials Research Directorate of the Army Research Laboratory [114]. Details of STF target preparation can be found in other literature [27, 60, 61]. STF Kevlar used in the current work was composed of the following constituent mass fractions: 0.8000 for Kevlar, 0.1333 for silica, and 0.0667 for PEG 200. STF preparation increased the original weight of the Kevlar by 25%. Care was taken to minimize exposure of the targets to the environment by keeping the target panels sealed in Ziploc bags until testing.

The University of Texas emplaced all targets in fixtures for consistency and supervised the experiments. Actual operation of test equipment (compressed air gun and cameras) was accomplished by Southwest Research Institute. Aluminum cylinders and steel disks impacted various layers of Kevlar fabric at specified velocities to achieve penetration, SwRI Project No. 18.18054.01.042 and SwRI Fragment Testing of Kevlar Panels, [38, 41]. All impacts were flat-end impacts for the aluminum cylinders and edge impacts for the steel disks at normal obliquity. To minimize fabric slip at the clamped edges of the target, the target frame consisted of steel backing and cover plates with a 20.32 cm circular aperture in the middle. Different cover plates were fabricated for various layers of target material to provide a secure fit and minimize slip between the Kevlar targets and the steel plates. The steel disk projectile tests were only conducted on the circular target with clamped edges. Testing of targets with all clamped edges occurred first. However, due to the results of these tests, the University of Texas redesigned the targets with two clamped and two free edges. A review of the literature showed that previous STF testing occurred with targets with free edges [27, 61]. For the aluminum cylinder projectile tests on two clamped and two free edges of Kevlar, the Kevlar was cut into strips 10.16 cm x 38.1 cm and assembled into the target frame in accordance with the specified number of layers. The Kevlar strips were oriented vertically and centered in the aperture. The Kevlar was tightened to minimize slack, but not stretched, and the cover plate was clamped in place to immobilize the target material. The long edges of the Kevlar strips

were unconstrained. In the clamped edge tests, Kevlar was cut into 38.1 cm panels and assembled between the steel plates, minimizing any slack but not stretching the target material. The plates were held together with C-clamps, Figure 3.2.

The impact tests were performed at Southwest Research Institute (SwRI) using a compressed gas gun with helium as the driver gas to launch the projectiles. The gun consisted of a gas chamber and a twenty-foot square barrel with a 2-inch by 2-inch bore size, Figure 3.3. A sabot trap was located at the muzzle to abruptly stop the motion of the sabot and allow the projectile to continue on toward the target, Figure 3.4. Sabot materials were polystyrene for the aluminum cylinder and Noryl [84] for the steel disk, Figures 3.5 and 3.6. All tests were performed at room temperature. The barrel was aimed on the target center and a laser was used to confirm target obliquity and align the gun with the desired impact location. The impact velocity (V_i) and residual velocity (V_r) of each projectile were measured using video cameras positioned perpendicular to the projectile's direction of travel. The performance of the neat and STF Kevlar could be assessed by evaluating the residual velocities of the projectiles from the corresponding number of layers.

Three Vision Research Phantom V7 monochrome cameras recorded the impact event at 40,000 frames per second with a resolution of 192 x 192 pixels per image. The first camera recorded the impact velocity using a calibration bar to record distance and time. A second camera provided a side view of the target and measured the residual velocity of the projectile after it penetrated

the target. The third camera provided an oblique view of the rear of the target and recorded the target deflection and projectile interaction during each test. Figure 3.7 shows the experimental setup for the STF tests.

3.4 Results of Ballistic Experiments

A series of tests for the aluminum cylinder impacts on one through five layers of neat Kevlar and one through four layers of STF Kevlar were conducted to obtain corresponding residual velocities. First experiments were conducted with all clamped edges of Kevlar for the aluminum cylinder and steel disk impacts. The results of these experiments showed that STF Kevlar actually performed worse than neat Kevlar. Additional tests were conducted with aluminum cylinder impacts on Kevlar with two clamped and two free edges to investigate if STF Kevlar was sensitive to the target configuration. The results of the additional experiments showed that the ballistic performance of STF Kevlar was quite similar to neat Kevlar on a per unit mass basis.

Tables 3.2 and 3.3 summarize the data from the aluminum cylinder impact experiments on Kevlar with all clamped edges and with two clamped and two free edges, respectively. For the steel disk tests, the layers of Kevlar were varied from 3, 6, 12, and 24 layers. Table 3.4 displays the results of the steel disk impacting Kevlar with clamped edges. In some of the experiments, the projectile did not penetrate the target.

The response of the fabric undergoing impact was reflected in general observations of post-impact damage. Post-impact observations of the Kevlar

target revealed lateral movement of impacted yarns relative to the fabric structure, Figure 3.8, but in other cases, especially for the lower V_r/V_i ratios, the damage of impacted yarns included more yarn pull-out. Specific observations of neat and STF Kevlar show minor differences. Neat Kevlar targets revealed slightly more yarn ejection from the unconstrained edges, Figure 3.9, compared to the STF Kevlar targets, 3.10. Additionally, reviews of the impact videos show a debris cloud of STF components following the trajectory of the projectile, Figure 3.11, which was not observed for the neat Kevlar.

3.5 Analysis

3.5.1 Aluminum Cylinder Impact Experiments with Clamped Edges

Results of the aluminum cylinder impact on one through five layers of neat and one through four layers of STF Kevlar are shown in Figure 3.12 for a circular target with clamped edges. The impact velocities were consistent, and the difference of the impact velocities from the averaged high and low impact velocity values can be expressed as a percent by

$$\delta = \frac{V_i - V_i^*}{V_i^*} \cdot 100 \quad (3.1)$$

where V_i^* is the average of the high and low impact velocities

$$V_i^* = \frac{V_i^{high} + V_i^{low}}{2} \quad (3.2)$$

Table 3.2 shows the largest difference of impact velocities was within

9.82% of the averaged high and low impact velocity values. Test 2 was omitted due to an equipment malfunction.

The areal densities of the targets were normalized with the areal density of a single layer of neat Kevlar. In Figure 3.12, the x-axis is the normalized areal density of the target material, reflecting the increased areal density corresponding to the number of layers of neat and STF Kevlar. To compare the impact performance of the neat and STF Kevlar on a per unit mass basis, the ratios of residual to impact velocities were plotted versus the normalized areal densities of the targets. The projectile failed to penetrate the five layer neat Kevlar target. In each case, the experiments performed with all clamped edges showed higher V_r/V_i ratios for the STF Kevlar compared to the neat Kevlar, indicating worse ballistic performance. Figure 3.13 shows an aluminum cylinder impact at 335 m/s on two layers of neat Kevlar. To investigate the effects of target boundary conditions on STF performance, additional tests were conducted and discussed in the next section.

3.5.2 Aluminum Cylinder Impact Experiments with Two Clamped and Two Free Edges

Results of an aluminum cylinder impact on one through four layers of neat and STF Kevlar are shown in Figure 3.14 for a rectangular target with two clamped and two free edges. Table 3.3 shows the largest difference of impact velocities was within 1.57% of the averaged high and low impact velocity values. Tests 1 and 2 were retested (Tests 9 and 10) to achieve experimental

data with constant impact velocities for the different target geometries.

Figure 3.14 shows very minor differences in neat and STF Kevlar ballistic performance when assessed on an equivalent areal density basis. These tests with two target edges clamped and two target edges free indicate that the overall ballistic performance of neat and STF Kevlar is quite similar, for targets of similar areal density, given the specified impact velocity. A comparison of the results with all clamped edges and with two clamped and two free edges shows a slightly better ballistic performance when the target has unconstrained edges. This suggests that the ballistic performance of neat and STF Kevlar is sensitive to the target configuration. Figure 3.15 shows an aluminum cylinder impact at 298 m/s on one layer of STF Kevlar.

Again, given the specific target geometry and fixed impact velocity, there are very minor differences between the neat and STF Kevlar ballistic performances. These small differences suggests that their ballistic performance is quite similar on a per unit mass basis.

3.5.3 Steel Disk Impact Experiments with Clamped Edges

Results of the steel disk impact on 3, 6, 12, and 24 layers of neat and STF Kevlar are shown in Figure 3.16 for a circular target with clamped edges. Table 3.4 shows very consistent impact velocities with the largest difference of impact velocities within 0.57% of the averaged high and low impact velocity values. The ratios of residual to impact velocities for the neat and STF Kevlar layers were plotted versus the normalized areal density of the target as in the

other cases. The projectile failed to penetrate the target in each of the 24 layer tests. Similar to the previous result with all clamped edges, the STF Kevlar was inferior to the neat Kevlar in absorbing the projectile energy for the same areal density. In general, the neat Kevlar performed better than the STF Kevlar when impacted by the steel disk, showing lower V_r/V_i ratios. Figure 3.17 shows a steel disk impact at 294 m/s on three layers of STF Kevlar.

3.5.4 Boundary Conditions

Results of all clamped edges and two clamped and two free edges for the aluminum cylinder impact experiments show a general trend in Figures 3.12 and 3.14. Impacts on Kevlar with all clamped edges resulted in higher V_r/V_i values, indicative of poorer ballistic performance. Overall, the results are consistent with other research that have shown targets with free edges have better ballistic performance than targets with all clamped edges [23, 31, 117]. When all edges are clamped, the target has limited lateral and out of plane movement. On impact, the yarns distort until they reach failure strain and can no longer decelerate the projectile. However, free edges allow greater movement of the fabric, both out of plane and lateral displacements, which decelerates the projectile as the fabric is in contact with the projectile over a greater distance and time. The fabric layers are carried along the path of the projectile, adding mass and drag, when the fabric can deform and envelope the projectile. The processes of yarn axial tension and yarn ejection both contribute to the spatial and temporal spreading of the load and to energy loss

from the projectile. Additionally, as the difference between impact velocity and the target specific V_{50} decreases, boundary condition effects are more significant. In these cases fabric failure is not as localized as single layer targets. This allows the projectile to transfer more energy to the fabric during deformation and allows more time to decelerate the projectile. A higher impact velocity is required to penetrate more layers. This observation is in agreement with other research that show boundary condition effects are more significant at lower impact velocities when the fabric can deform to the boundaries before failure [31, 117].

3.6 Summary

The current work has described a series of experiments consisting of impacts of an aluminum cylinder and steel disk on various layers of neat and STF Kevlar. Results of the experiments will be used for comparison to future simulations and modeling work. Targets consisted of circular panels with all clamped edges as well as rectangular panels with two clamped and two free edges. In general, the neat Kevlar outperformed the STF Kevlar over the limited velocity range tested. These results have provided some observations on boundary condition effects as well as STF performance and will help validate the simulations. These experiments imply STF Kevlar may not be advantageous in the application of softwall containment systems for aircraft turbine blades. Additionally, these low velocity experiments indicate neat and STF Kevlar performance may be target configuration dependent. Boundary

conditions become significant when the impact velocity is close to the V_{50} and the constrained target system has limited mobility to deform and absorb the projectile's energy. Results of these experiments have provided a database for experimental target geometries and boundary conditions over a consistent impact velocity for neat and STF Kevlar impacts. Additionally, these experiments provided information on different projectile geometries, important in this area since published STF experimental work has been with significantly smaller spherical and fragment simulating projectiles.

Several conclusions specific to this STF impact testing and modeling on Kevlar fabric are suggested: (1) additional experiments should be conducted to investigate further the effects of different STF mass fractions and boundary conditions, (2) additional material testing on STF is needed to provide material properties for impact damage modeling, and (3) additional experiments should be performed over a wider range of impact velocities and number of layers to validate future computational analysis methods and simulations.

Table 3.1: Properties of STF Kevlar constituents used in experiments

Property	Neat KM-2 fiber		Silica		PEG 200	
		Ref		Ref		Ref
Mass fraction	0.8000		0.1333		0.0667	
Density (g/cm^3)	1.45	[33], p.3	2.22	[66], p.321	1.1239	[6]

Table 3.2: Experimental results: aluminum cylinder impacts on neat and STF Kevlar with all edges clamped

Test #	Type	Number of Layers	V_i (m/s)	δ (%)	V_r (m/s)	V_r/V_i
3	Neat	1	375	9.82	366	0.976
4	Neat	2	335	-1.79	305	0.909
5	Neat	3	308	-9.82	227	0.738
6	Neat	4	351	2.77	268	0.764
1	Neat	5	335	-1.79	0	0.000
7	STF	1	361	5.80	348	0.965
9	STF	2	367	7.59	344	0.938
10	STF	3	366	7.32	321	0.876
12	STF	4	357	4.64	306	0.856

Table 3.3: Experimental results: aluminum cylinder impacts on neat and STF Kevlar with two edges clamped and two edges free

Test #	Type	Number of Layers	V_i (m/s)	δ (%)	V_r (m/s)	V_r/V_i
9	Neat	1	306	1.57	288	0.941
10	Neat	2	303	0.66	253	0.833
3	Neat	3	299	-0.76	211	0.705
4	Neat	4	297	-1.57	0	0.000
5	STF	1	298	-1.06	285	0.956
6	STF	2	301	-0.25	267	0.887
7	STF	3	298	-1.16	0	0.000
8	STF	4	297	-1.57	0	0.000

Table 3.4: Experimental results: steel disk impacts on neat and STF Kevlar with all edges clamped

Test #	Type	Number of Layers	V_i (m/s)	δ (%)	V_r (m/s)	V_r/V_i
8	Neat	3	297	0.57	283	0.956
13	Neat	6	295	-0.05	256	0.868
15	Neat	12	295	0.16	213	0.721
17	Neat	24	293	-0.57	0	0.000
11	STF	3	294	-0.36	273	0.929
14	STF	6	296	0.36	272	0.920
16	STF	12	294	-0.47	265	0.903
18	STF	24	297	0.57	0	0.000

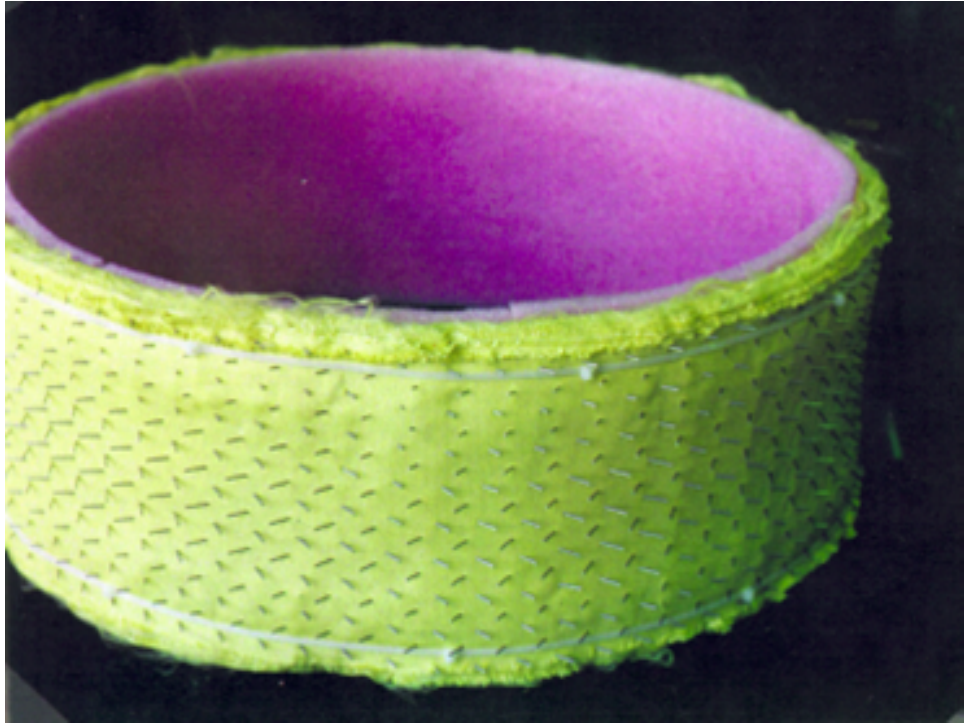


Figure 3.1: Softwall fan containment system concept [80]

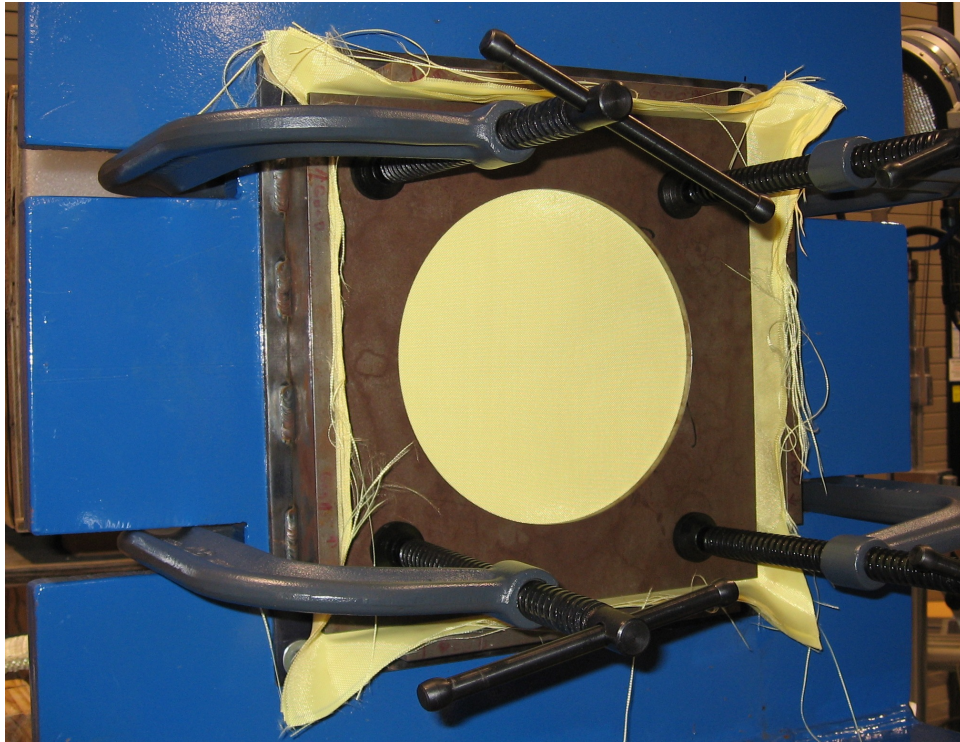


Figure 3.2: Target frame for the aluminum cylinder and steel disk impact tests on Kevlar with clamped edges



Figure 3.3: Southwest Research Institute (SwRI) compressed gas gun



Figure 3.4: Sabot trap with a steel disk projectile sabot

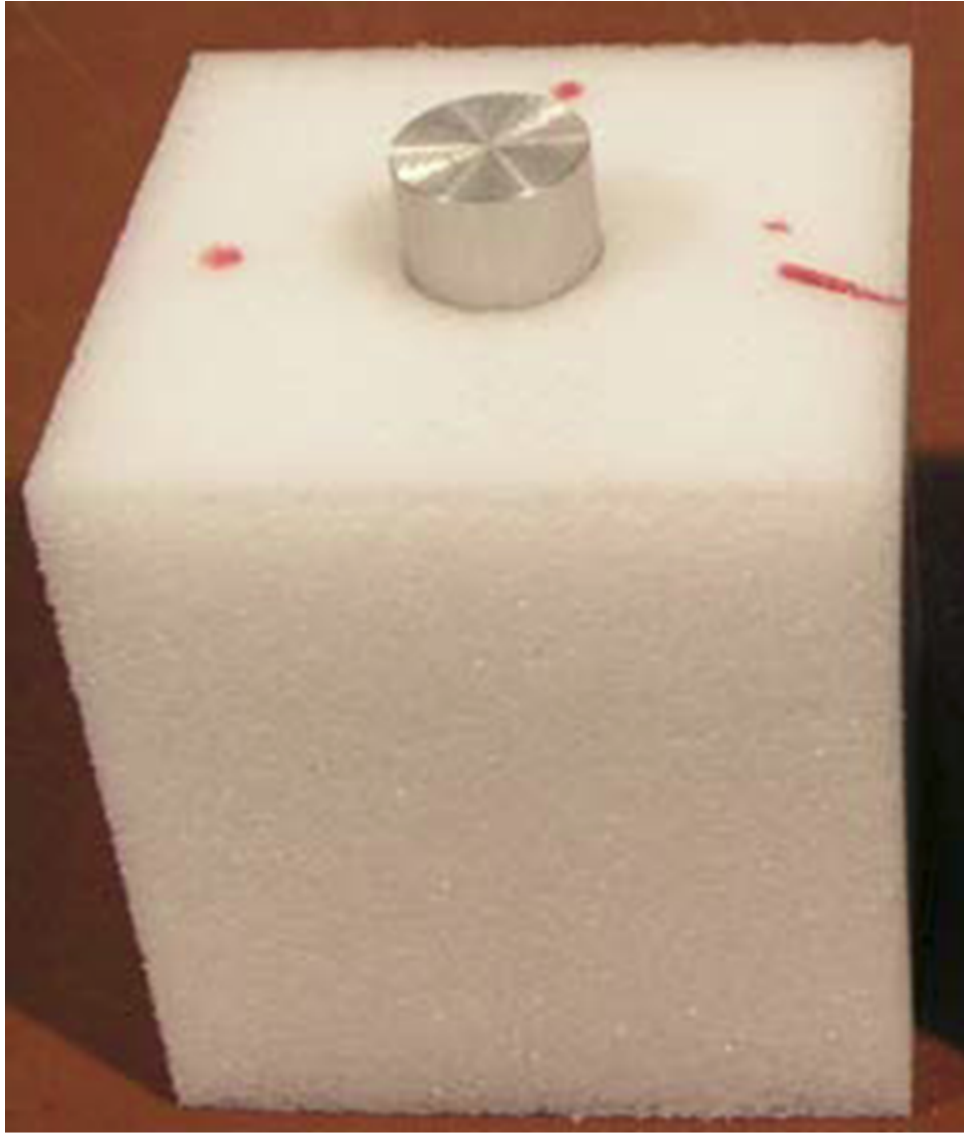


Figure 3.5: Aluminum cylinder projectile and polystyrene sabot [38]

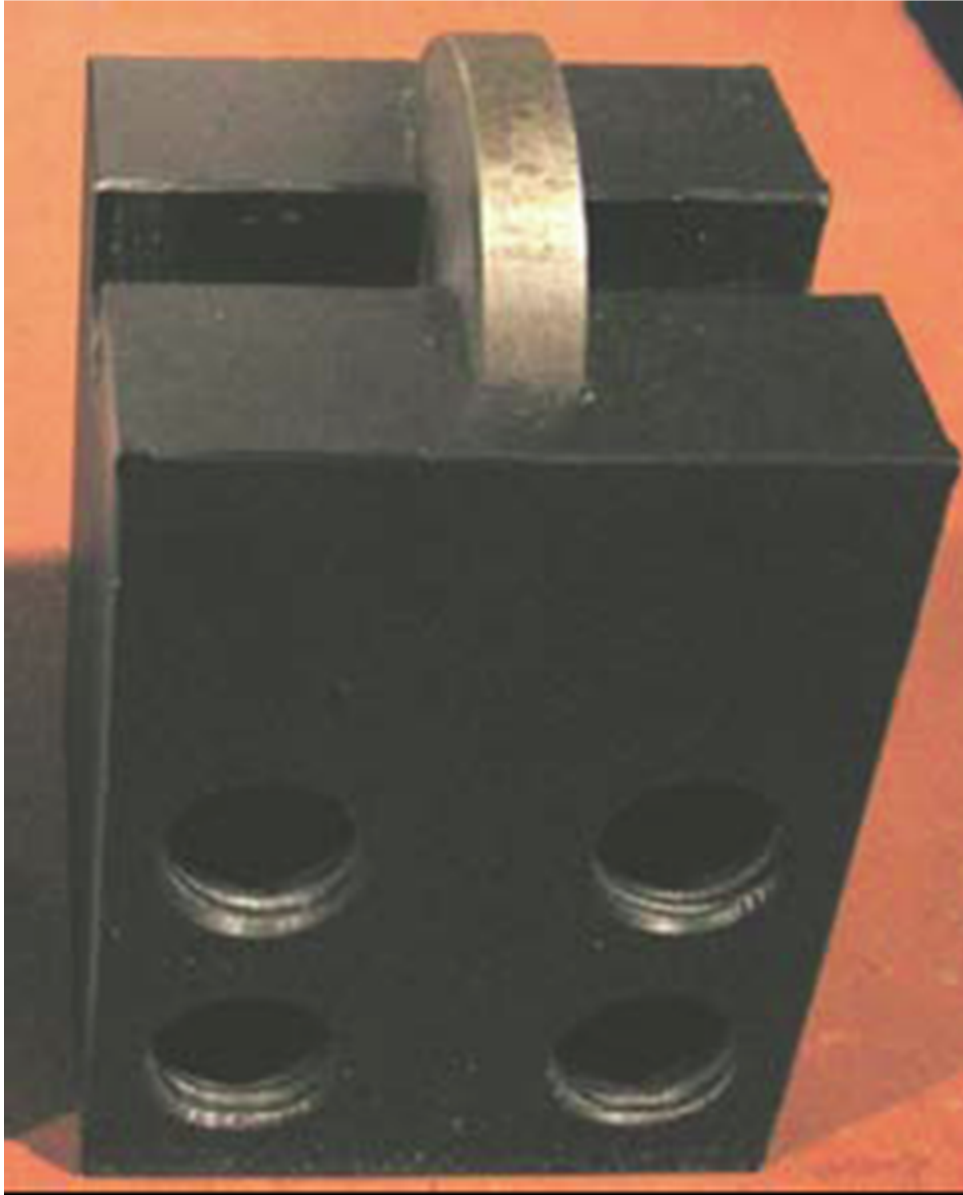


Figure 3.6: Steel disk projectile and Noryl sabot [38]

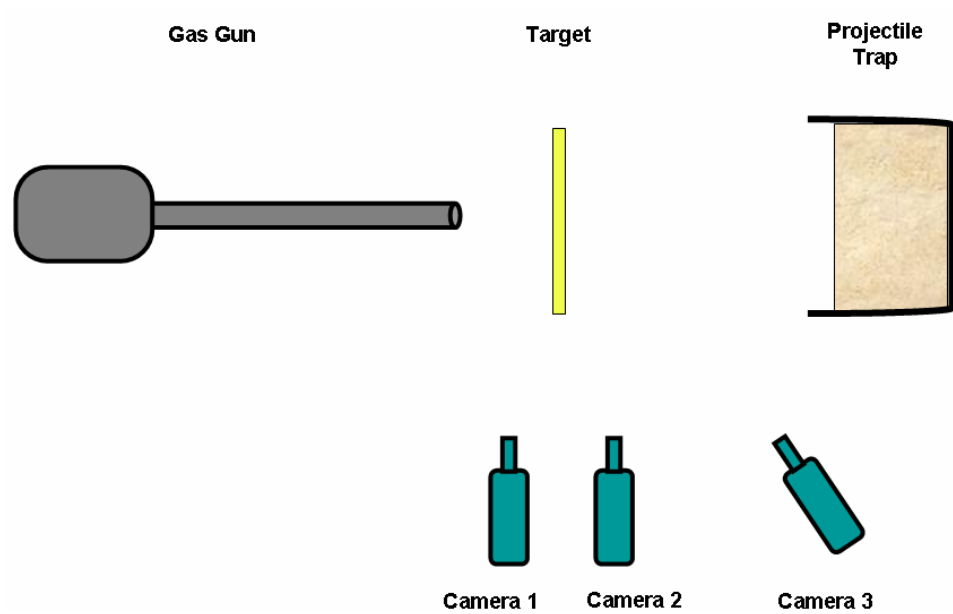


Figure 3.7: Experimental setup for the STF impact tests



Figure 3.8: Post-impact damage by a steel disk projectile

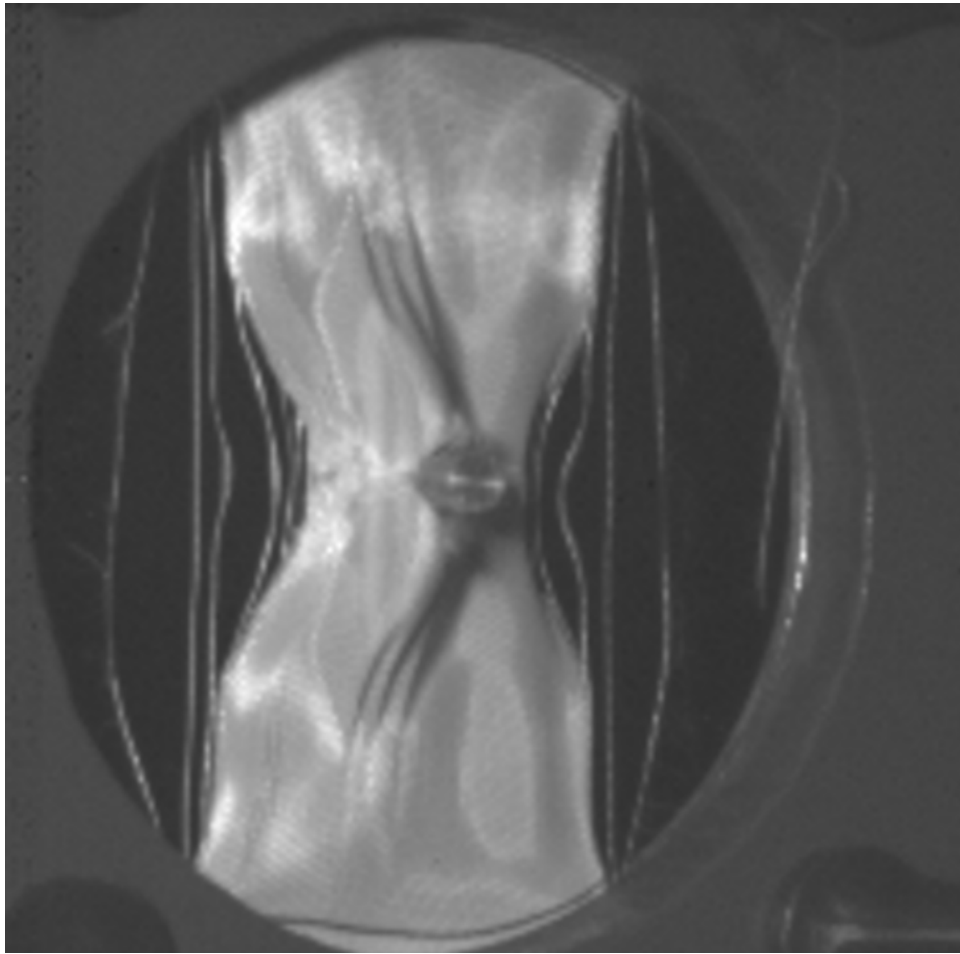


Figure 3.9: Yarn damage from an aluminum cylinder projectile impact on one layer of neat Kevlar

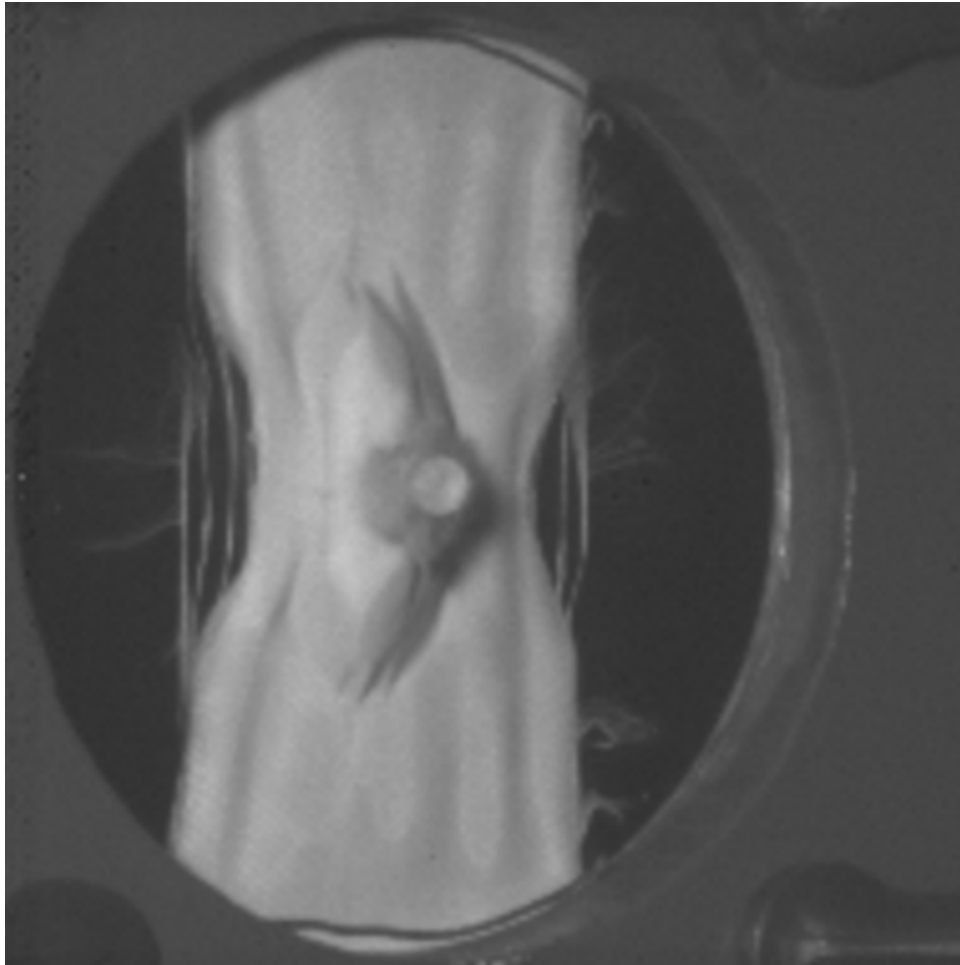


Figure 3.10: Yarn damage from an aluminum cylinder projectile impact on one layer of STF Kevlar

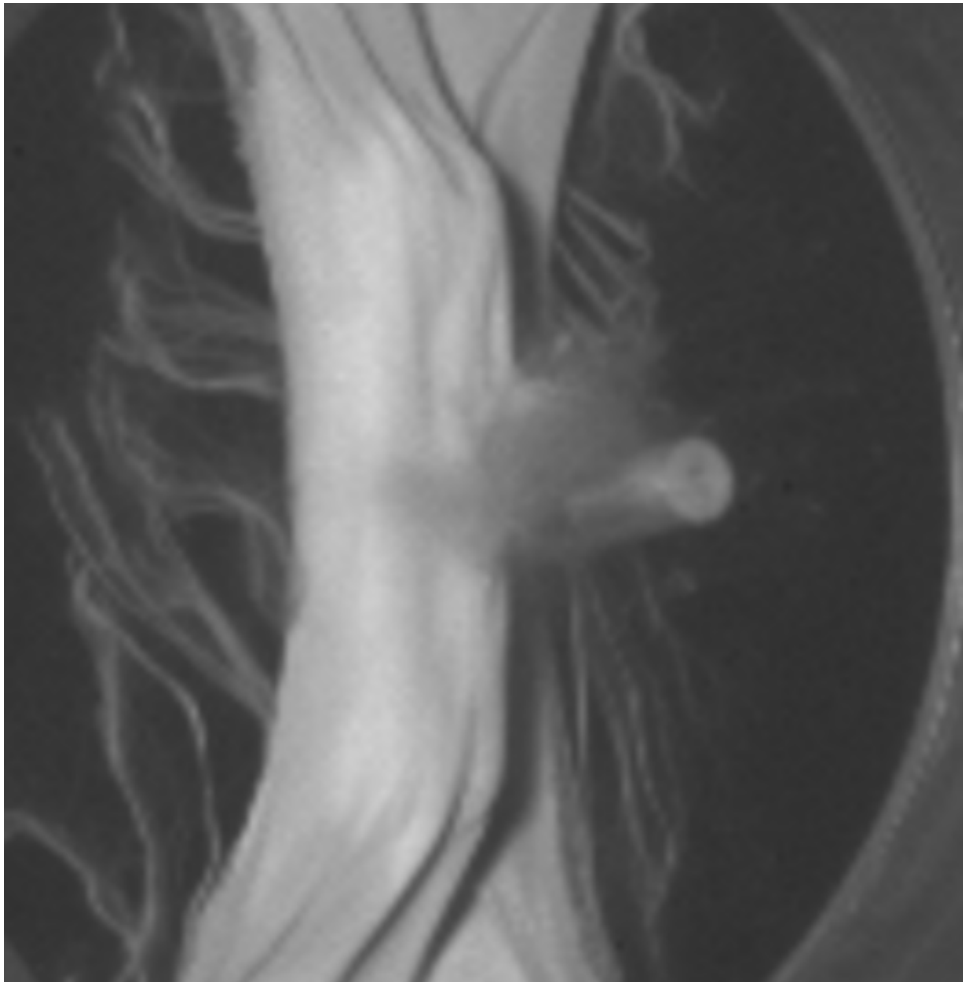


Figure 3.11: STF debris cloud from an aluminum cylinder projectile impact

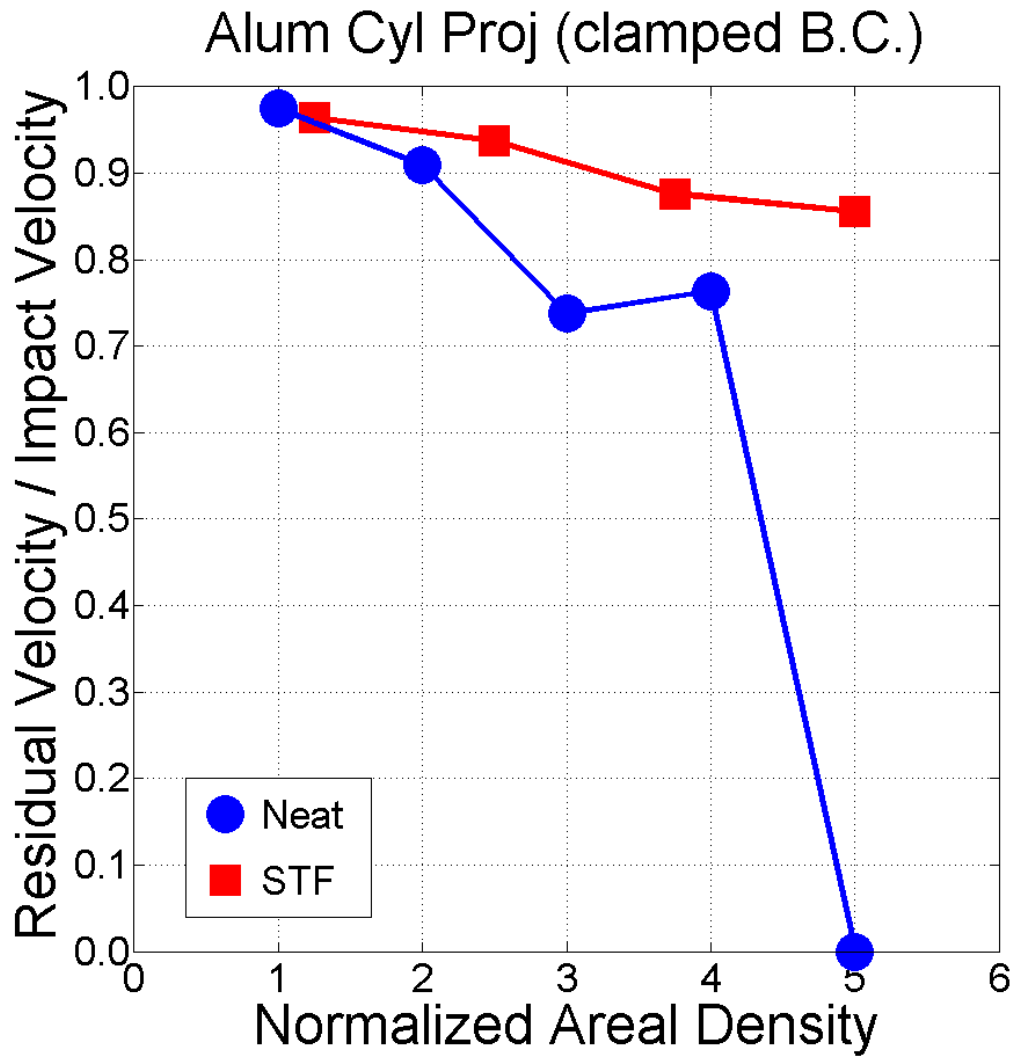


Figure 3.12: Comparison of aluminum cylinder impacts on neat and STF Kevlar with all clamped edges

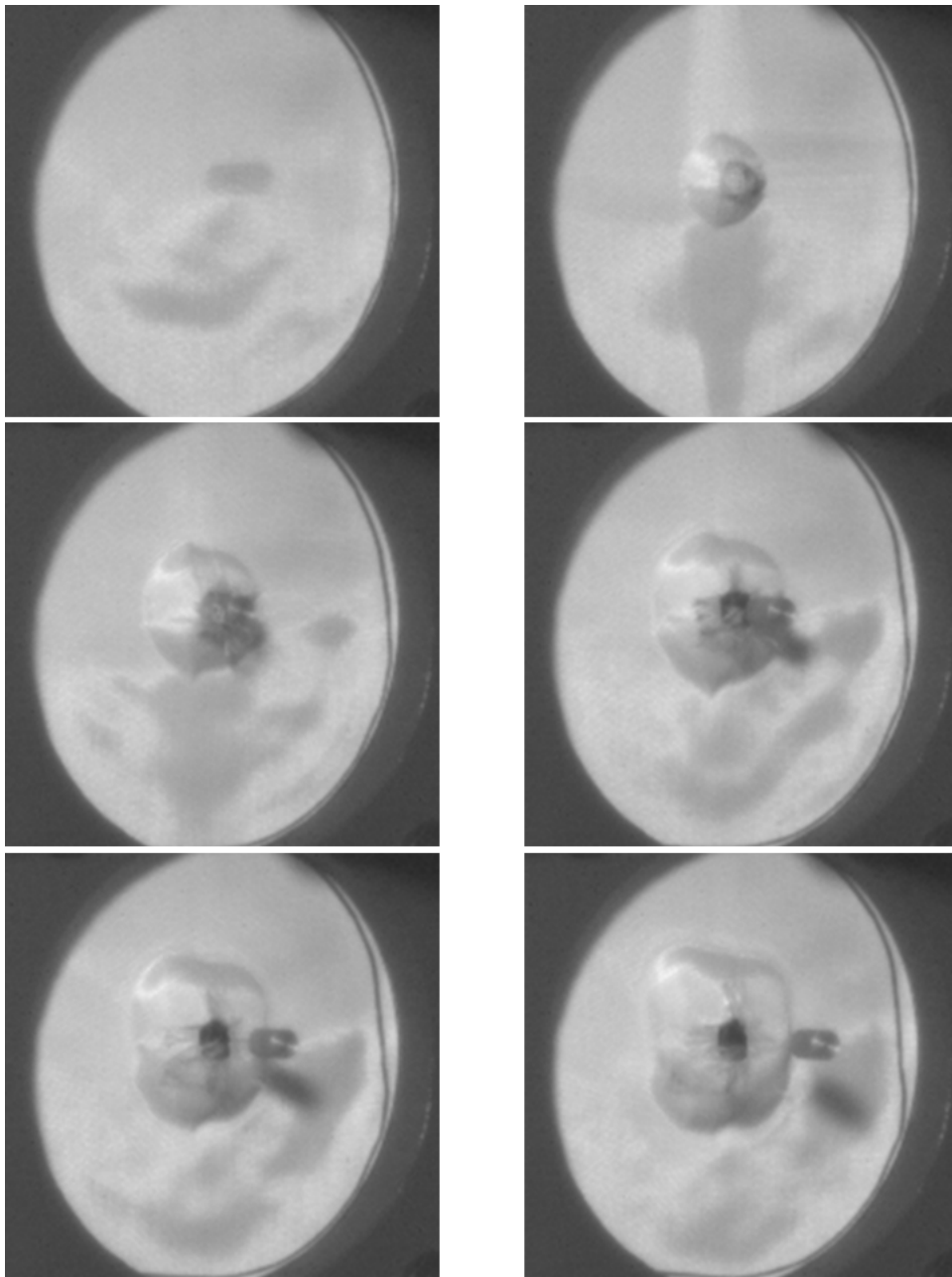


Figure 3.13: Images of an aluminum cylinder impact at 367 m/s on two layers of STF Kevlar with all clamped edges

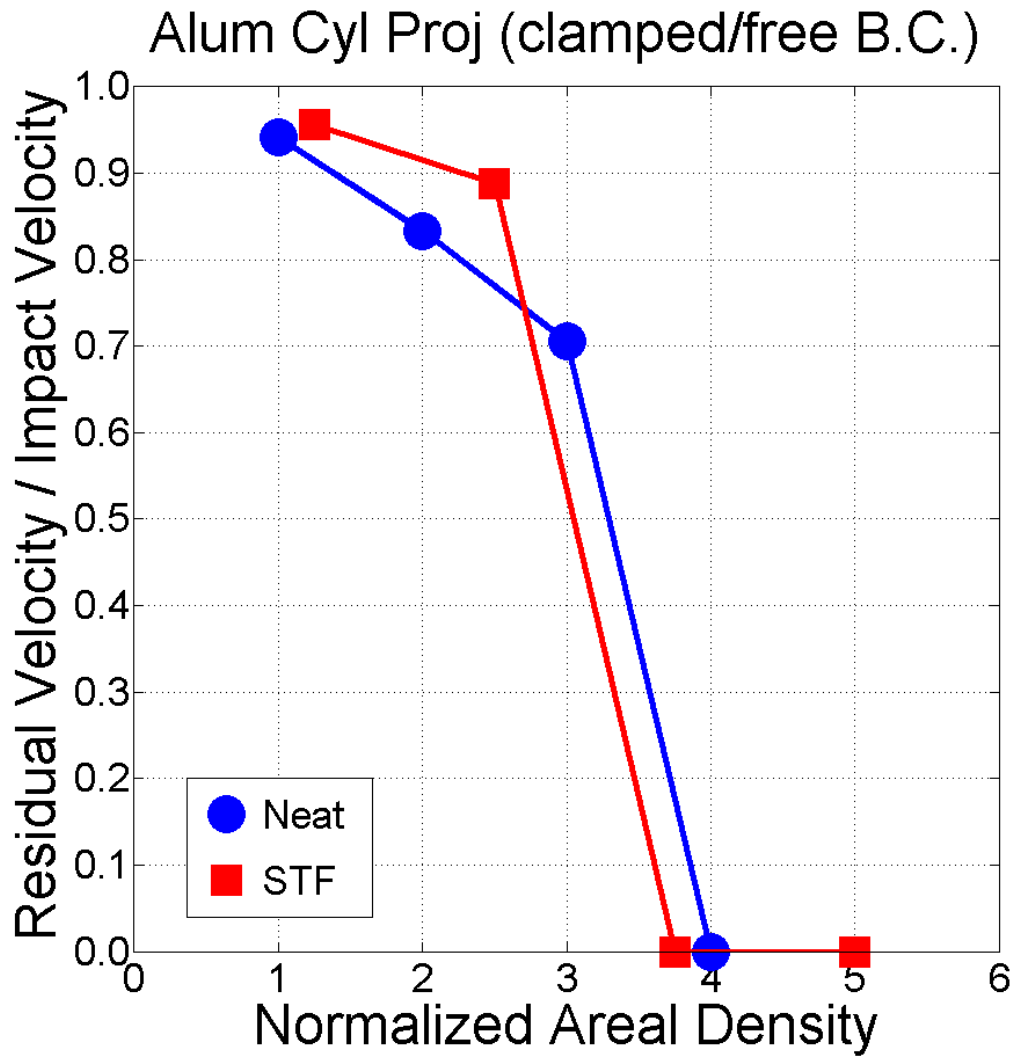


Figure 3.14: Comparison of aluminum cylinder impacts on neat and STF Kevlar with two clamped and two free edges

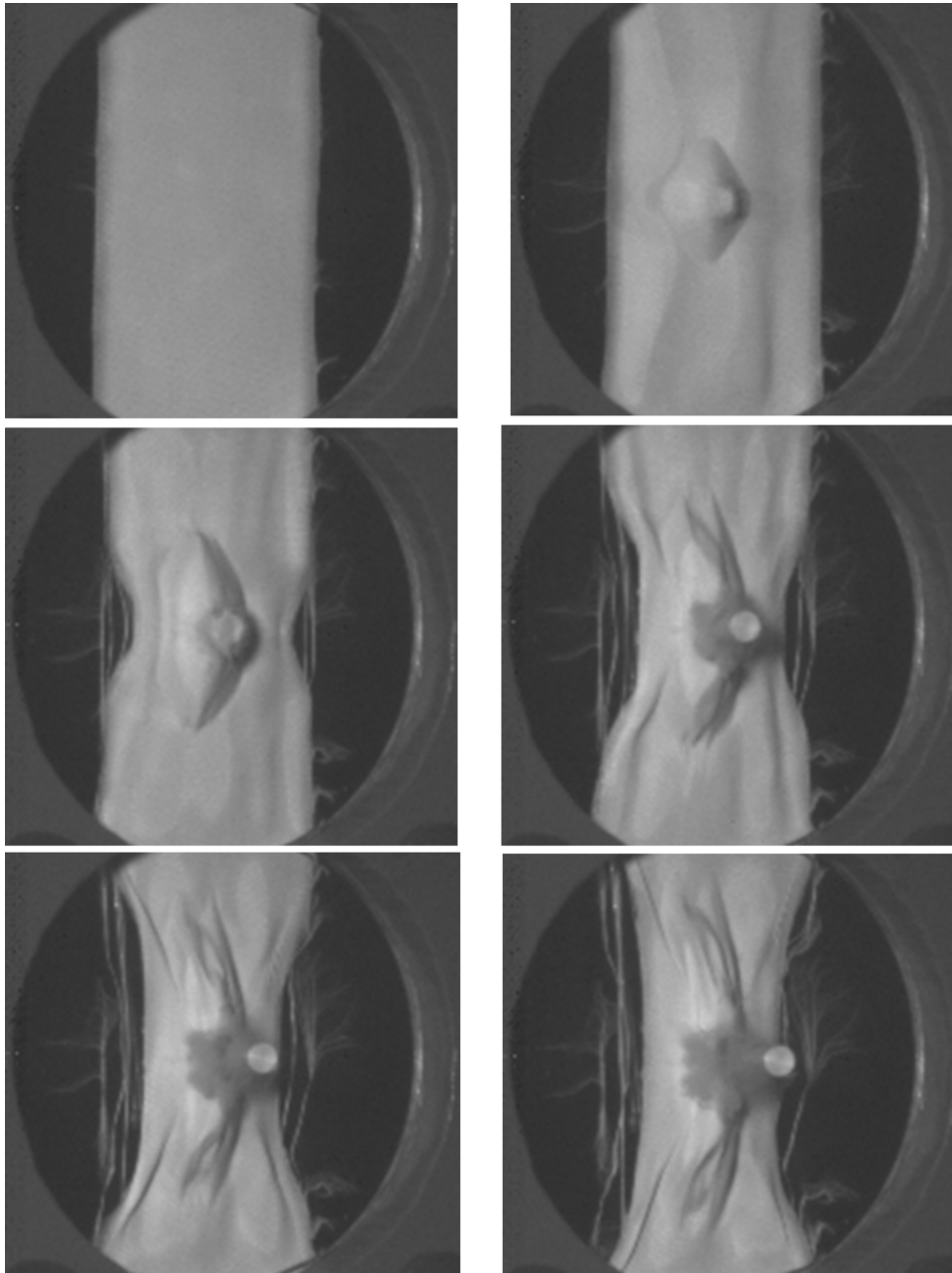


Figure 3.15: Images of an aluminum cylinder impact at 298 m/s on one layer of STF Kevlar with two clamped and two free edges

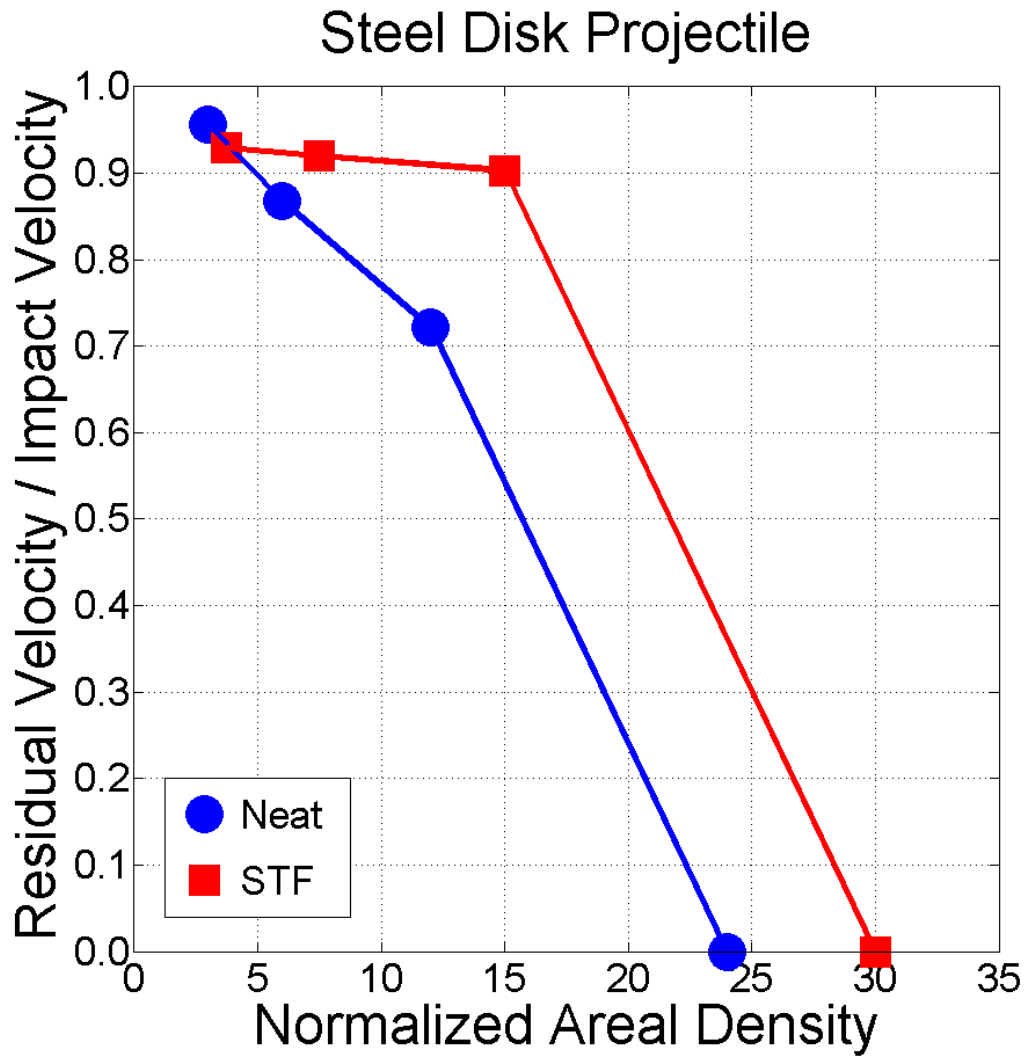


Figure 3.16: Comparison of steel disk impacts on neat and STF Kevlar with all clamped edges

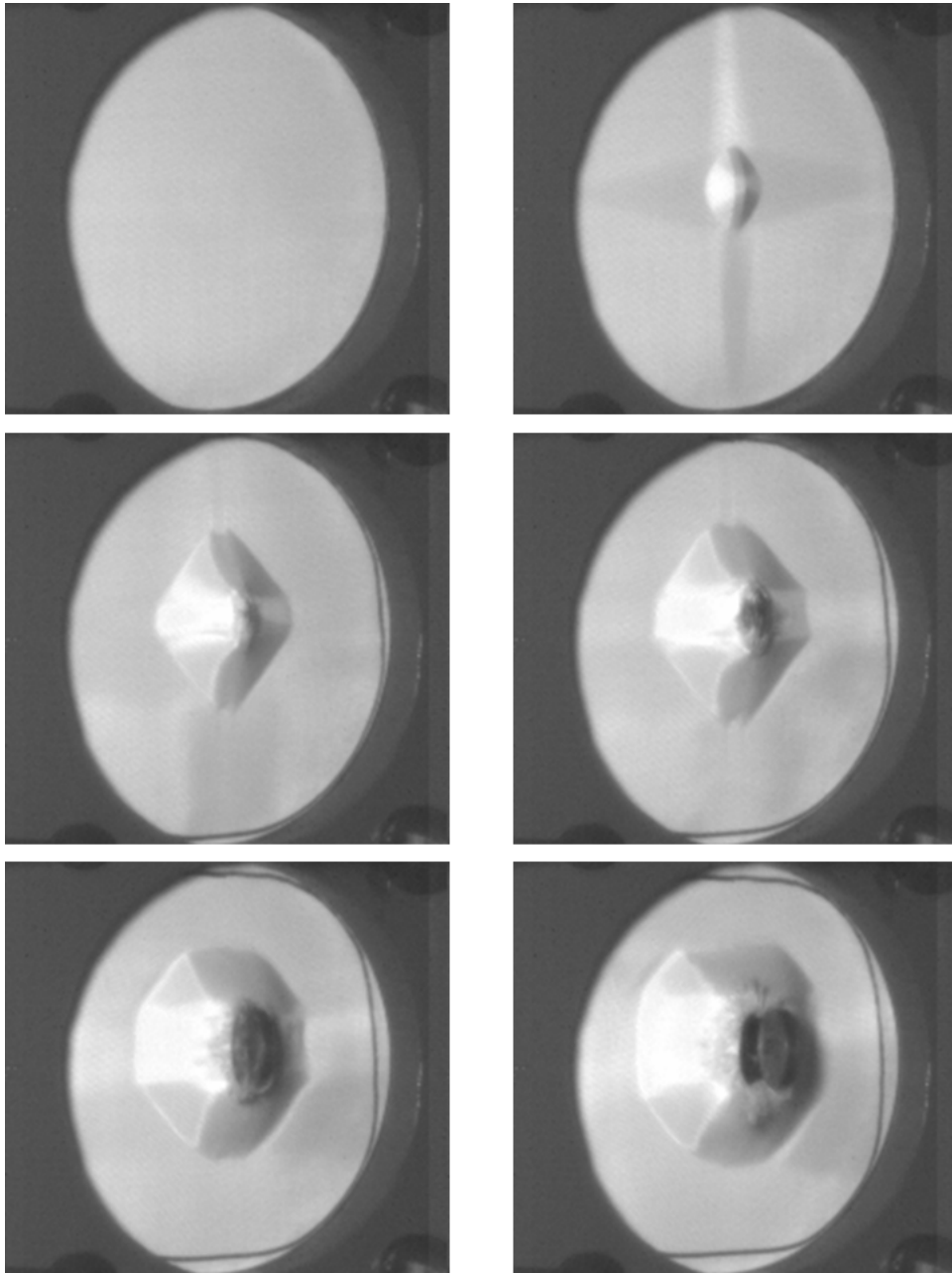


Figure 3.17: Images of a steel disk impact at 294 m/s on three layers of STF Kevlar with all clamped edges

Chapter 4

Development and Validation of a Hybrid Particle-Element Mesomechanical Model for Kevlar Fabric

4.1 Introduction

Woven fabrics made from high-strength fibers, such as Kevlar, Zylon, and Spectra have been widely used in flexible armors such as bomb suppression blankets, Explosive Ordnance Disposal (EOD) bomb disposal suits, and ballistic vests. Improvements in soft ballistic armor have grown as materials science has introduced new advanced materials to meet demands of mass efficient systems that provide improved ballistic protection. However, progress in soft armor systems that contain advanced materials such as Kevlar, Spectra, and Dyneema is often a product of experiments [14, 19, 87]. These experiments are useful but account for only a limited range of impact conditions. Many of the threat projectiles encountered by military and law enforcement personnel and even containment systems are generated from explosions and involve projectile geometries not yet tested. Extrapolation of the data as a means to predict ballistic performance for the given target geometry beyond the experimental velocities is difficult. Likewise, some ballistic performance parameters require extensive testing. For instance, testing for the ballistic limit of a system re-

quires repetitive trials to find the threshold velocity which allows penetration 50% of the time. Predicting the ballistic limit based on experimental results to an estimated value saves considerable time and resources by shortening or eliminating bracketing procedures.

Similarly, modeling the experimental data is another means to predict ballistic protection with different impact conditions. Although some models may adequately predict specific behaviors from fabric characteristics [71], others are often limited to certain types of materials or impact conditions [96]. Ballistic armor designs employing different fabric types in multiple layers are now commercially available, and developing models to predict the ballistic performance of these systems is of growing importance [13]. Likewise, with increased computational capability and experimental constraints, there is a greater need to develop impact models to take advantage of the computational resources. The geometry and properties of the fibers within the yarn, and the yarns within the fabric, create a complex system of deformation. Cork and Foster recently commented that, due to the complexity and uncertainty of projectile/fabric interaction, precise prediction of Kevlar performance, especially where the projectile size is small compared to the yarn size and spacing, is difficult [23].

Numerical modeling and simulations of fabric protection systems is not novel. However, the resolution that can be achieved has been significantly improved as computational capabilities have advanced. By taking advantage of readily available scientific computing, one can start directly at the microscale,

using simple descriptions of the materials to simulate realistic responses of structural fabric. Extending these simple structural elements, one can build an entire structure of woven fabric. The advantage is that simple microscale models can be used with the analysis shifted to more rapid computation [120]. However, very detailed finite element models may require significant time for results or lack other parameters. For instance, Zylon yarn has been modeled as a finite element yarn structure with eight brick elements in the cross section and 12 elements along a crimp wavelength. The computational costs of this particular representation has limited simulations to small geometries on the order of one square inch or less [101].

Nevertheless, simulations are a valuable tool as an adjunct to experimental work when testing facilities and resources are expensive or have limited availability. To be of practical use, a model must meet certain requirements to include:

- 1) The model must accurately predict the Kevlar response under ballistic loading conditions, predicting the macroscopic response of the Kevlar and capturing the deformation mechanisms at the structural level, such as yarn interaction. This ability allows the model to serve as an analysis and design tool for different impact conditions.
- 2) The model must be able to accurately predict the Kevlar's response within a reasonable time with current computational resources.

Advanced ballistic armor systems often use composite materials and

include multilayer geometry. Experiments performed by Grosch at Southwest Research Institute (SwRI) [39, 40] illustrated the efficacy of Kevlar as a material suitable for ballistic protection. Accordingly, the development of a validated computer code to model and design future ballistic protection concepts is nontrivial. Soft armor systems distribute the impact load over a larger area due to the deformation of the fabric and generally increase the computational cost of the simulation.

Previously published articles suggest several models based on their idealization of the materials. First, finite element models are the most common, often employing hex elements to represent the entire fabric or even individual yarns [31]. Another finite element model is a membrane model for the yarns [9]. More recent finite element modeling work has used bar elements for the yarn material [25, 47]. Second, particle models have been used to represent the fabric in some simulations [76]. Most recently, Digital Element Analysis has been introduced to model fibers and yarns [119]. A more appropriate discussion of the model scales will elaborate the differences of these model types.

At the fabric level, finite element membrane models such as those used by Lim et al. [63] and Phoenix [83] do not account for yarn interactions. These membrane models treat the fabric as continuum of finite elements and lack the details of the intricate weave pattern of the yarns. This representation allows the multiple layer geometries to be modeled as a single layer [83]. This approach neglects the interaction of the yarn structure in order to predict

the bulk response of the Kevlar at a low computational cost [52]. This simplification cannot account for yarn interactions which influence the ballistic performance of the system, suggested in experiments and research by Briscoe and Motamedi [16]. Another method used to model fabric includes a pure particle model [76]. This method represents the fabric as an assembly of geometrically spaced particles, which like membrane models, does not represent the medium at the yarn level.

At the yarn level, current models can replicate the weave pattern of particular fabrics. Finite element models (FEM) such as those used by Duan et al. [31] and Raftenberg [87] and Blankenhorn et al. [14] often employ hex elements at the yarn level in commercial packages such as LS-DYNA3D. They consider the Kevlar as a complex yarn structure of discrete elements, and the response of the Kevlar target is calculated from the interaction of the structural components [31, 63]. This approach captures the physics of the Kevlar deformation mechanisms at the expense of high computational costs but has the ability to model the ballistic response at the structural level as well as fabric nonuniformity [77]. However, these hex elements have inherent bending stiffness problems for the modeled yarn. Finite element models representing the individual yarn as a membrane [9] cannot capture the detailed yarn dynamics. Another FEM approach is to employ bar elements to represent the yarns, but these models represent the yarn crossovers with pin-joints [47] or springs [25], neglecting the sliding interface between the yarns. These finite element models also have mass and energy discard issues associated with failed

elements that may be important on multiple layer geometries. Additionally these models must use slideline and erosion algorithms for contact impact and large distortions. More recently, Digital Element Analysis (DEA) has been introduced by Zhou et al. to represent the yarns as multiple fibers [119]. Here, very small rod elements are connected and allow the “chain” to be flexible; however, DEA lacks a thermo-mechanical formulation. Current DEA work involves improving the code through parallelization for large scale computations and validating with experimental data [19].

The modeling approach used in the present work was an extension of a hybrid particle-element method previously used for hypervelocity impact simulations [36]. Particles model all thermo-mechanical effects, inertia, and contact-impact in compressed states, and elements are used to model all strength effects to include tensile inter-particle forces and deviatoric elastic-plastic deformation, see Figure 4.1. Advantages to the hybrid particle-element method over pure finite element methods [42] include no material loss after element failure and no slideline or rezoning issues are necessary. Additionally, no particle-to-element contact-impact models are required as in coupled particle-element methods. The hybrid particle-element method also avoids tensile instability problems associated with pure particle methods [50]. However, this particular particle-element method does not include the mesomechanical geometry to capture the interyarn interactions necessary in this class of contact-impact events.

This dissertation has extended previous work by developing particle-

bar elements to represent the yarn structure, avoiding the bending stiffness associated with hex elements. Material modeling work consisted of a rate dependent strength model for the Kevlar yarn. High velocity impacts involve high strain rate loading, so any material model parameter dependent on strain rate is important to predict system performance. Once a rate dependent strength model was developed, simulations were run to validate the model against known experimental data. The simulations described in this chapter model the experiments performed at Southwest Research Institute [40], SwRI Project No. 18071.02.001, in which a 1.1 gram fragment simulating projectile (FSP) impacted Kevlar targets described in Chapter 2. Simulations were performed on one, two, and four layers of Kevlar targets in order to validate the model with multiple layer targets over a range of velocities. The simulations presented in this work used a Mie-Gruneisen equation of state. Material properties used in the simulations are in Table 4.1 [28, 45, 58, 105]. Simulation work appears to accurately estimate the protection provided by multilayer Kevlar targets.

4.2 Geometry

The Kevlar fabric used in the experimental work and modeled at the yarn level was Hexcel Schwebel Style 706 fabric (Kevlar KM-2 fiber, 600 denier, 400 fibers per yarn, 34 yarns per inch), Figure 4.2. Denier refers to the unit of linear density, equal to the mass in grams of 9000 m of textile strand [4]. In order to replicate the Kevlar-Kevlar and projectile-Kevlar interactions,

the Kevlar was modeled as a system of woven particle-bar elements, capturing the mesoscale structure of the Kevlar yarns. The particles can interact through tension between the connecting particles and through contact with each other. Bar elements were modeled by connecting the nodal coordinates of the particles.

One important characteristic of Kevlar fabric is the crimp in the yarns caused by the weaving process as the yarns pass alternately over and under orthogonal yarns. Hence, the length of the yarn in the fabric is less than the length of the straightened yarn once removed [3]. Crimp is defined as the undulations, waviness, or succession of bend, curls, or waves in the strand induced either naturally, mechanically, or chemically [4]. Crimp is calculated as a percentage by ASTM D 3883-04 with the following equation

$$C = 100 \left(\frac{Y - F}{F} \right) \quad (4.1)$$

where F is the distance between bench marks on the yarn in the fabric, and Y is the average distance between bench marks on the yarn after removal from the fabric and straightening under tension [5]. When a Kevlar yarn is placed in tension to eliminate crimp and then relaxed, the Kevlar yarn restores its waviness pattern, Figure 4.3, implying the crimp is a feature of woven yarn that contributes to a projectile's energy loss when the woven yarn is impacted.

Yarn crimp is a distinctive characteristic of woven Kevlar and has an important effect on the fabric response to impact loading. When a projectile

strikes the Kevlar, the crimped yarns straighten in the initial stage of fabric deformation, offering slight resistance to the projectile. The Kevlar really begins to resist the projectile when the yarns straighten due to tension and begin to elongate [108, 109].

In the current work, the ellipsoid particles are elastically coupled by torsional springs. The particles represent a continuous surface, resisting interpenetration of the yarns. By coupling the particles within a yarn, the modeled geometry prevents free rotation of the particles. The Kevlar yarn is modeled as a system of these particles connected by extensible bar elements. The elements are formed by connecting the nodal particle center of mass coordinates. The elements model tensile forces and strength effects, while the particles model all contact-impact, inertia, and thermodynamics. Particles and elements are used together simultaneously, but they model different physical effects in the same material.

4.2.1 Modeled Yarn Geometry

Figure 4.4 shows a cross section of the Kevlar fabric and the geometry of the yarn comprised of the ellipsoidal particles [98]. The warp yarns run the length of the fabric [4] in the x-direction. Fill yarns run across the fabric at right angles to the warp yarns [4] in the z-direction. The warp and fill yarns are woven to form the fabric. In Figure 4.4 a side view of a warp yarn is detailed for clarity with the modeled particles connected at the nodal coordinates to form the yarn structure. As the warp yarn traverses the orthogonal fill yarns to form

a woven fabric, it passes over and under the fill yarns. At the point where the warp yarn changes from being above to below a fill yarn, the fabric is modeled as being only one particle thick to allow the continuous yarn to represent the woven structure. The particles' center of mass separation distances are denoted by the dimensions l_i . This section describes the numerical development of the particle and yarn geometries.

The initial geometry of the yarns is determined from the crimp in the yarn and the fabric thickness, t . In Figure 4.4, the fabric thickness further defines the center of mass separation distance, $2l_2$ where

$$2l_2 = \frac{t}{2} \quad (4.2)$$

Using Figure 4.4, let d represent the diagonal length from the centers of mass of a top warp particle to its nearest bottom warp particle. The ratio of the lengths of a crimped yarn ($d + 2l_1$) and an uncrimped yarn (i.e. straightened) ($6l_1$) can be expressed in terms of the crimp

$$\frac{d + 2l_1}{6l_1} = 1 + C \quad (4.3)$$

and the equation can be further simplified to

$$\frac{d}{l_1} = 6(1 + C) - 2 \quad (4.4)$$

The diagonal length d can be calculated as

$$d^2 = (2l_2)^2 + (4l_1)^2 \quad (4.5)$$

and rearranging

$$\left(\frac{d}{l_1}\right)^2 = \left(\frac{2l_2}{l_1}\right)^2 + 16 \quad (4.6)$$

Substituting Equation 4.4 into the previous result yields

$$\left(\frac{l_2}{l_1}\right)^2 = \frac{1}{4} [6(1 + C) - 2]^2 - 4 \quad (4.7)$$

With the crimp defined and the separation distance in the direction of the particle's minor radius ($2l_2$) determined from the fabric thickness, the separation distance in the particle's major axes direction ($2l_1 = 2l_3$) can be calculated from the previous relationship. The ratio of nodal separation distances

$$\Phi = \frac{l_1}{l_2} \quad (4.8)$$

is a specific quantity determined by the crimp and specific thickness. With the specified nodal geometry, a system of these particles can accurately represent a woven yarn and a layer of fabric, keeping the integrity of the high yarn aspect ratio and fabric thickness. In the current work for Kevlar KM-2 Style 706, the modeled fabric geometry consisted of yarns that were two particles wide, and woven so the particle structure repeated every three particles in length, Figure 4.4. By the method described above where the fabric thickness and crimp were specified values, the modeled Kevlar fabric was represented by 39 yarns per

inch, and the ratio of nodal separation distances (Φ) was 1.887. Alternative geometries can be applied to change the model resolution without changing the basic modeling approach.

Given the ellipsoidal particles and yarn structure, different schemes can be used to model the yarn geometry. The method described above, of specifying the thickness of the yarn and use the crimp specifications, determines the number of yarns spanning a unit length of fabric. Another method is to specify the number of yarns per length and then use the crimp to calculate the fabric thickness in the model. Another method is to use the number of yarns per inch and the thickness to calculate the crimp. Each way has a trade-off of either inexact yarns per unit length, inexact thickness, or inexact crimp. The present work employed the first method where the fabric thickness and crimp specifications were used to calculate the yarns per unit length of fabric. These results allowed the model to simulate the fabric with the correct thickness and yarn crimp, but with a slightly different number of yarns per unit length. By using this approach, the ratio of the nodal separation distances (Φ) was used to determine the particle geometry in the next section.

4.2.2 Modeled Particle Geometry

Dimensions of the ellipsoid particle's semi-axes lengths (h_i) can be calculated by analysis of a representative volume of the yarn model. Let V equal the bulk volume of the geometry represented by dimensions $2l_1$, $2l_2$, and $2l_3$

$$V = 8 l_1 l_2 l_3 \quad (4.9)$$

and the volume of a particle in the bulk volume is

$$V_p = \frac{4}{3}\pi h_1 h_2 h_3 \quad (4.10)$$

With the ratio of nodal distances (Φ) defined in the previous section and keeping the same ratio for the particle half-lengths of the principal axes, substitution yields

$$V = 8\Phi^2 l_2^3 \quad \text{where } l_1 = l_3 = \Phi l_2 \quad (4.11)$$

$$V_p = \frac{4}{3}\pi\Phi^2 h_2^3 \quad \text{where } h_1 = h_3 = \Phi h_2 \quad (4.12)$$

Equating the bulk volume to the particle volume and solving for the particle half-length of the principal axis h_2

$$h_2 = \left(\frac{6}{\pi}\right)^{\frac{1}{3}} l_2 = \left(\frac{6}{\pi}\right)^{\frac{1}{3}} \frac{t}{4} \quad (4.13)$$

Since Kevlar yarn is composed of many individual fibers, the yarn contains voids. Let \hat{V} represent the true volume with porosity ϕ

$$\hat{V} = V(1 - \phi), \quad V_p = \frac{4}{3}\pi h_1 h_2 h_3 \quad (4.14)$$

For the volume of a particle representing the true yarn volume, the particle's half-lengths of the principal axes are represented by \hat{h}_i

$$\hat{V}_p = \frac{4}{3}\pi\hat{h}_1\hat{h}_2\hat{h}_3 \quad (4.15)$$

Letting $h_2 = \hat{h}_2$ allows the particle geometry to represent true fabric thickness.

Substituting and solving for the true volume gives

$$V(1 - \phi) = \frac{4}{3}\pi\hat{h}_1\hat{h}_3h_2 \quad (4.16)$$

and dividing by the bulk particle volume yields the following

$$(1 - \phi) = \frac{\hat{h}_1}{h_1} \frac{\hat{h}_3}{h_3} \quad (4.17)$$

If two of the particle half-lengths of the principal axes are equal so that

$$\frac{\hat{h}_1}{h_1} = \frac{\hat{h}_3}{h_3} \quad (4.18)$$

then substitution into Equation 4.17 results in

$$\frac{\hat{h}_1}{h_1} = \frac{\hat{h}_3}{h_3} = (1 - \phi)^{\frac{1}{2}} \quad (4.19)$$

In the final model, substituting $h_1 = h_3 = \Phi h_2$ and Equation 4.13 into the previous result yields the equation for the particle's half-lengths of the principal axes

$$\hat{h}_1 = \hat{h}_3 = (1 - \phi)^{\frac{1}{2}} \frac{t}{4} \left(\frac{6}{\pi} \right)^{\frac{1}{3}} \Phi \quad (4.20)$$

In the current model for Kevlar Style 706 fabric, specifying $t = 0.023 \text{ cm}$, $\phi = 0.5$, and calculating $\Phi = 1.887$ results in $h_2 = 0.00713 \text{ cm}$ and $\hat{h}_1 = \hat{h}_3 = 0.00952 \text{ cm}$.

4.3 Particle Kinematics

The modeled physical system is an embodiment of n deforming ellipsoidal particles ($i = 1, 2, 3, \dots, n$), each with mass $m^{(i)}$ and separation distances of the major semi-axes $h_1^{(i)}$, $h_2^{(i)}$, $h_3^{(i)}$. The ellipsoidal particles allow the high aspect ratio of the yarn cross section to be represented more easily than with traditional spheres. The particles translate and rotate so that the position vector for the particle center of mass ($\mathbf{c}^{(i)}$) and the Euler parameter vector ($\mathbf{e}^{(i)}$) describe the particle's position and orientation.

$$\mathbf{c}^{(i)} = \begin{bmatrix} c_1^{(i)} \\ c_2^{(i)} \\ c_3^{(i)} \end{bmatrix}, \quad \mathbf{e}^{(i)} = \begin{bmatrix} e_0^{(i)} \\ e_1^{(i)} \\ e_2^{(i)} \\ e_3^{(i)} \end{bmatrix} \quad (4.21)$$

The Euler parameters are defined as a set of four quantities e_0 ; e_1 ; e_2 ; e_3 described as follows:

$$e_0 = \cos\left(\frac{\phi}{2}\right) \quad (4.22)$$

$$e_i = \cos(\theta_i) \sin\left(\frac{\phi}{2}\right), \quad i = 1, 2, 3 \quad (4.23)$$

where $\cos(\theta_i)$ are the direction cosines of the axis, and ϕ is the rotation about the axis. The four parameters describe a finite rotation about an arbitrary axis. Since any non-redundant representation of rotation must have only three independent parameters, the Euler parameters must satisfy the following constraint [98]

$$e_0^2 + e_1^2 + e_2^2 + e_3^2 = 1 \quad (4.24)$$

The Euler parameter vector is computationally efficient, providing a singularity-free description of particle rotations, and defines a rotation matrix ($\mathbf{R}^{(i)}$) for each particle which transforms global components of vector \mathbf{v} into components $\hat{\mathbf{v}}$ in the local frame of particle i [78].

4.4 Potential Energy

Previous research from Fahrenthold and Park has well documented the Lagrange's equations used in the hybrid particle element method [36, 78, 79]. In the current model, the system potential energy consists of contributions from the particles and elements and has the general form

$$V = \sum_{i=1}^n U^{(i)} + \sum_{i=1}^n \sum_{j=1}^n \alpha_{ij} V_o^{(i,j)} \psi^{(i,j)} + \sum_{i=1}^n \sum_{j=1}^n \alpha_{ij} V_o^{(i,j)} \phi^{(i,j)} \quad (4.25)$$

The first term is a thermo-mechanical potential for particle interactions where $U^{(i)}$ is the total internal energy of the i th particle, and the pressure ($P^{(i)}$) and temperature ($\theta^{(i)}$) are defined by the functional form

$$P^{(i)} = P^{(i)}(u^{(i)}, \rho^{(i)}), \quad \theta^{(i)} = \theta^{(i)}(u^{(i)}, \rho^{(i)}) \quad (4.26)$$

where $u^{(i)}$ and $\rho^{(i)}$ are the internal energy per unit mass and the density [78].

The second term accounts for strain energy per unit volume in tension and depends on the number of particles (n) and the number of neighboring particles identified by a $n \times n$ Boolean matrix (α_{ij}). The strain energy due to tension ($\psi^{(i,j)}$) is

$$\psi^{(i,j)} = \frac{1}{2} E^{(i,j)} (1 - d^{(i,j)}) \langle \epsilon^{(i,j)} \rangle^2 \quad (4.27)$$

and

$$V_o^{(i,j)} = \frac{1}{2} (V_0^{(i)} + V_0^{(j)}) \quad (4.28)$$

$$E^{(i,j)} = \frac{1}{2} (E^{(i)} + E^{(j)}) \quad (4.29)$$

$$\epsilon^{(i,j)} = \left(\frac{|\mathbf{c}^{(i)} - \mathbf{c}^{(j)}|}{|\mathbf{c}_0^{(i)} - \mathbf{c}_0^{(j)}|} - 1 \right) \quad (4.30)$$

$$d^{(i,j)} = \frac{1}{2} (d^{(i)} + d^{(j)}) \quad (4.31)$$

where the superscript (i, j) denotes the reference and neighboring particle, $V_o^{(i,j)}$ is the average volume, $E^{(i,j)}$ is average Young's modulus, $\epsilon^{(i,j)}$ is the strain which acts in tension only and is a function of the particle nodes, \mathbf{c} is the nodal coordinate, \mathbf{c}_0 is the reference nodal coordinate, and $d^{(i,j)}$ is the average damage variable. The damage variable ranges from a value of 0 representing no damage to 1 representing full damage. The bracket function $\langle x \rangle$ denotes

$$\langle x \rangle = x \hat{u}(x) \quad (4.32)$$

where \hat{u} is the unit step function, since the strain acts in tension only.

The third term relates strain energy due to particle rotation. It depends on the number of particles (n), the number of neighboring particles identified with the $n \times n$ Boolean matrix (α_{ij}) , the volume $(V_o^{(i,j)})$ defined above, and the strain energy due to shear $(\phi^{(i,j)})$ calculated as

$$\phi^{(i,j)} = (1 - d^{(i,j)}) \kappa \mu^{(i,j)} (\mathbf{e}^{(i)} - \mathbf{e}^{(j)})^T (\mathbf{e}^{(i)} - \mathbf{e}^{(j)}) \quad (4.33)$$

where $d^{(i,j)}$ is the average shear damage variable, $\mu^{(i,j)}$ is the average shear modulus, κ is a dimensionless penalty stiffness, and \mathbf{e} is the Euler parameter vector describing the particle's orientation.

The system potential energy takes the functional form

$$V = V(U^{(i)}, \mathbf{c}^{(i)}, \mathbf{e}^{(i)}, d^{(i)}) \quad (4.34)$$

and the potential energy identifies the generalized conservative forces

$$\frac{\partial V}{\partial U^{(i)}} = 1 \quad (4.35)$$

$$\frac{\partial V}{\partial c_\alpha^{(i)}} = f_\alpha^{(i)} = \sum_{j=1}^n \alpha_{ij} (1 - d^{(i,j)}) \frac{V_o^{(i,j)} E^{(i,j)}}{l_0^{(i,j)}} \left(\frac{l^{(i,j)}}{l_0^{(i,j)}} - 1 \right) \frac{(c_\alpha^{(i)} - c_\alpha^{(j)})}{l^{(i,j)}} \quad (4.36)$$

$$\frac{\partial V}{\partial e_\alpha^{(i)}} = \tau_\alpha^{(i)} = \sum_{j=1}^n 2\alpha_{ij} (1 - d^{(i,j)}) V_o^{(i,j)} \kappa \mu^{(i,j)} (e_\alpha^{(i)} - e_\alpha^{(j)}) \quad (4.37)$$

where the subscript (α) denotes the component of the generalized conservative force, and the particle distances l_0 and l are defined by the nodal coordinates

$$l_0^{(i,j)} = | \mathbf{c}_0^{(i)} - \mathbf{c}_0^{(j)} | \quad (4.38)$$

$$l^{(i,j)} = | \mathbf{c}^{(i)} - \mathbf{c}^{(j)} | \quad (4.39)$$

The strain energy release rate due to the damage is

$$\begin{aligned} \frac{\partial V}{\partial d^{(i)}} &= - \Gamma^{d(i)} \\ &= - \sum_{j=1}^n \alpha_{ij} V_o^{(i,j)} \left[\frac{E^{(i,j)}}{4} \left\langle \frac{l^{(i,j)}}{l_0^{(i,j)}} - 1 \right\rangle^2 + \right. \\ &\quad \left. \frac{\kappa \mu^{(i,j)}}{2} (\mathbf{e}^{(i)} - \mathbf{e}^{(j)})^T (\mathbf{e}^{(i)} - \mathbf{e}^{(j)}) \right] \end{aligned} \quad (4.40)$$

4.5 Failure Criteria

The network of woven particles used to represent the Kevlar yarn failed when the averaged strain in tension between any adjoining particles exceeded the failure strain. The damage variable, d , was initially set to zero, and the change in damage at particle i increases, ($\dot{d}^{(i)} > 0$), when

$$\epsilon^{(i)} > \epsilon_f \quad (4.41)$$

and

$$\epsilon^{(i)} = \frac{1}{n_n^{(i)}} \sum_{j=1}^n \alpha_{ij} \epsilon^{(i,j)} \quad (4.42)$$

where $\epsilon^{(i)}$ is the average strain at particle i , $\epsilon^{(i,j)}$ represents the strain from particle i to a connecting particle j , α_{ij} is the $n \times n$ Boolean matrix which identifies the neighboring particles (n_n), and ϵ_f is the rate dependent failure strain.

The damage evolution equations provide a means to systematically degrade material strength properties once an element meets any specified material failure criteria. Damage variables model the conversion from an undamaged to a degraded form once element failure criteria are satisfied. The damage evolution equations employed are from Silling [103], and dissipate the strain energy stored in tension and shear over \hat{n} time steps. The evolution equation for damage (d) is

$$\dot{d}^{(j)} = \frac{\Lambda^{(j)}}{\hat{n} \Delta t} \hat{u}(1 - d^{(j)}) \quad (4.43)$$

The term $\Lambda^{(j)}$ is a constant describing the rate of damage evolution. To represent no damage evolution, $\Lambda^{(j)}$ is initially set to zero, and is adjusted to a value of one when the accumulated failure strain criterion is reached. The time step is Δt . Element failure is defined as any combination of the following:

- 1) The accumulated elastic strain (ϵ) reaches the failure strain (ϵ_f)

2) The temperature ($\theta^{(i)}$) reaches the melt or char temperature ($\theta_m^{(i)}$)

In functional form, the damage evolution equation is a nonholonomic constraint in the form

$$\dot{d}^{(i)} = \dot{d}^{(i)} (U^{(i)}, \mathbf{c}^{(i)}, \mathbf{e}^{(i)}, d^{(i)}) \quad (4.44)$$

4.6 Irreversible Entropy Production

Energy methods can solve the thermo-mechanical problem using internal energy evolution equations. The general internal energy evolution equation for particle i is in the form [78]

$$\dot{U}^{(i)} = \dot{U}^{wrk(i)} + \dot{U}^{irr(i)} - \dot{U}^{con(i)} \quad (4.45)$$

where $\dot{U}^{wrk(i)}$ represents mechanical power flow, $\dot{U}^{irr(i)}$ accounts for irreversible entropy evolution due to energy dissipation, and $\dot{U}^{con(i)}$ represents numerical heat diffusion. Consistent with most impact codes, a heat conduction model allows the heat generated due to viscous effects to diffuse through the material [74]. Park and Fahrenthold developed the equations for mechanical power flow and numerical heat diffusion in their work [78].

$$\dot{U}^{wrk(i)} = m^{(i)} \frac{P^{(i)}}{\rho^{(i)2}} \dot{\rho}^{(i)} \quad (4.46)$$

$$\dot{U}^{con(i)} = \dot{Q}^{con(i)} \quad (4.47)$$

Equation 4.46 represents the internal energy evolution from the interaction between particles in contact. The thermal power flow is represented by $\dot{Q}^{con(i)}$ in Equation 4.47. The energy dissipation due to irreversible entropy production for particle i depends on the dissipation in the particles due to damage evolution

$$\dot{U}^{irr(i)} = \sum_{j=1}^n \alpha_{ij} \zeta^{(i,j)} \dot{Q}^{irr(i)} \quad (4.48)$$

where $\dot{Q}^{irr(i)}$ is the power dissipated in damage evolution in particle i given by

$$\dot{Q}^{irr(i)} = \Gamma^{d(i)} \dot{d}^{(i)} \quad (4.49)$$

and $\zeta^{(i,j)}$ is the fraction of dissipation in particle i due to particle j .

4.7 Equation of State

Implementation of the Kevlar material model required the proper use of an equation of state. The equation of state for the modeled Kevlar used a Mie-Gruneisen formulation [121, 122]

$$P = P_H \left(1 - \frac{\Gamma \mu}{2} \right) + \Gamma \rho (u - u_0) \quad (4.50)$$

where

$$P_H = K_1\mu + K_2\mu^2 + K_3\mu^3 \quad \text{for } \mu \geq 0 \quad (4.51)$$

$$P_H = K_1\mu \quad \text{for } \mu < 0 \quad (4.52)$$

and

$$\mu = \frac{\rho}{\rho_0} - 1 \quad (4.53)$$

is a measure of the material's compressibility, P is the pressure, ρ is the current density, ρ_0 is the reference or initial density, Γ is the Mie-Gruneisen parameter, u is the internal energy per unit mass, u_0 is the reference internal energy per unit mass, and K_1, K_2, K_3 are empirical constants.

With no validated Mie-Gruneisen or tabulated equation of state data for Kevlar, the equation of state for Kevlar KM-2 used a Mie-Gruneisen gamma approximated by the following [8, 36, 43]

$$\Gamma = \frac{\beta\kappa}{\rho C} \quad (4.54)$$

where β is the thermal expansion coefficient, κ is the bulk modulus, ρ is the density, and C is the specific heat. Tabulated material properties for steel and calculated material properties for Kevlar are included in Table 4.1 [28, 45, 58, 105]. The Mie-Gruneisen slope coefficient for Kevlar was estimated at 1.0, consistent with previous research [36].

4.8 Rate Dependent Strength Model

Several references are summarized in Table 4.2 which shows the quasi-static tensile strength of Kevlar KM-2 and the specimen type. In general, the individual KM-2 fibers were stronger than yarns, which in turn were stronger than fabrics. Jearanaisilawong [48] investigated all three specimen types and observed this trend, although his results were lower than other researchers listed in the table. Raftenberg [88] and Clements [22] separately noted in their work that degradation in strength is known to occur in the weaving and manufacturing process, so that these large differences between fabric, yarn, and prewoven fiber strengths are possible. Additionally, Wang and Xia describe strain rate dependence for a single Kevlar fiber for their experiments over a large strain rate range [112, 113].

In the current work, a rate dependent strength model was used for the Kevlar to capture the strain rate dependence of the Kevlar yarn. High velocity impacts involve high strain rate loading, so any material model parameter dependent on strain rate is important in order to predict system performance. Accordingly, Dooraki [28] recently discussed significant strain rate dependence on the mechanical properties of Kevlar KM-2 yarn, measuring the maximum engineering stress under uniaxial loading conditions and discovered a 7.32% increase in strength as the strain rate increased from 0.0001 to 800 s^{-1} , Table 4.3.

The failure strain evolution rate can be expressed as the following equation

$$\dot{\epsilon}_f = \left[\frac{\gamma \dot{\epsilon}}{1 + \gamma \dot{\epsilon}} \right] \langle \dot{\epsilon} \rangle \hat{u} (\epsilon_f^{max} - \epsilon_f) \quad \text{for } \dot{\epsilon} > \dot{\epsilon}_0 \quad (4.55)$$

where ϵ_f is the failure strain. From a series of dynamic uniaxial tension tests, the dynamic failure strains were obtained. The rate change in dynamic failure strain over the test data is represented by γ . A more detailed derivation of Equation 4.55 can be found in the Appendix.

The maximum failure strain cannot increase indefinitely with increasing strain rate. Hence, at very high strain rates associated with high velocity impacts, the maximum failure strain value was limited in agreement with current Kevlar KM-2 data [57].

4.9 Simulation Results

The modified material models were adapted in a series of three dimensional simulations of a .22 cal Fragment Simulating Projectile (FSP) impact on one, two, and four layers of Kevlar with various impact velocities from experiments described in reference [40]. Quantitative agreement of residual projectile velocities, over a large range of impact velocities, was obtained. All impacts were at zero degree obliquity on Kevlar targets with two fixed and two free edges. Simulation results are shown in Figures 4.5 - 4.7 by layers and summarized in Table 4.4, showing good agreement with experimental data from SwRI testing. Results are shown with the experimental data and the experimental correlation curve developed in Chapter 2. Validation of the simulation results was with the experimental correlation curve and not specific

impact velocities.

Figures 4.8 - 4.10 show the simulation results of a FSP impacting a single layer of Kevlar at 300 m/s at initial configuration, 50 and 100 μsec . Figure 4.11 is a FSP impact on one layer at 297 m/s from experiment at 0 - 100 μsec for comparison to the simulation. Figures 4.12 - 4.14 show the simulation of a FSP impact on four layers of Kevlar at 400 m/s at initial configuration, 93 and 120 μsec . Figure 4.15 is a FSP impact on four layers at 386 m/s from experiment at 0 - 120 μsec for comparison to the simulation. Unlike pure finite element methods that discard elements after failure, these simulations show that the current method preserves material fragments and models contact-impact of intact as well as fragmented material.

The results reported in the current work suggest that the hybrid particle-element method used in the simulations is numerically robust and includes important basic geometry of multilayer Kevlar impact experiments. The hybrid particle-bar element approach developed in this work models the intra-layer and inter-layer contact-impact dynamics of Kevlar yarn, as well as yarn crimp. Presenting a rate dependent strength model for the Kevlar yarn appears to accurately predict the damage and impact performance of FSP impacts on Kevlar fabrics. A total of 19 simulations were completed and required between 223,000 and 668,000 particles depending on the number of target layers. Simulations required between 30 and 118 wall clock hours to complete, using parallel execution of eight Intel 64 bit, 2.66 GHz processors. The current work accurately predicted the Kevlar response under the given load conditions and

within a reasonable time with current computational resources. These simulations show that this model can serve as a supplement to experimental work in the analysis and design process for flexible armor.

4.10 Summary

The present work has described an extension of a hybrid particle-element method by developing a new mesoscale model of the Kevlar and a new rate dependent material model for the Kevlar. An advancement of previous work includes using particle and bar elements rather than hex elements to model the Kevlar yarn, capturing the yarn structure. Additionally, improvements include the formulation of strain rate dependent strength. Particles modeled as ellipsoids rather than spheres allowed modeling of Kevlar yarns with high aspect ratios. Crimp effects at the yarn level have also been incorporated. The model was validated in three dimensional impact simulations of known experimental data. The new model predicted well the impact protection provided by different layers of Kevlar Style 706 fabric against a fragment simulating projectile over a range of velocities. Such results can be used in computer aided design of advanced impact protection systems.

Suggestions for future work include: 1) additional material testing, especially at high strain rates encountered in this engineering application, to improve strength models for future simulation results, 2) additional experiments and numerical simulations with different projectile and target geometries to further validate the model, 3) additional higher resolution simulations to ex-

amine assumptions made in material modeling and the structural geometry, and 4) additional equation of state research is necessary to provide tabulated data of Kevlar materials over a range of impact velocities.

Table 4.1: Material properties used in the FSP impact simulations [28, 36, 45, 58, 105]

Property	Kevlar KM-2		Steel	
		Ref		Ref
Shear modulus (<i>Mbar</i>)	0.2574	cc	0.801	[105]
Reference density (<i>g/cm³</i>)	1.45	[45]	7.842	[105]
Reference Sound Speed (<i>cm/μsec</i>)	0.5352	[36], p.229	0.4529	[105]
Reference Yield Stress (<i>Mbar</i>)	0.0288	[28], p.1185	0.012	[105]
Melt/char temperature (<i>degrees K</i>)	700	[36], p.229	2310	[105]
Specific heat (<i>Mbar · cm³ per g · kilodegrees K</i>)	0.0142	[36], p.229	0.00448	[105]
Thermal expansion coefficient (<i>per kilodegrees K</i>)	0.038	[58], p.160	0.012	[105]
Mie-Gruneisen gamma	0.7666	[36], p.229	1.84	[105]
Mie-Gruneisen slope coefficient	1.0	[36], p.229	1.5	[105]
Failure strain rate change (<i>per μsec</i>)	1.0	[28], p.1185	na	
Crimp (%)	2.3	*	na	

na = not applicable

cc = calculated from isotropic elastic materials

* = provided by the Hexcel Corporation

Table 4.2: Kevlar KM-2 tensile strength data

Tensile Strength (<i>GPa</i>)	Specimen type	Reference
3.88	fiber	[20], p.6220
3.41	fiber	[57], p.798
3.28	fiber	[22], p.208
3.07	fiber	[48], p.36
3.30	yarn	[116], p.219
2.87	yarn	[28], p.1185
2.66	yarn	[69], p.14
2.64	yarn	[48], p.36
2.45	fabric	[69], p.15
2.39	fabric	[45]
2.14	fabric	[48], p.36

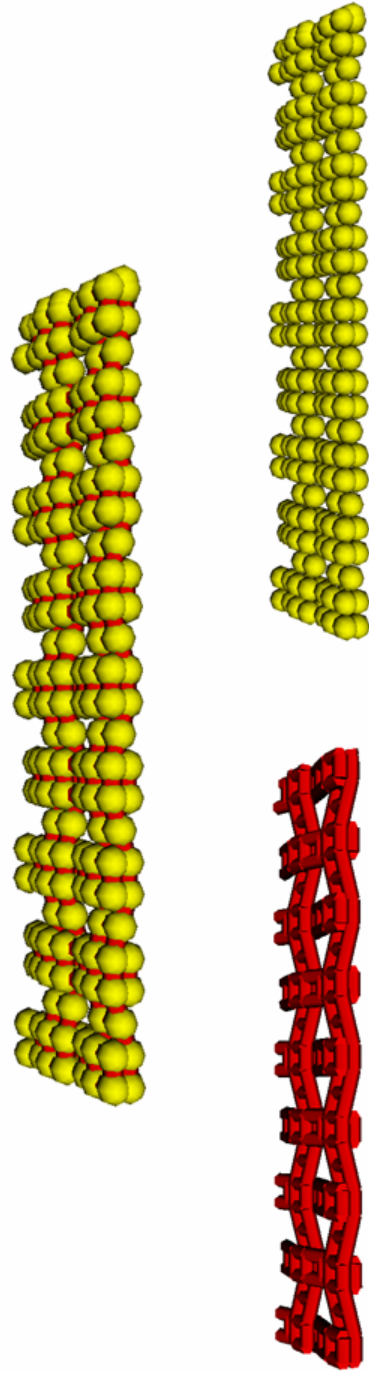
Table 4.3: Mechanical properties of Kevlar KM-2 yarn as a function of strain rate [28]

	Strain Rate	
	0.0001 s^{-1}	800 s^{-1}
σ_{max} (<i>GPa</i>)	2.87	3.08

Table 4.4: Simulation results: FSP impacts on two fixed and two free edges of neat Kevlar

Number of Layers	V_i (m/s)	V_r Experimental Correlation (m/s)	V_r Simulation (m/s)
1	100	0	0
1	150	52	52
1	200	130	102
1	250	196	174
1	300	255	258
1	350	309	306
1	400	362	351
2	200	25	0
2	250	129	48
2	300	213	203
2	350	282	261
2	400	343	306
2	450	399	398
4	300	0	0
4	350	148	51
4	400	279	193
4	450	364	311
4	500	429	444
4	550	486	518

Particles and elements are used in tandem. In ‘intact’ materials, the particle motions are coupled by bar elements.



Elements model tension

Particles model inertia,
contact-impact, and compressed states

Figure 4.1: Hybrid Particle-Element Method

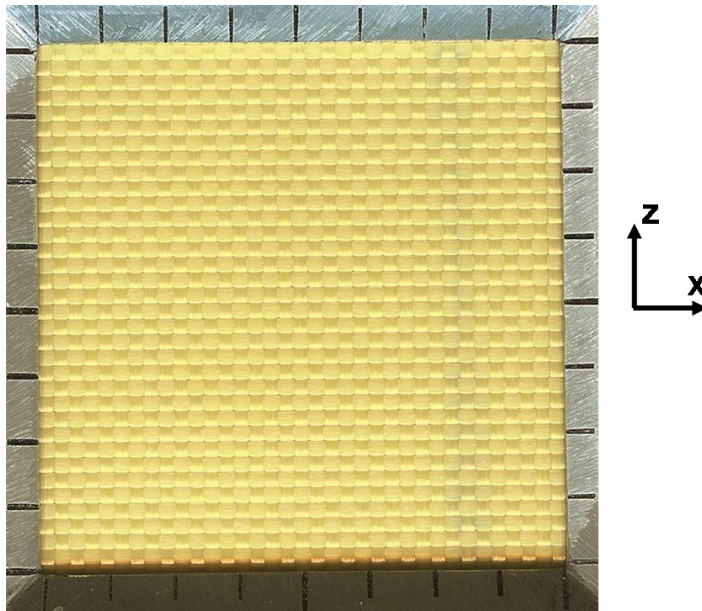


Figure 4.2: Hexcel Schwebel Style 706 fabric, Kevlar KM-2 fiber, 600 denier, 400 fibers per yarn, 34 yarns per inch



Figure 4.3: Crimp in Kevlar KM-2 yarn after removal from the woven fabric

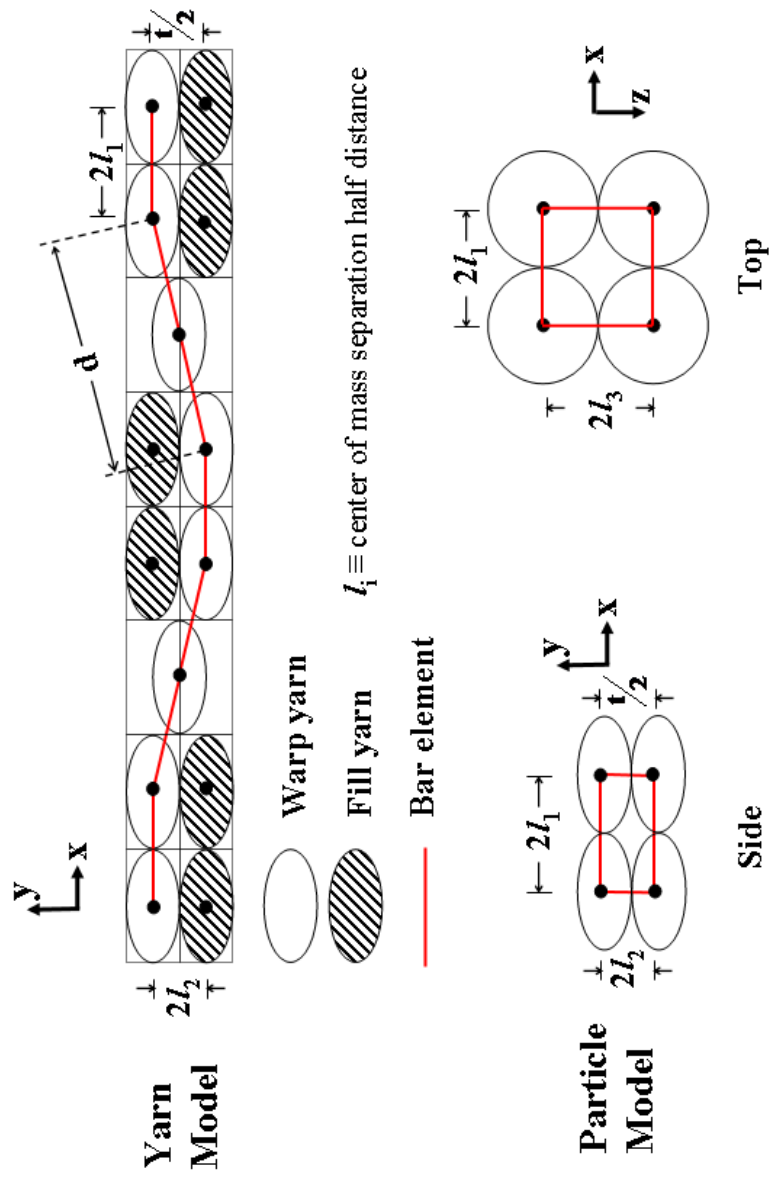


Figure 4.4: Kevlar KM-2 yarn model

One layer FSP data (2 fixed, 2 free edges)

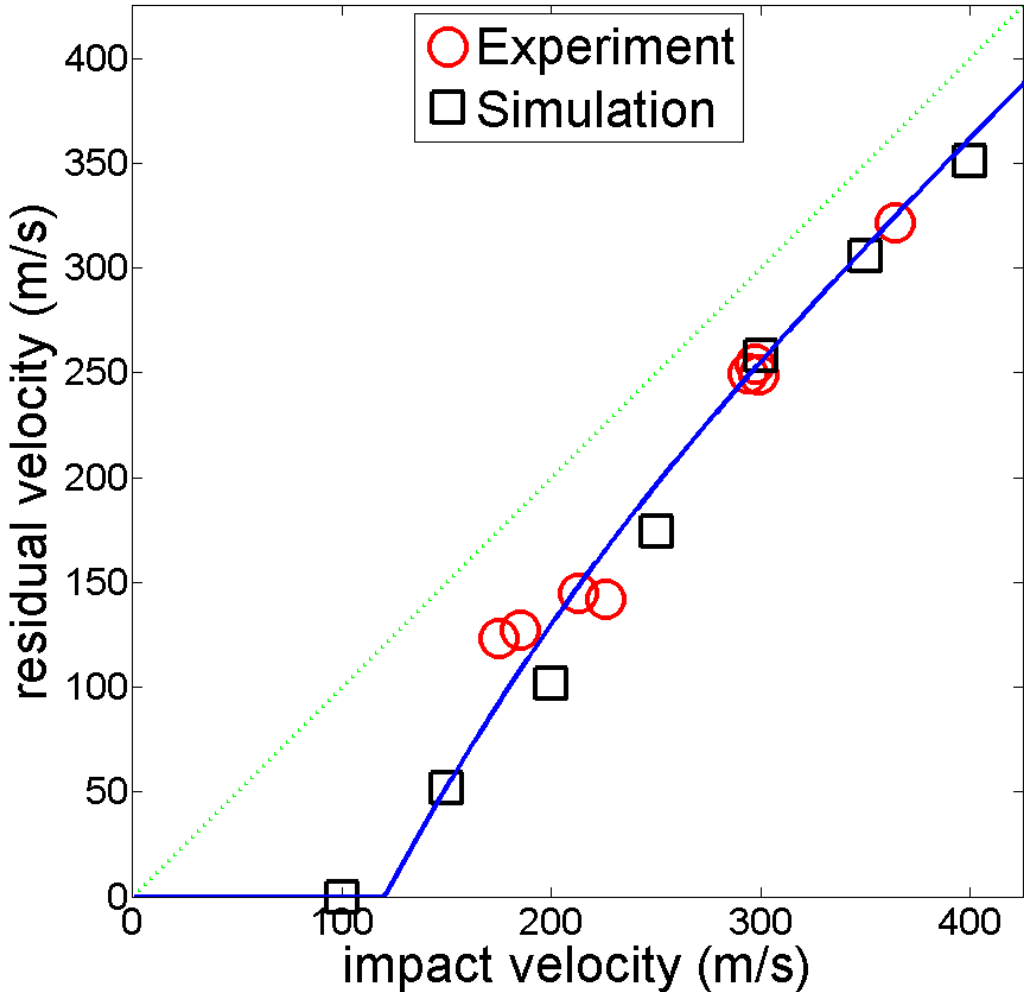


Figure 4.5: Simulation results: FSP impacts on one layer of two fixed and two free edges of neat Kevlar

Two layer FSP data (2 fixed, 2 free edges)

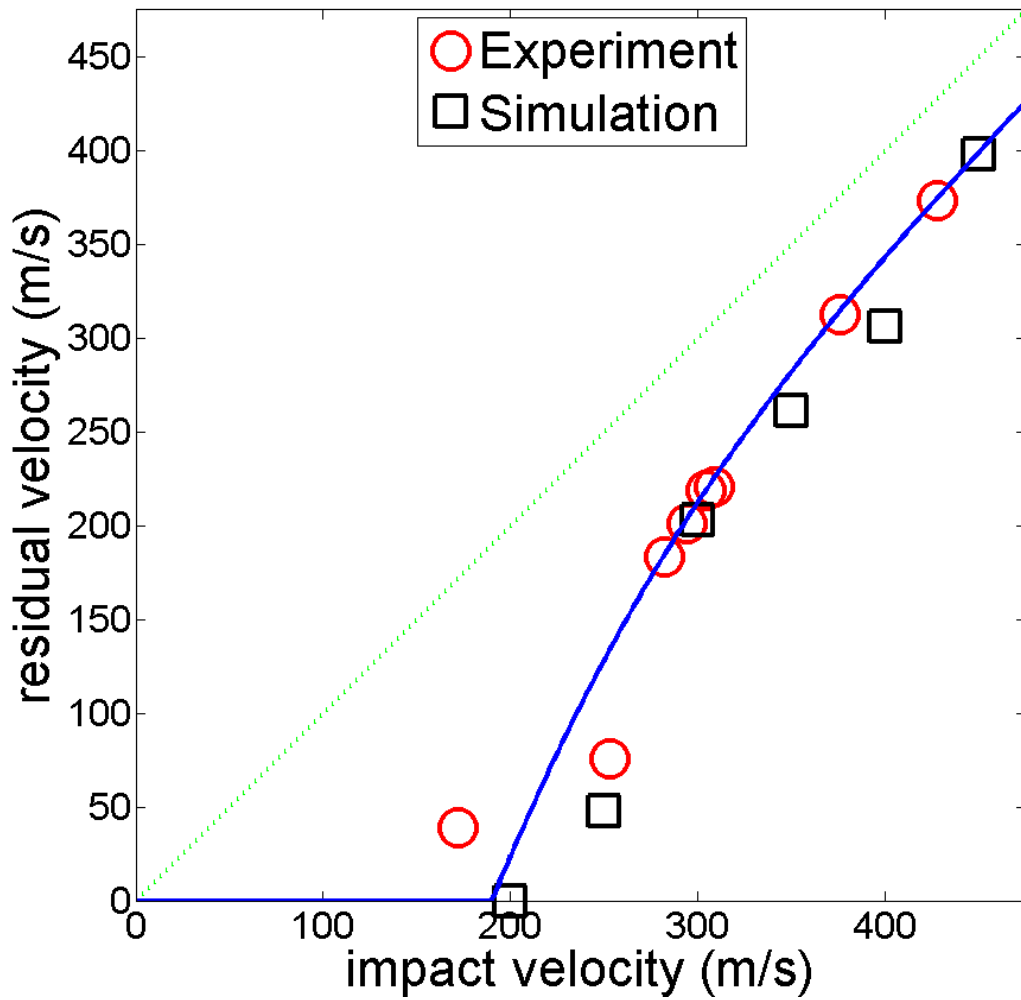


Figure 4.6: Simulation results: FSP impacts on two layers of two fixed and two free edges of neat Kevlar

Four layer FSP data (2 fixed, 2 free edges)

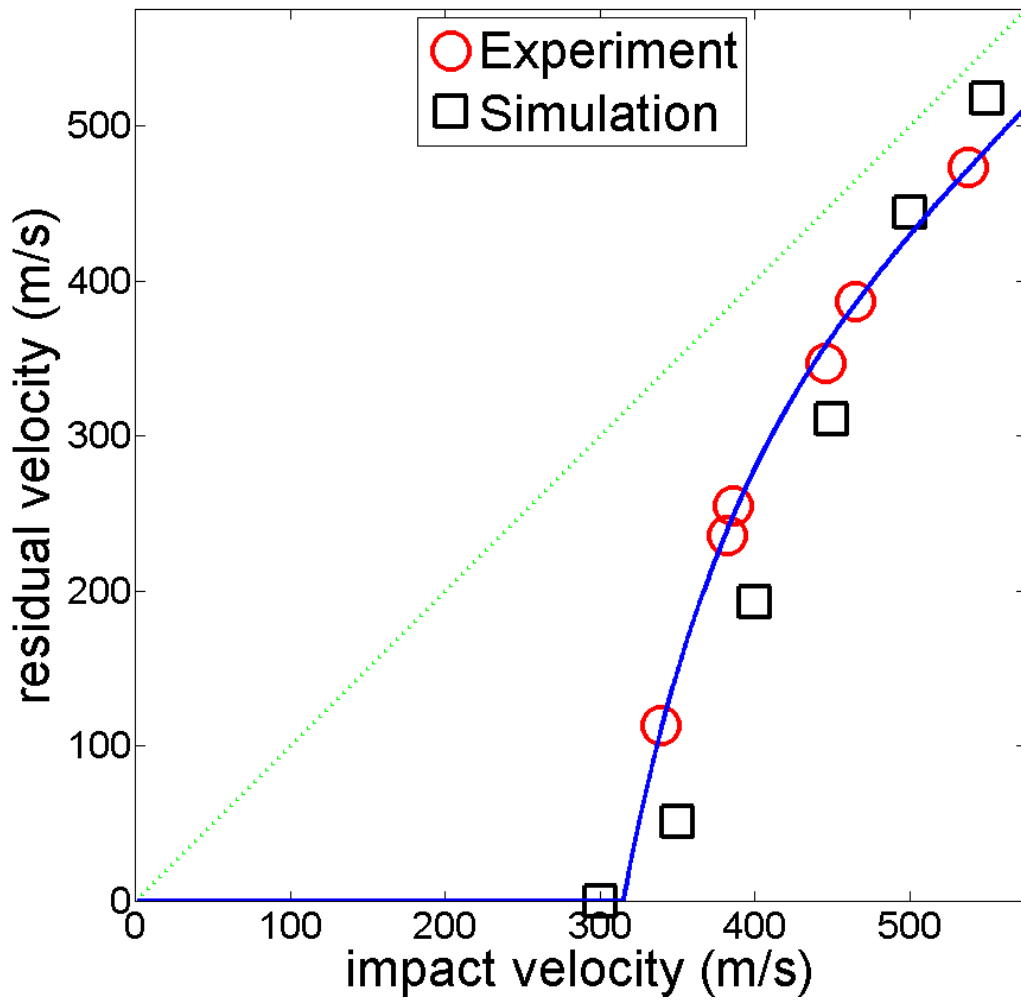


Figure 4.7: Simulation results: FSP impacts on four layers of two fixed and two free edges of neat Kevlar

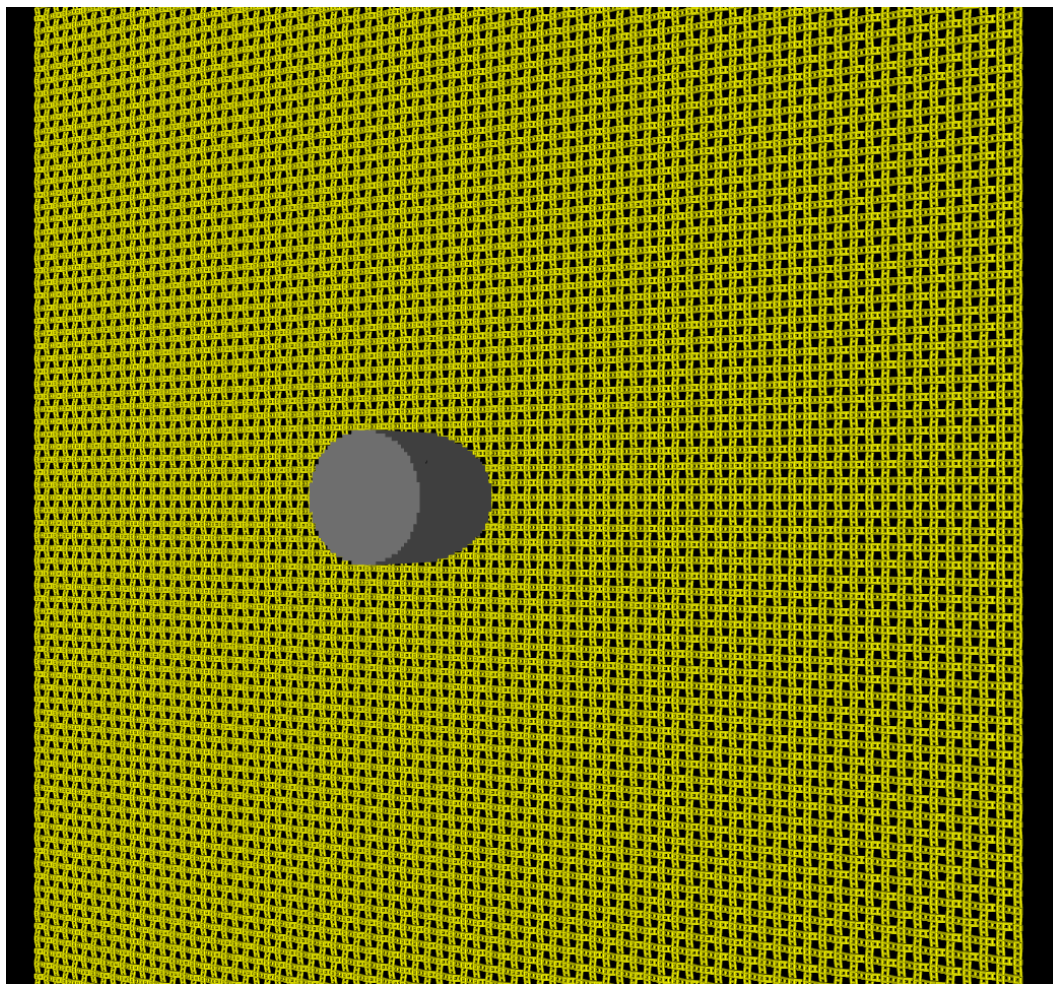


Figure 4.8: FSP impact simulation at 300 m/s on one layer of Kevlar with two fixed and two free edges at 0 μsec

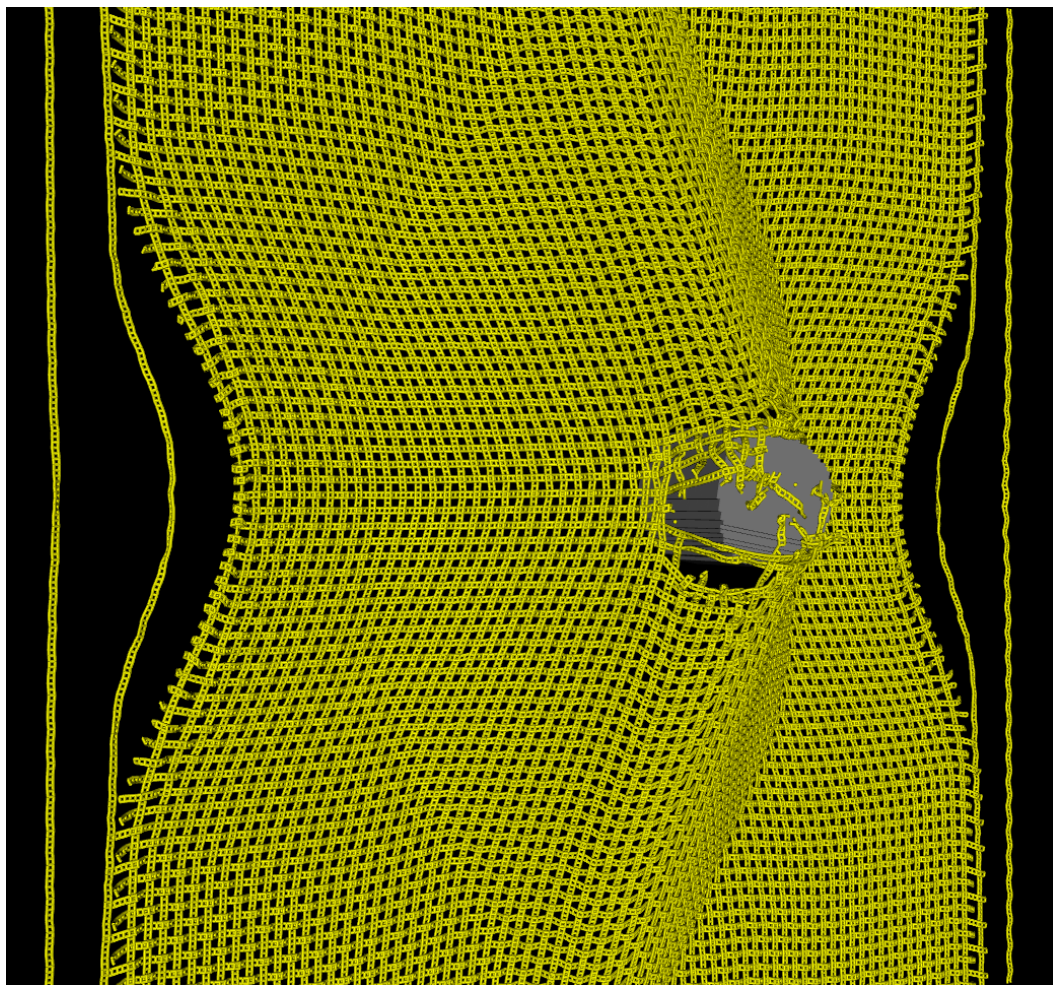


Figure 4.9: FSP impact simulation at 300 m/s on one layer of Kevlar with two fixed and two free edges at $50\text{ }\mu\text{sec}$ after impact

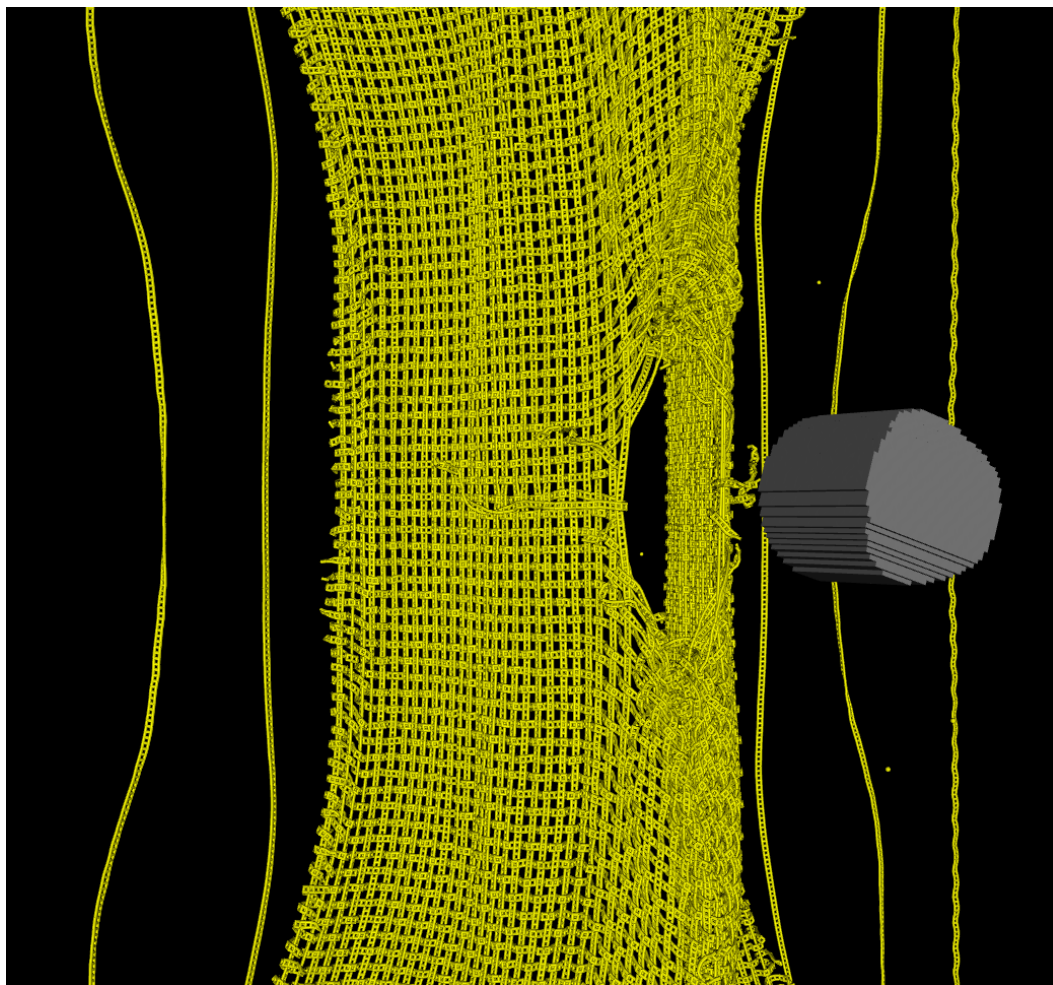


Figure 4.10: FSP impact simulation at 300 m/s on one layer of Kevlar with two fixed and two free edges at $100\ \mu\text{sec}$ after impact

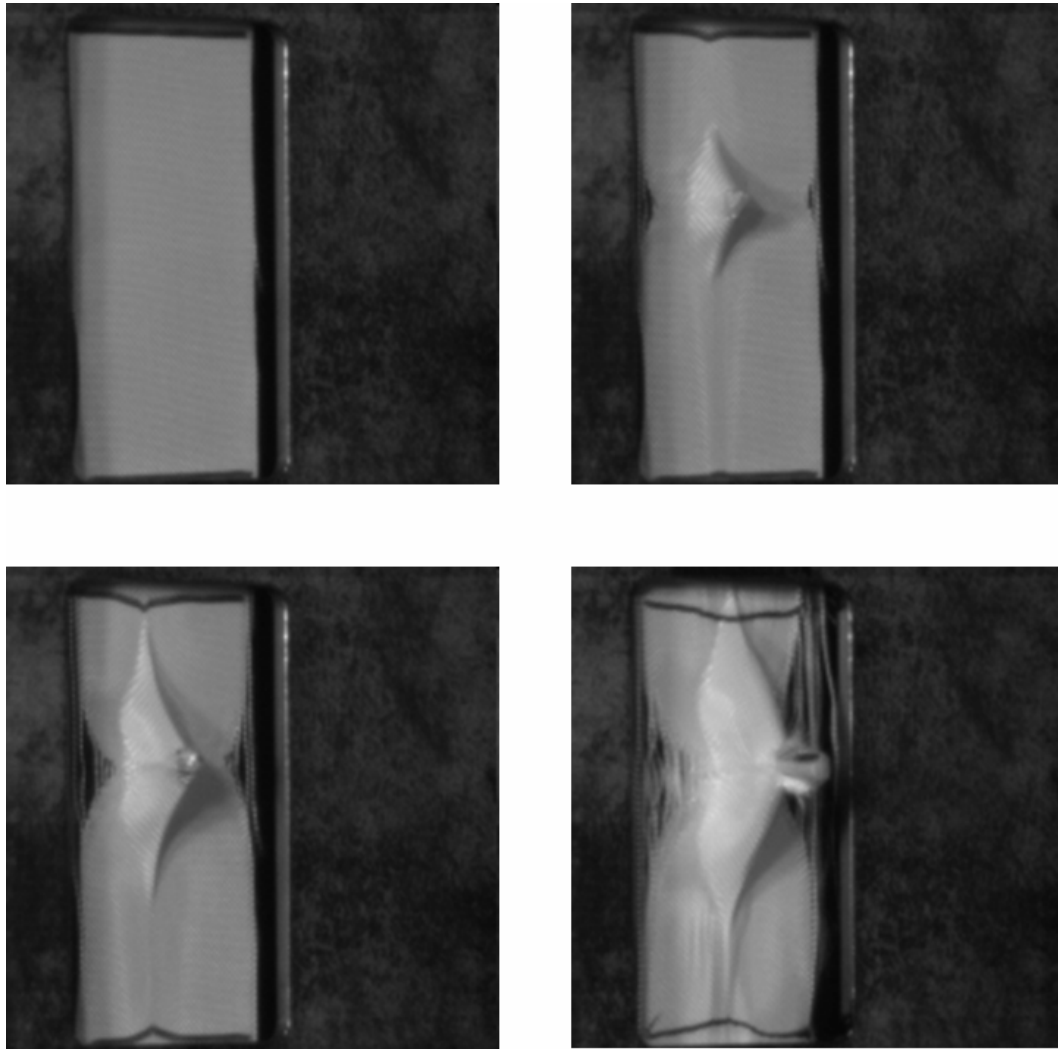


Figure 4.11: FSP impact experiment at 297 m/s on one layer of Kevlar with two fixed and two free edges at $0 - 100\ \mu\text{sec}$ after impact

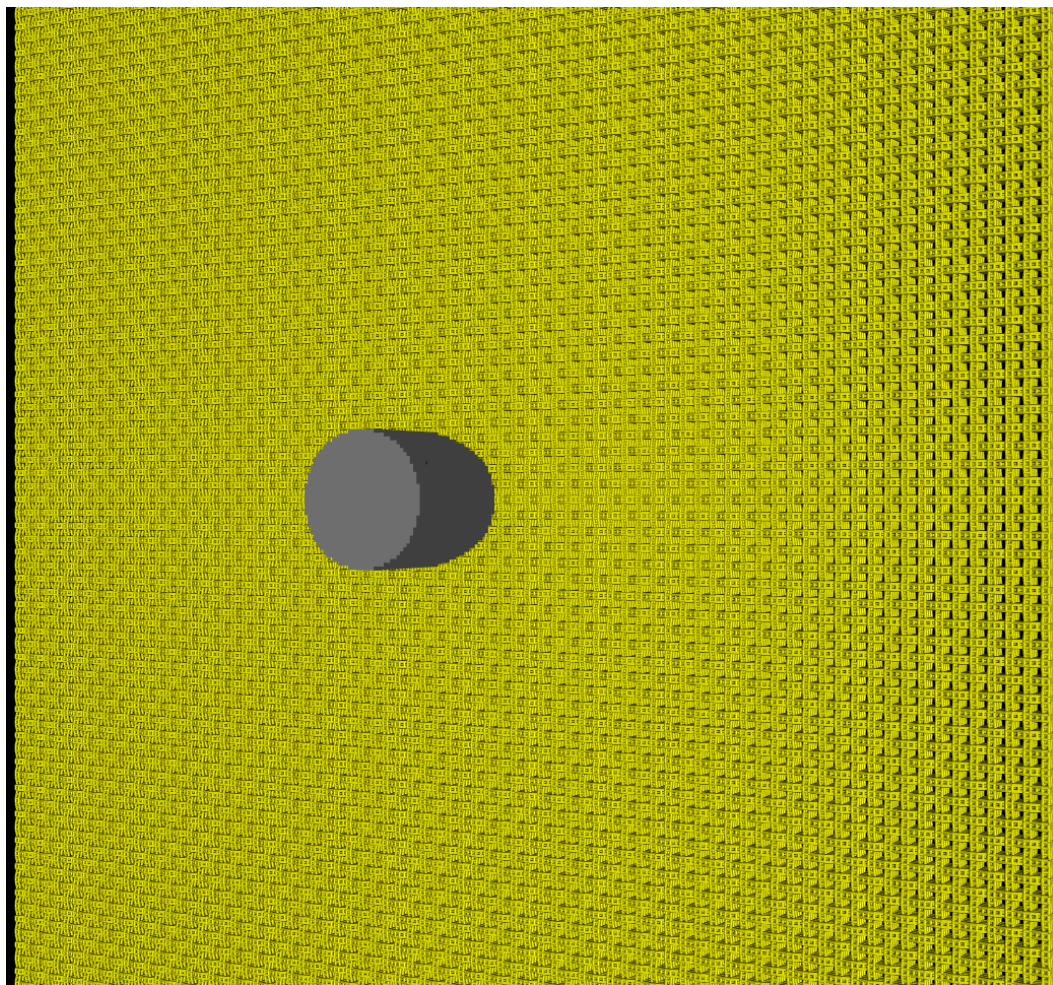


Figure 4.12: FSP impact simulation at 400 m/s on four layers of Kevlar with two fixed and two free edges at $0\ \mu\text{sec}$

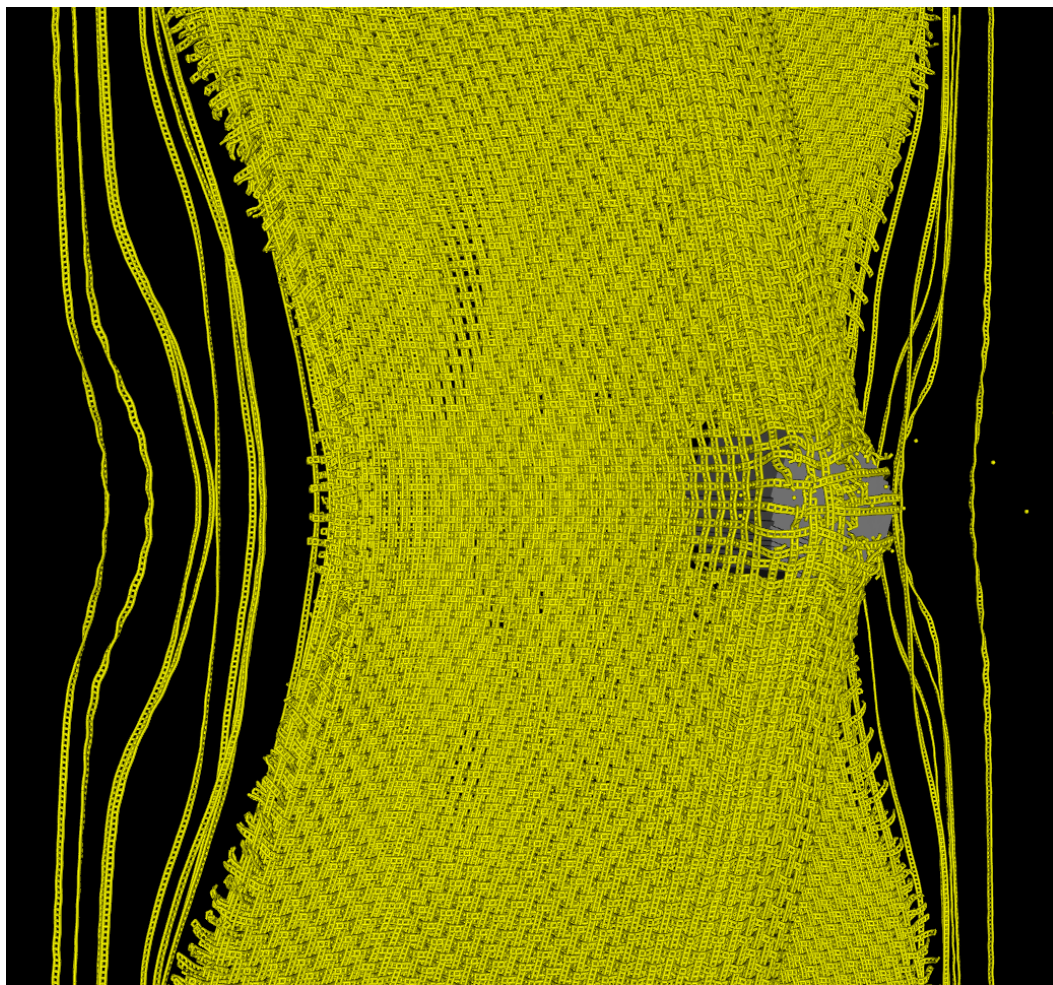


Figure 4.13: FSP impact simulation at 400 m/s on four layers of Kevlar with two fixed and two free edges at $93\ \mu\text{sec}$ after impact

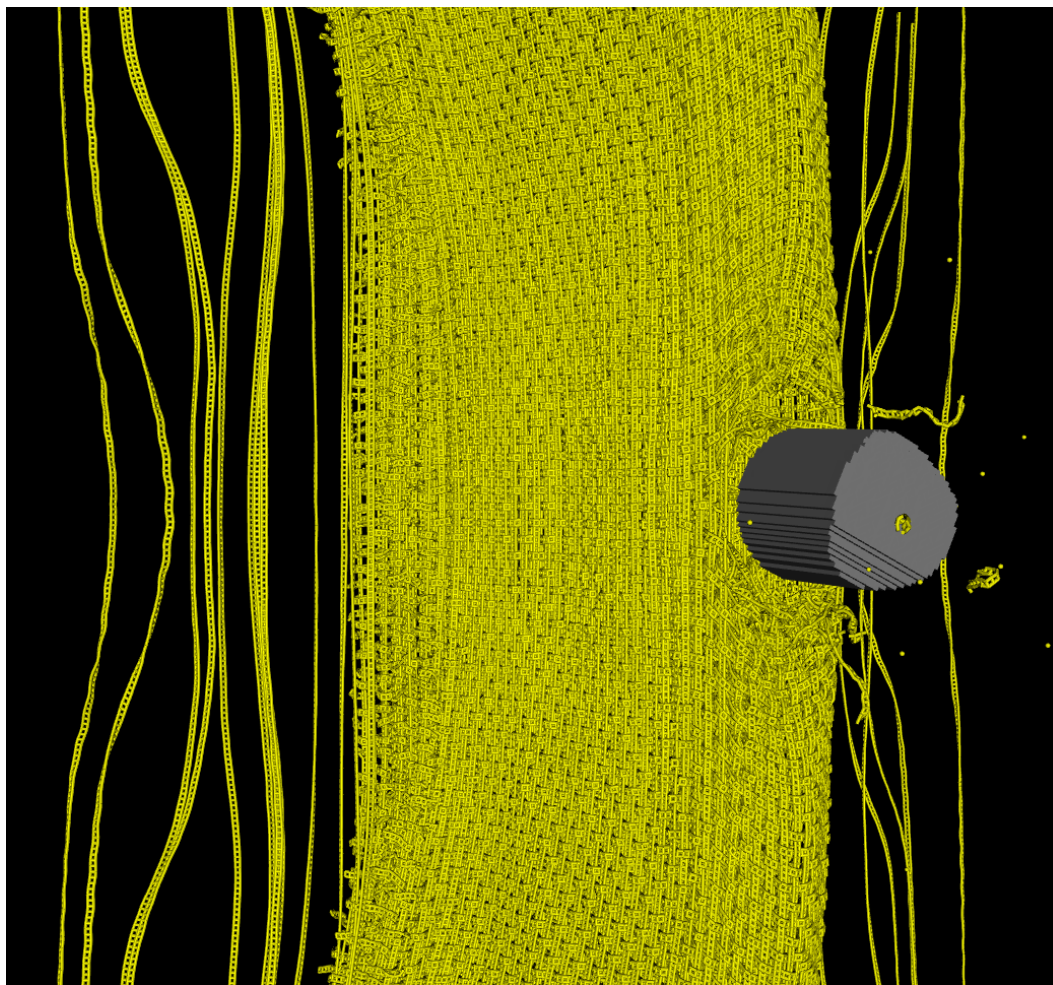


Figure 4.14: FSP impact simulation at 400 m/s on four layers of Kevlar with two fixed and two free edges at $120\ \mu\text{sec}$ after impact

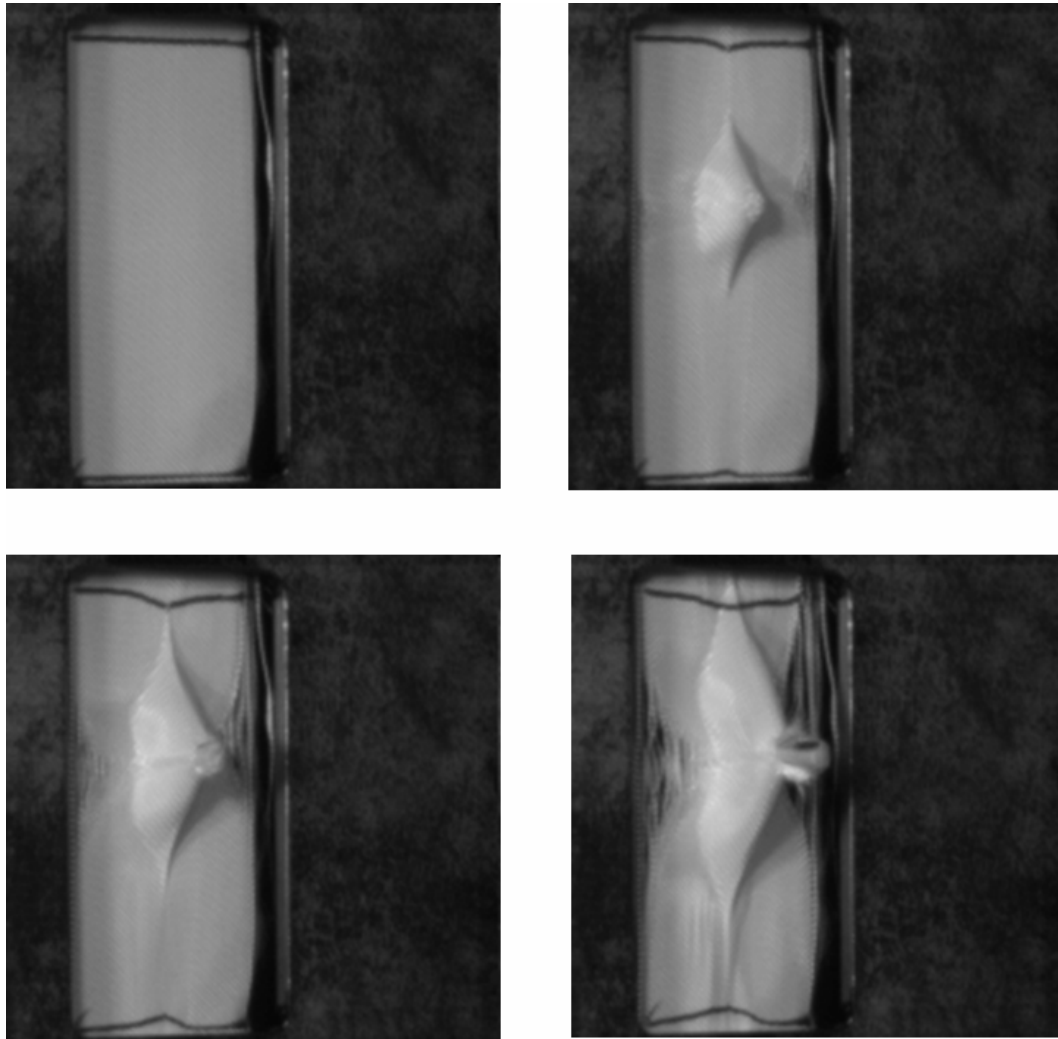


Figure 4.15: FSP impact experiment at 386 m/s on four layers of Kevlar with two fixed and two free edges at $0 - 120\ \mu\text{sec}$ after impact

Chapter 5

Development and Validation of a Particle-Element Model for Shear Thickening Fluid (STF) Treated Kevlar Fabric

5.1 Introduction

Aircraft engines can fail catastrophically in a high-energy "blade-out" event that results in large and small pieces of rotating engine components perforating the engine casings and damaging the aircraft structure and control systems. In order to reduce risks and guarantee passenger and crew safety for commercial jet aircraft, a system must exist that will prevent a loose compressor or turbine blade from penetrating the engine case while running at full thrust [17].

Title 14, Code of Federal Regulations (CFR) 25.903(d)(1), states that "Design precautions must be taken to minimize the hazards to the airplane in the event of an engine rotor failure...." Minimizing such hazards to the aircraft can be accomplished in several ways, but one is to mitigate the hazards to safe flight through aircraft design and construction [37].

The system designed to mitigate the release of uncontained fragments and prevent the debris from penetrating the engine is known as the fan contain-

ment system. Containment systems result in safer operations by protecting the aircraft from damage arising from high-energy trajectories of turbine blade failure. There are generally two types of fan containment systems: hardwall and softwall systems. Hardwall systems consist of a stiff section of the engine housing that prevents penetration if impacted by a blade. Softwall systems contain a relatively thin ring of metal surrounded by dry fabric [17].

Traditional hardwall containment systems use lightweight metals, such as aluminum and titanium, to provide for the safety of the critical airplane components in a "blade-out" event. Metallic containment systems make the airplane heavier and are costly to manufacture. One suitable alternative to the all metal or hard-wall containment case is the softwall system consisting of an aluminum containment system protected by a composite textile, which is a lighter and stronger barrier. Such systems have been shown to be especially effective for diminishing engine debris damage during a fan blade-out event. One commonly used fabric is Kevlar enclosing the appropriate area of the fan housing [94].

High strength, high modulus aramid fibers such as Kevlar have found application in advanced impact protection where their relatively low densities ($\sim 1.5 \text{ gm/cm}^3$) make them very attractive for aircraft engine containment systems where there are significant penalties for weight [102]. Various system and design requirements for a particular aircraft may determine the appropriate use of a hardwall or softwall system. However, the softwall system generally shows the lightest weight with typically 24 - 35% weight savings over hardwall

systems with similar protection [35].

Shockey and colleagues [99] have recently concluded that high-strength polymer fabrics offer an extremely effective, low-weight solution for mitigating the effects of uncontained turbine engine fragments on commercial aircraft. Their ability to deform during impact spreads the load over a larger area. When the fabric deforms and shrouds the fragment, the fabric layers are carried along the path of the projectile, adding mass and drag.

Recent development offers a new material choice for impact protection with shear thickening fluid (STF) [59, 65] treated Kevlar used as the fabric in softwall containment systems. Recent research has shown that STF treated Kevlar can absorb more energy and provide a weight savings over neat Kevlar [59, 61, 114]. When saturated into the woven fabric, the STF remains flexible. However, upon a fragment impact there may be a localized transformation of the Kevlar to a near-rigid state, allowing various mechanisms to absorb projectile energy. Experimental work with STF has explained its increase in impact performance through increased friction between the yarns [32, 107, 114].

The remainder of this chapter extends a particle-element method used in previous research by Park and Fahrenthold [78] and further extends a new Kevlar model developed in the previous chapter. Improvements include the numerical development of a velocity dependent friction model. Advancements in the material model consist of a new STF Kevlar mixture equation of state and a Bingham shear stress model to account for STF effects. The new model accounts for the added mass and thermodynamics of the STF constituents

unlike previous STF modeling attempts. Earlier STF simulation work by Cromwell in LS-DYNA3D simply adjusted the locking angle between yarns to model STF effects [24]. This chapter also presents a seventh order polynomial for the Mie-Gruneisen equation of state of certain materials, the simulation results and analysis, a comparison of computer resource requirements for this level of simulations, and recommendations for future work. The simulations described in this chapter model the experiments performed by Southwest Research Institute [38, 41], in which aluminum cylinder and steel disk projectiles impacted neat and STF Kevlar targets described in Chapter 3.

5.2 Mixture Equation of State

STF Kevlar is a composite of Kevlar, silica, and polyethylene glycol (PEG 200) which requires a new, but similar equation of state to the neat Kevlar. STF preparation requires a predetermined amount of silica to be suspended in the polyethylene glycol. The mass fraction of silica can be controlled directly during the STF preparation. Likewise, the amount of STF that is applied to the Kevlar can be controlled and verified by weight before and after STF treatment. Each component of the STF Kevlar (Kevlar, silica, and polyethylene glycol) has unique, individual material properties that contribute to the STF mixture properties. The following discussion assumes the polyethylene glycol and silica are uniformly distributed throughout the Kevlar.

5.2.1 Mass Fractions of the Constituents

The mass of STF Kevlar can be described by the mass of its individual constituents, m_i

$$m_1 + m_2 + m_3 = \alpha m_1 \quad (5.1)$$

$$m_3 = \beta m_2 \quad (5.2)$$

where α is the mass ratio of the STF Kevlar to the neat Kevlar, and β is the mass ratio of the polyethylene glycol to the silica. The subscripts 1, 2, and 3 denote Kevlar, silica, and polyethylene glycol respectively. Rearranging Equation 5.1 and substituting 5.2 yields

$$\alpha = 1 + \frac{m_2}{m_1} + \frac{m_3}{m_1} = 1 + \frac{m_2}{m_1} (1 + \beta) \quad (5.3)$$

$$m_2 = m_1 \left(\frac{\alpha - 1}{\beta + 1} \right) \quad (5.4)$$

$$m_3 = m_1 \beta \left(\frac{\alpha - 1}{\beta + 1} \right) \quad (5.5)$$

The mass fraction, f_i , of an STF component is the ratio of the component's mass to the total STF mixture mass. Using the previous results, the mass fractions of the STF constituents can be described in terms of the STF constituent mass ratios, α and β

$$f_1 = \frac{m_1}{\alpha m_1} = \frac{1}{\alpha} \quad (5.6)$$

$$f_2 = \frac{m_2}{\alpha m_1} = \frac{1}{\alpha} \left(\frac{\alpha - 1}{\beta + 1} \right) \quad (5.7)$$

$$f_3 = \frac{m_3}{\alpha m_1} = \frac{\beta}{\alpha} \left(\frac{\alpha - 1}{\beta + 1} \right) \quad (5.8)$$

With the mass fractions of the STF components calculated, these results can be used in the development of internal energy equations.

5.2.2 Internal Energy Equation

The energy method (Lagrange's equations) applied here includes mechanical and thermal dynamics, and so the internal energy is the conserved potential. For the STF mixture, the expression for the total internal energy is

$$U = m_1 u_1(\rho_1, s_1) + m_2 u_2(\rho_2, s_2) + m_3 u_3(\rho_3, s_3) \quad (5.9)$$

where the subscript denotes the STF mixture component, m is the mass, u is the internal energy per unit mass, ρ is the density, and s is the entropy per unit mass.

Generalized forces for the system can be calculated as

$$\frac{\partial U}{\partial \rho} = m \frac{P}{\rho^2} \quad (5.10)$$

$$\frac{\partial U}{\partial S} = \theta \quad (5.11)$$

For the first force listed above, Equation 5.10 can be represented with the constituents by

$$\frac{\partial U}{\partial \rho} = m_1 \frac{\partial u_1}{\partial \rho_1} \frac{\partial \rho_1}{\partial \rho} + m_2 \frac{\partial u_2}{\partial \rho_2} \frac{\partial \rho_2}{\partial \rho} + m_3 \frac{\partial u_3}{\partial \rho_3} \frac{\partial \rho_3}{\partial \rho} \quad (5.12)$$

For the system, assume the following thermodynamic equilibrium relationships correlate component properties

$$\frac{s - s_0}{c_v} = \frac{s_1 - s_{10}}{c_{v_1}} = \frac{s_2 - s_{20}}{c_{v_2}} = \frac{s_3 - s_{30}}{c_{v_3}} \quad (5.13)$$

$$\frac{\rho}{\rho_0} = \frac{\rho_1}{\rho_{10}} = \frac{\rho_2}{\rho_{20}} = \frac{\rho_3}{\rho_{30}} \quad (5.14)$$

$$c_v = f_1 c_{v_1} + f_2 c_{v_2} + f_3 c_{v_3} \quad (5.15)$$

where c_v is the constant volume specific heat and the subscript (0) represents the reference state.

Generalized forces for the mixture constituents are defined as

$$\frac{\partial u_1}{\partial \rho_1} = \frac{P_1}{\rho_1^2}, \quad \frac{\partial u_2}{\partial \rho_2} = \frac{P_2}{\rho_2^2}, \quad \frac{\partial u_3}{\partial \rho_3} = \frac{P_3}{\rho_3^2} \quad (5.16)$$

denoting the pressure P_i and density ρ_i for each component.

Substituting Equations 5.14 and 5.16 into 5.12 results in

$$\frac{\partial U}{\partial \rho} = m \frac{P}{\rho^2} = m_1 \frac{P_1}{\rho_1^2} \frac{\rho_{10}}{\rho_0} + m_2 \frac{P_2}{\rho_2^2} \frac{\rho_{20}}{\rho_0} + m_3 \frac{P_3}{\rho_3^2} \frac{\rho_{30}}{\rho_0} \quad (5.17)$$

which simplifies to the following

$$P = \frac{m_1}{m} P_1 \frac{\rho^2}{\rho_1^2} \frac{\rho_{10}}{\rho_0} + \frac{m_2}{m} P_2 \frac{\rho^2}{\rho_2^2} \frac{\rho_{20}}{\rho_0} + \frac{m_3}{m} P_3 \frac{\rho^2}{\rho_3^2} \frac{\rho_{30}}{\rho_0} \quad (5.18)$$

Substituting Equation 5.14 into 5.18 results in the expression for the mixture pressure

$$P = f_1 P_1 \frac{\rho_0}{\rho_{10}} + f_2 P_2 \frac{\rho_0}{\rho_{20}} + f_3 P_3 \frac{\rho_0}{\rho_{30}} \quad (5.19)$$

Similarly, the second generalized force denoted by Equation 5.11 can be represented by the constituents as

$$\frac{\partial U}{\partial S} = \theta = m_1 \frac{\partial u_1}{\partial s_1} \frac{\partial s_1}{\partial S} + m_2 \frac{\partial u_2}{\partial s_2} \frac{\partial s_2}{\partial S} + m_3 \frac{\partial u_3}{\partial s_3} \frac{\partial s_3}{\partial S} \quad (5.20)$$

From Equation 5.13, constituent entropy densities s_i are

$$s_1 = \frac{c_{v1}}{c_v} \left(\frac{S}{m} - s_0 \right) + s_{10} \quad (5.21)$$

$$s_2 = \frac{c_{v2}}{c_v} \left(\frac{S}{m} - s_0 \right) + s_{20} \quad (5.22)$$

$$s_3 = \frac{c_{v3}}{c_v} \left(\frac{S}{m} - s_0 \right) + s_{30} \quad (5.23)$$

By definition

$$\frac{\partial s_1}{\partial S} = \frac{c_{v1}}{c_v} \frac{1}{m} \quad \frac{\partial s_2}{\partial S} = \frac{c_{v2}}{c_v} \frac{1}{m} \quad \frac{\partial s_3}{\partial S} = \frac{c_{v3}}{c_v} \frac{1}{m} \quad (5.24)$$

$$\frac{\partial u_1}{\partial s_1} = \theta_1 \quad \frac{\partial u_2}{\partial s_2} = \theta_2 \quad \frac{\partial u_3}{\partial s_3} = \theta_3 \quad (5.25)$$

Substituting these results into Equation 5.20 yields

$$\theta = f_1 \theta_1 \frac{c_{v1}}{c_v} + f_2 \theta_2 \frac{c_{v2}}{c_v} + f_3 \theta_3 \frac{c_{v3}}{c_v} \quad (5.26)$$

The mixture reference density (ρ_0) can be calculated as

$$\rho_0 = \frac{m}{V_0} = \frac{m_1 + m_2 + m_3}{V_{10} + V_{20} + V_{30}} \quad (5.27)$$

which leads to a simplified form of

$$\rho_0 = \left(\frac{f_1}{\rho_{10}} + \frac{f_2}{\rho_{20}} + \frac{f_3}{\rho_{30}} \right)^{-1} \quad (5.28)$$

It follows that the STF mixture pressure P and temperature θ can be expressed by an equation of state with functional form [103]

$$P = P(\rho, S) \quad \theta = \theta(\rho, S) \quad (5.29)$$

5.3 Velocity Dependent Friction Model

The engineering application in this research involves very high relative velocity between Kevlar yarns. Early research of Kevlar friction investigated

the experimental friction coefficient of Kevlar and the effects of surface treatments [90]. Briscoe and Motamedi asserted that moderate changes in friction may have a subtle effect on ballistic performance, with the highest yarn friction resulting in higher energy dissipation [16]. Rebouillat also noted that Kevlar exhibited variation of the friction coefficient over a range of velocity [91]. Martinez and others have reported similar findings of velocity dependent friction in Kevlar [67]. However, these investigations were with much lower relative velocities than those experienced in ballistic impacts. Additionally, the narrow range of velocities from their tests showed much variation in results. Some have shown higher static than kinetic friction coefficients, while others have reported the opposite [67].

However, the mechanisms through which friction takes effect are not well understood. Many researchers have asserted that Kevlar exhibits Coulomb friction behavior and modeled Coulomb friction in Kevlar fabric [29, 30, 51, 67, 70, 118]. Some have modeled an exponential friction force to avoid the discontinuity associated with a simple Coulomb model [9, 32]. However, these exponential models are not validated, and the researchers estimated the exponential coefficients. More recently, yarn pullout tests conducted by the Army Research Laboratory show that the transition from static friction to stable kinetic friction is very acute, signifying that the friction between Kevlar yarns exhibits constant kinetic friction behavior once there is small relative velocity between the two surfaces in contact [32, 54]. However, there is no known validated velocity dependent friction model applied to Kevlar.

In the analysis of fabric, there is interest in modeling Coulomb friction and Bingham fluid type friction, both which are discontinuous at zero velocity. A friction model is used that avoids a discontinuity at zero relative velocity, Figure 5.1. The formulation is general enough to be used with other friction laws. However, unlike conventional Coulomb or other common velocity dependent dry friction models, the current work represents the friction force well at low or zero relative velocity. The friction modeled resists the relative motion between particles but cannot change the direction of the particles in one time step since the velocity dependence ensures the frictional force is zero when there is no relative motion. Similarly, the model ensures the maximum friction force between particles cannot be exceeded. From Figure 5.1 the Kevlar rate dependent friction employs a critical velocity (v_c) function, above which the frictional force is constant and in the general form

$$f_0 = \tau_0 A \quad (5.30)$$

where τ_0 is the shear force, and A is the area in contact described by

$$A = \frac{\pi h^2}{\frac{N}{2}} \quad (5.31)$$

and h is the particle radius and N is the maximum number of neighbor particles in contact. The frictional force above the critical velocity is also equal to

$$f_0 = \dot{p} = m \frac{v_c}{\Delta t}, \quad v > v_c \quad (5.32)$$

where m is the mass, v_c is the critical velocity, and Δt is the time step.

Below the critical velocity, the friction force is assumed linear from zero to the critical velocity

$$f = v \frac{m}{\Delta t}, \quad v \leq v_c \quad (5.33)$$

and the fractional part of the above equation represents the linear change in frictional force with respect to the velocity.

In the Kevlar model for the present work where particles model all inertial forces and contact-impact, the velocity dependent friction between particles i and j can be calculated from

$$\mathbf{f}^{(i)} = \sum_{j=1}^n \beta_{ij} \tau^{(i,j)} A^{(i,j)} \frac{\mathbf{v}^{t(i,j)}}{|\mathbf{v}^{t(i,j)}|} \quad \text{for } |\mathbf{v}^{t(i,j)}| > v_c \quad (5.34)$$

$$\mathbf{f}^{(i)} = \sum_{j=1}^n \beta_{ij} \min(m^{(i)}, m^{(j)}) \frac{\mathbf{v}^{t(i,j)}}{\Delta t} \quad \text{for } |\mathbf{v}^{t(i,j)}| \leq v_c \quad (5.35)$$

where β_{ij} is a Boolean matrix identifying the nearest neighbors in contact, t is time, and the minimum mass is used since motion in the particle with the smaller mass (i and j) will occur first. The average shear stress between the reference i and neighboring particle j is represented by $\tau^{(i,j)}$ and the average contact area between the particles $A^{(i,j)}$ is given by

$$\tau^{(i,j)} = \frac{1}{2} (\tau^{(i)} + \tau^{(j)}) \quad (5.36)$$

$$A^{(i,j)} = \frac{1}{2} (A^{(i)} + A^{(j)}) \quad (5.37)$$

The tangential velocity between particles i and j is

$$\mathbf{v}^{t(i,j)} = \mathbf{v}^{(i,j)} - \mathbf{v}^{n(i,j)} \quad (5.38)$$

where $\mathbf{v}^{(i,j)}$ is the relative velocity between particles and $\mathbf{v}^{n(i,j)}$ is the normal component of the velocity between the particles given by

$$\mathbf{v}^{(i,j)} = (\dot{\mathbf{c}}^{(i)} - \dot{\mathbf{c}}^{(j)}) \quad (5.39)$$

$$\mathbf{v}^{n(i,j)} = [(\dot{\mathbf{c}}^{(i)} - \dot{\mathbf{c}}^{(j)}) \cdot (\mathbf{c}^{(i)} - \mathbf{c}^{(j)})] \frac{(\mathbf{c}^{(i)} - \mathbf{c}^{(j)})}{|\mathbf{c}^{(i)} - \mathbf{c}^{(j)}|^2} \quad (5.40)$$

Again, the friction modeled here resists the relative motion between particles. However, the direction of the particles cannot change in one time step since the velocity dependence requires the frictional force to be zero when there is no relative motion.

5.4 Bingham Fluid Model

Experimental work with STF accounted for its effect as increased friction between the yarns [32, 107, 114] and viscous dissipation in the fluid [114]. In experiments, STF appeared to inhibit relative motion of yarns within the Kevlar fabric resulting in fewer yarns pulled and less distance pulled by the projectile [60, 61, 114]. During yarn pull-out tests conducted at the Army Research Laboratory (ARL), STF Kevlar samples showed nearly ten times higher

peak loads compared to neat Kevlar, followed by sudden and complete yarn failure [27, 53]. ARL suggested that STF increased the friction force between yarns, resisting their ability to slide relative to each other.

Simulations of STF effects in published literature are very limited. Early STF simulation work described by Cornwell in LS-DYNA3D simply adjusted the locking angle between yarns to model STF effects [24]. More recent work by Duan et al. used a simple viscous friction model to account for STF effects [32]. Unlike previous work using these models, this section develops a Bingham fluid model to incorporate STF effects on the modeled Kevlar particles.

STF requires high colloidal concentrations, behaving as a non-Newtonian fluid whose viscosity increases when the shear stress increases. When a projectile impacts a STF treated fabric, shear thickening can occur on a large scale such that the fluid will act more like a solid. This rigid behavior continues until the shear stress is reduced or exceeds the yield stress for the STF. This type of behavior is characteristic of a Bingham fluid which incorporates a characteristic stress or yield stress below which the material behaves as a solid [82]. Bingham fluids can transmit a shear stress without a velocity gradient; however, to make the Bingham fluid flow, the driving shear stress must be larger than the yield stress. Bingham models describe many highly viscous products such as pastes, gels, and slurries [64]. The equation describing the behavior of a fluid with a yield stress is [21]

$$\tau = \tau_0 + \eta \dot{\gamma} \quad (5.41)$$

with τ_0 defined as the yield stress which must be exceeded before the fluid will deform, η is the viscosity of the fluid, and $\dot{\gamma}$ is the shear rate. In the current work, $\eta = 0$, so the yield stress is constant and the fluid deforms once the value is surpassed.

In the Kevlar model for the present work where particles model all inertial forces and contact-impact, a nonconservative force is introduced due to the Bingham fluid behavior. This Bingham fluid model is a specific case of the velocity dependent friction model given by

$$\mathbf{f}^{(i)} = \sum_{j=1}^n \beta_{ij} \tau^{(i,j)} A^{(i,j)} \frac{\mathbf{v}^{t(i,j)}}{|\mathbf{v}^{t(i,j)}|} \quad (5.42)$$

where β_{ij} is the Boolean matrix identifying the neighboring particles. The tangential velocity $\mathbf{v}^{t(i,j)}$, the average shear stress $\tau^{(i,j)}$ and average contact area between the particles $A^{(i,j)}$ are described in the previous section.

5.5 Irreversible Entropy Production

Energy methods can solve the thermo-mechanical problem using internal energy evolution equations. The general internal energy evolution equation for particle i is in the form [78]

$$\dot{U}^{(i)} = \dot{U}^{wrk(i)} + \dot{U}^{irr(i)} - \dot{U}^{con(i)} \quad (5.43)$$

where $\dot{U}^{wrk(i)}$ represents mechanical power flow, $\dot{U}^{irr(i)}$ accounts for irreversible entropy evolution due to energy dissipation, and $\dot{U}^{con(i)}$ represents numerical heat diffusion due to the heat generated from viscous effects.

The energy dissipation due to irreversible entropy production for particle i depends on the friction and viscous forces acting on the particles

$$\dot{U}^{irr(i)} = \mathbf{f}^{(i)T} \dot{\mathbf{c}}^{(i)} \quad (5.44)$$

The viscous torque, mechanical power flow, and numerical heat diffusion are well documented in other literature by Park and Fahrenthold [78] and Shivararama and Fahrenthold [97].

5.6 Seventh Order Polynomial Mie-Gruneisen Equation of State

The Hugoniot data for many materials are determined from experiments, and some parameters such as the Hugoniot slope are commonly regarded as constant over the range of interest [122]. For some materials a higher order polynomial is used to represent the data when the material displays nonlinear behavior. Silica is one component of STF and displays unusual properties at high pressures which can be encountered during impact experiments and simulations [15]. Recently, Hare and Managan [43], investigated the Hugoniot data of silica and fit the data to a seven term polynomial Mie-Gruneisen equation of state to represent the beyond-elastic response in

hydrocode simulations.

$$P = A_0 + A_1\mu + A_2\mu^2 + A_3\mu^3 + (B_0 + B_1\mu + B_2\mu^2) \rho_0 u \quad (5.45)$$

where ρ_0 is the reference density, u is the internal energy per unit mass and

$$\mu = \frac{\rho}{\rho_0} - 1 \quad (5.46)$$

Inclusion of the seventh order polynomial equation of state for materials such as silica provides more accurate calculations for simulations. Parameters for the silica coefficients in Equation 5.45 are in Table 5.1. Alternative data for other materials may be introduced without change to the basic modeling methodology.

5.7 Simulation Results

This section describes simulations which apply the modified material model in three dimensional simulations of an aluminum cylinder and steel disk impacting various layers of neat and STF Kevlar. The simulations involve experimental data described in references [38, 41]. Material properties used in the simulations are in Table 5.2 [1, 6, 36, 43, 45, 58, 66]. The value for the PEG 200 Mie-Gruneisen gamma was calculated with Equation 4.54. Quantitative agreement of residual projectile velocities with different shape projectiles and multiple target layers was obtained. Impact velocities in simulation mirrored

those from experiment. The model used perfectly clamped edges with no slipping. In the experiments, fabric slipping occurred more noticeably as the number of target layers increased. The results reported in this chapter suggest that the hybrid particle-element method used in the simulations can provide good estimates of the residual velocities for normal obliquity aluminum cylinder projectile and steel disk projectile impacts on neat Kevlar and some STF Kevlar targets. Simulations of STF Kevlar impacts appear to overpredict the ballistic performance of STF Kevlar against these projectiles.

5.7.1 Aluminum Cylinder Projectile

Simulation results are summarized in Table 5.3 and compared to the experimental data for the aluminum cylinder impacts on Kevlar with two clamped and two free edges. The experimental impact velocities were consistent within a narrow range, and from Chapter 3, the difference of the impact velocities from the averaged high and low impact velocity values can be expressed as a percent by

$$\delta = \frac{V_i - V_i^*}{V_i^*} \cdot 100 \quad (5.47)$$

where V_i^* is the average of the high and low impact velocities

$$V_i^* = \frac{V_i^{high} + V_i^{low}}{2} \quad (5.48)$$

The largest impact velocity difference was 1.57% of the averaged high

and low values showing consistent impact velocities over the different targets. Comparisons of the fraction of impact energy dissipated in the experiments and simulations for both neat and STF targets are in Figures 5.2 and 5.3, respectively. The STF simulation results show a gradual trend of the fraction of impact energy dissipated. Additionally, STF Kevlar seems to offer no significant advantage over neat Kevlar, given the target conditions and considering the limited range of projectile velocity. When the target consisted of four layers, the error between simulation and experiment was significantly greater than the one - three layer targets for both neat and STF Kevlar targets. As the number of layers of a target increases, the target's V_{50} value also increases. When the difference between the impact velocity and V_{50} decreased, as in the case with four layers, boundary condition effects are more significant. Boundary conditions have more influence at low impact velocities because more of the fabric is deformed before the projectile penetrates. In the experiments with a lower number of layers, the projectile penetrates the target before the target can deform to the boundaries. In the experiments with a higher number of layers, the target deforms to the boundaries where the clamped edges allow some slipping of material, effectively allowing more time and material to decelerate the projectile. The simulations modeled a perfectly clamped boundary with no slipping, constraining the target material more than in the experiments.

Figures 5.4 - 5.6 show the simulation results of an aluminum cylinder impacting a two layer STF Kevlar target at 303 m/s at initial configuration, 100 and 138 μsec . Figure 5.7 is an aluminum cylinder impact on two layers

of STF Kevlar at 303 m/s from experiment at 125 μsec for comparison to the simulation.

5.7.2 Steel Disk Projectile

The steel disk impacts on 3, 6, 12, and 24 layers are summarized in Table 5.4 and compared to the experimental data. The largest impact velocity difference was 0.57% of the averaged high and low values showing consistent impact velocities over the different targets. Similar to the aluminum cylinder simulations, the neat Kevlar simulations compare well to the experimental results, and the STF Kevlar simulations overpredict the capability of the STF Kevlar.

Comparisons of the fraction of impact energy dissipated in the experiments and simulations are in Figures 5.8 and 5.9. The impact velocity for the 30 layers of STF Kevlar and 30 and 36 layers of neat Kevlar were the same as the 24 layer experiments since no experiments were conducted beyond 24 layers. The STF simulation results showed a gradual trend of the fraction of impact energy dissipated. However, experimental STF impacts by the steel disk showed an abrupt change in ballistic performance from 12 to 24 layers, suggesting boundary conditions not modeled in these simulations may affect the ballistic performance. When the target consisted of a high number of layers (≈ 24), the error between simulation and experiment was significantly greater than the 3, 6, and 12 layer targets. In the case with 24 layers, boundary condition effects were more considerable. In the experiments, the

projectile has not strained the material to failure before the target deformation has reached the boundary, so some target material slipped at the clamped boundary, allowing more material and time to slow and stop the projectile. In simulation, the boundary condition was modeled as perfectly clamped with no slipping. Increasing the number of layers in simulation showed that 30 layers of STF Kevlar and 36 layers of neat Kevlar were required to stop the steel disk compared to the 24 layers for each in the experiment.

Figures 5.10 - 5.12 show the simulation results of a steel disk impacting a three layer neat Kevlar target at 296 m/s at initial configuration, 110 and $188\text{ }\mu\text{sec}$. Figure 5.13 is a steel disk impact on three layers of neat Kevlar at 296 m/s from experiment at $200\text{ }\mu\text{sec}$ for comparison to the simulation.

5.7.3 Multilayer Model

Steel disk experiments consisted of 3, 6, 12, and 24 layers of Kevlar. In order to decrease computational time, simulations for the corresponding experiments used a multilayer representation for the Kevlar where three layers of Kevlar were simulated as one layer of Kevlar with an equivalent thickness to the three individual layers. All material properties for the simulations remained the same. Simulations for the steel disk impacts show good agreement with experimental results when employing the multilayer model for the 3, 6, and 12 layer simulations. With 24 layers, simulations differed significantly from experiments and are discussed in the previous section.

A multilayer comparison was conducted with the aluminum cylinder

simulations to assess time savings and accuracy. For these simulations, two layers of experimental Kevlar were represented as one layer of Kevlar with an equivalent thickness to the two individual layers. These additional simulations were only conducted for the two and four layer neat and STF aluminum cylinder impacts. Results are summarized in Table 5.5. These results show that the multilayer model overpredicted the Kevlar's performance compared to the individual layer representation and resulted in lower residual velocities for the aluminum cylinder impacts on two layers. However, in the four layer cases, the multilayer representation resulted in residual velocities closer to the experimental data. Although these differences exist between the individual and multiple layer representations, the computational efficiency of the multilayer model can be seen in the table. Additionally, the computational costs for the aluminum cylinder and steel disk simulations are summarized in Tables 5.6 and 5.7, respectively. These results show the increased cost by layer and demonstrate that the computational cost of high resolution models is significant.

5.8 Summary

A material mixture model was formulated, extending a hybrid particle-element method, for use in three dimensional simulations of impact problems. Extensions of the previous work include the development of a STF mixture equation of state, a rate dependent friction model for the STF Kevlar, and a Bingham shear stress model to represent STF effects. The material model

was developed to investigate aluminum cylinder and steel disk impacts on STF Kevlar. The model was validated against known experimental data of different projectile and target geometries. Such simulation results can be used in computer aided design of advanced fan containment systems for aircraft. Improvements also include a seventh order polynomial for the equation of state of silica used as an STF constituent. Additionally, a comparison of computer resource requirements for modeling each individual layer and modeling multiple layers as one layer was presented. It should be noted that these simulations represent a very specific set of projectiles and boundary conditions in a limited range of impact velocity. However, these simulations show that this model can serve as a supplement to experimental work in the analysis and design process for impact protection systems. The ability of STF Kevlar to absorb projectile energy suggest accurate models and material properties are necessary in simulations over a range of velocities.

Future work suggestions include: 1) additional mechanical property testing is needed, especially at high strain rates, to support development and validation of improved strength models for STF Kevlar, 2) additional equation of state research is needed to provide tabulated data for STF Kevlar components over a range of impact velocities, 3) additional experimental data with different STF Kevlar compositions is needed to further validate the mixture model, and 4) further modeling work is needed to develop a multiple layer representation that provides simulation results consistent with individual layer representation and reduces computational time.

Table 5.1: Coefficients for a seven term polynomial Mie-Gruneisen equation of state for silica [43]

Constant	Value
A_0 (<i>Mbar</i>)	0
A_1 (<i>Mbar</i>)	0.8737
A_2 (<i>Mbar</i>)	-1.7087
A_3 (<i>Mbar</i>)	1.1857
B_0	0.0377
B_1	0.667
B_2	0

Table 5.2: Material properties used in the STF impact simulations [1, 6, 36, 43, 45, 58, 66]

Property	Neat KM-2 fiber		Silica		PEG 200	
		Ref		Ref		Ref
Mass fraction	0.8000		0.1333		0.0667	
Shear modulus (<i>Mbar</i>)	0.2574	cc	0.310	[7]	na	
Reference density (<i>g/cm³</i>)	1.45	[45]	2.22	[66], p.321	1.1239	[1]
Reference Sound Speed (<i>cm/μsec</i>)	0.5352	[36], p.229	5960	[43], p.2	0.1658	[62]
Melt/char temperature (<i>degrees K</i>)	700	[36], p.229	1983	[110], p.1	208	[1]
Specific heat (<i>Mbar · cm³ per g · kilodegrees K</i>)	0.0142	[36], p.229	0.0073	[43], p.2	0.0072	[1]
Thermal expansion coefficient (<i>per kilodegrees K</i>)	0.038	[58], p.160	0.00166	[43], p.2	0.72	[6], p.51
Mie-Gruneisen gamma	0.7666	[36], p.229	0.0377	[43], p.2	0.9092	
Mie Gruneisen slope coefficient	1.0	[36], p.229	1.0	[66], p.321	1.55	[66], p.562

na = not applicable

cc = calculated from isotropic elastic materials

Table 5.3: Simulation results: aluminum cylinder impacts on neat and STF Kevlar with two edges clamped and two edges free

Number of Layers	Kevlar	V_i (m/s)	δ (%)	Exp V_r (m/s)	Sim V_r (m/s)	Exp $\frac{V_r}{V_i}$	Sim $\frac{V_r}{V_i}$
1	Neat	306	1.57	288	282	0.941	0.922
2	Neat	303	0.66	253	255	0.860	0.842
3	Neat	299	-0.76	211	219	0.706	0.732
4	Neat	297	-1.57	0	173	0	0.582
1	STF	298	-1.06	285	269	0.956	0.903
2	STF	301	-0.25	267	241	0.887	0.801
3	STF	298	-1.16	0	184	0	0.617
4	STF	297	-1.57	0	89	0	0.300

Table 5.4: Simulation results: steel disk impacts on neat and STF Kevlar with all edges clamped

Number of Layers	Kevlar	V_i (m/s)	δ (%)	Exp V_r (m/s)	Sim V_r (m/s)	Exp $\frac{V_r}{V_i}$	Sim $\frac{V_r}{V_i}$
3	Neat	296	0.57	283	281	0.956	0.949
6	Neat	295	-0.05	256	261	0.868	0.885
12	Neat	295	0.16	213	228	0.722	0.773
24	Neat	293	-0.57	0	150	0	0.512
30	Neat	297			93		0.313
36	Neat	297			0		0
3	STF	294	-0.36	273	277	0.929	0.942
6	STF	296	0.36	272	257	0.919	0.868
12	STF	294	-0.47	265	211	0.901	0.718
24	STF	297	0.57	0	93	0	0.313
30	STF	297			0		0

Table 5.5: Simulation results: aluminum cylinder impacts on multiple layers modeled as a single layer

Exp No. of Layers	Sim No. of Layers	Kevlar	V_i Exp (m/s)	V_r Exp (m/s)	V_r Sim (m/s)	Sim Time (μs)	Wall Clock hours	System *
2	2	Neat	303	253	255	120	716	p655
2	1	Neat	303	253	241	120	39	p655
2	2	STF	301	267	241	138	883	p655
2	1	STF	301	267	216	140	46	p655
4	4	Neat	297	0	173	258	897	p690
4	2	Neat	297	0	84	260	44	p690
4	4	STF	297	0	89	300	817	p690
4	2	STF	297	0	0	300	49	p690

* IBM p655 node: 8 processors, 1.5 GHz Power 4 CPU

IBM p690 node: 32 processors, 1.7 GHz Power 4 CPU

Table 5.6: Computer resource requirements for the aluminum cylinder impact simulations

No. of Layers	Kevlar	V_i (m/s)	V_r Sim (m/s)	Sim time (μs)	Wall Clock hours	System *
1	Neat	306	282	153	262	p690
2	Neat	303	255	120	716	p655
3	Neat	299	219	237	614	p690
4	Neat	297	173	258	897	p690
1	STF	298	269	154	262	p690
2	STF	300	241	138	883	p655
3	STF	298	184	275	742	p690
4	STF	297	89	300	817	p690

* IBM p655 node: 8 processors, 1.5 GHz Power 4 CPU

IBM p690 node: 32 processors, 1.7 GHz Power 4 CPU

Table 5.7: Computer resource requirements for the steel disk impact simulations

No. of Layers	Kevlar	V_i (m/s)	V_r Sim (m/s)	Sim time (μs)	Wall Clock hours	System *
3	Neat	296	281	189	24	p655
6	Neat	295	261	230	71	p655
12	Neat	295	228	190	71	p655
24	Neat	293	150	330	8	p690
30	Neat	297	93	400	103	p690
36	Neat	297	0	350	107	p690
3	STF	294	277	184	24	p655
6	STF	296	257	190	48	p655
12	STF	294	211	190	71	p655
24	STF	297	96	400	599	p655
30	STF	297	0	350	65	p690

* IBM p655 node: 8 processors, 1.5 GHz Power 4 CPU
 IBM p690 node: 32 processors, 1.7 GHz Power 4 CPU

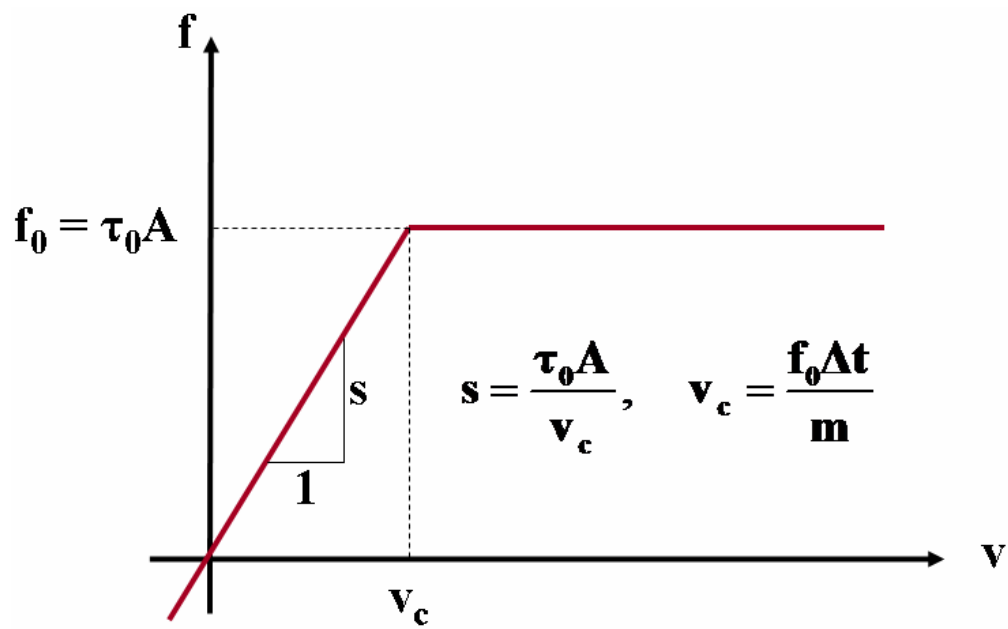


Figure 5.1: Velocity dependent friction model

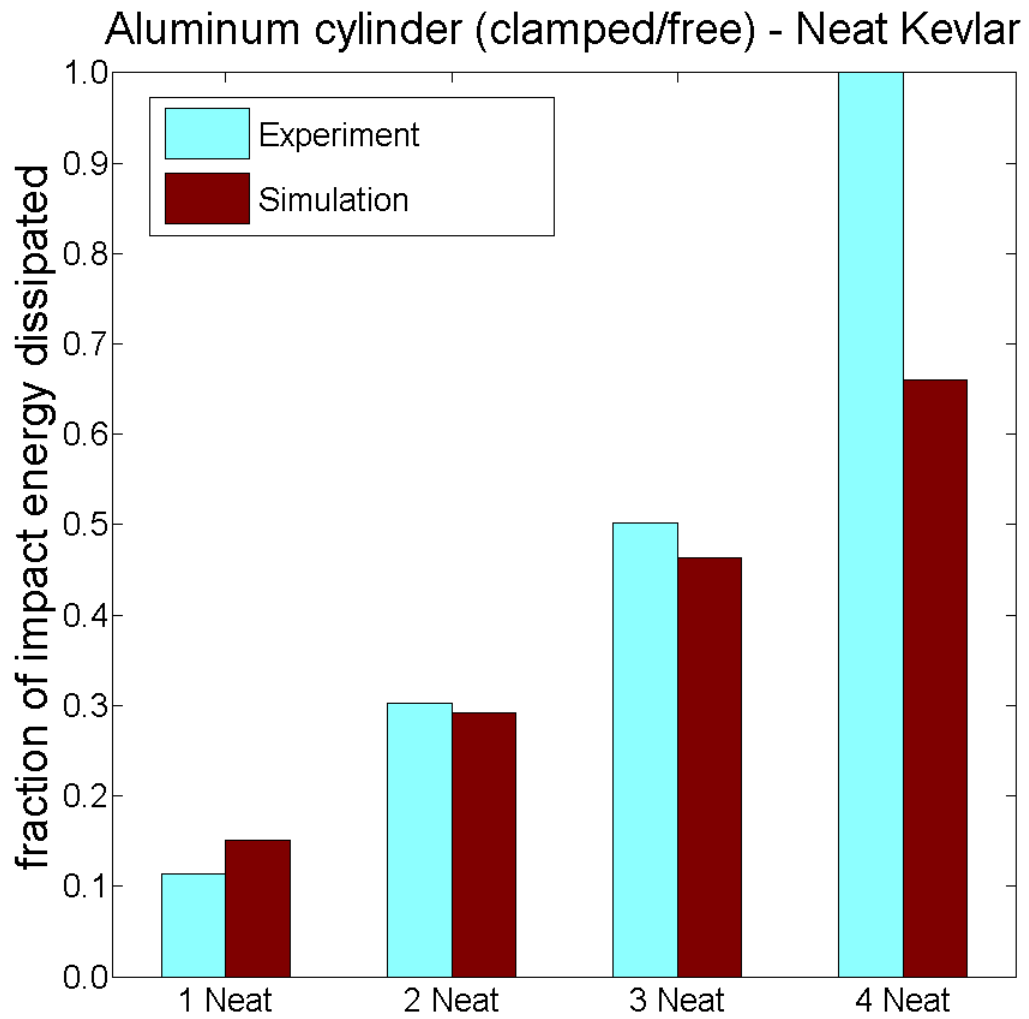


Figure 5.2: Experiment and simulation results: aluminum cylinder impacts on neat targets

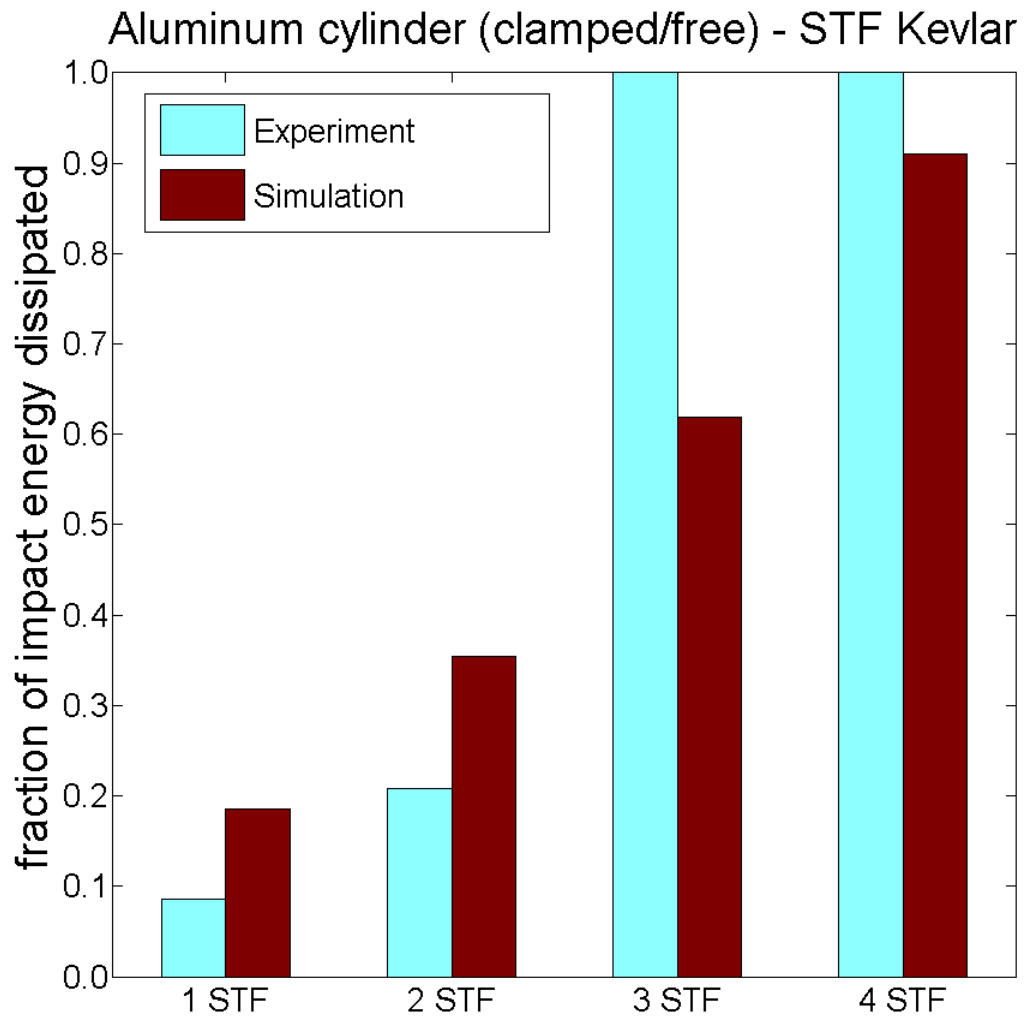


Figure 5.3: Experiment and simulation results: aluminum cylinder impacts on STF targets

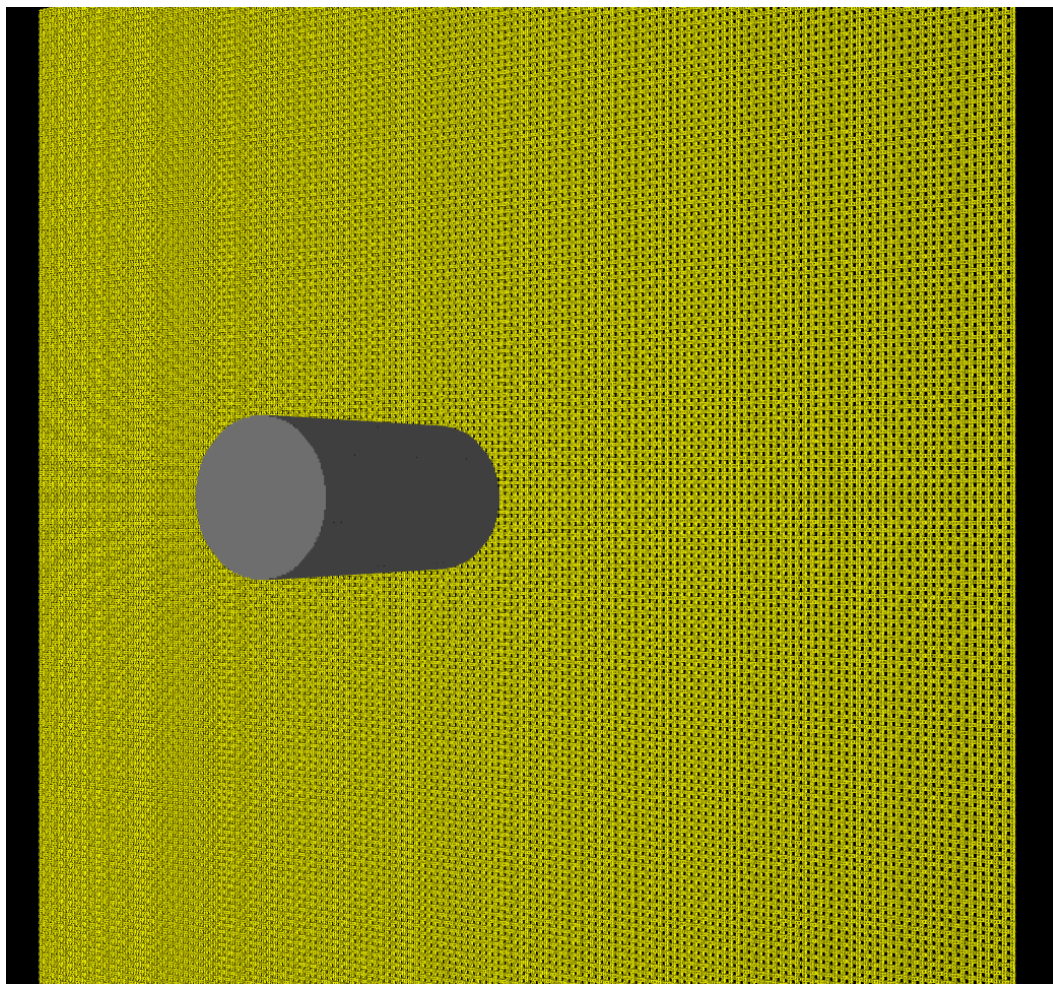


Figure 5.4: Aluminum cylinder impact simulation at 303 m/s on two layers of STF Kevlar with two clamped and two free edges at $0\text{ }\mu\text{sec}$

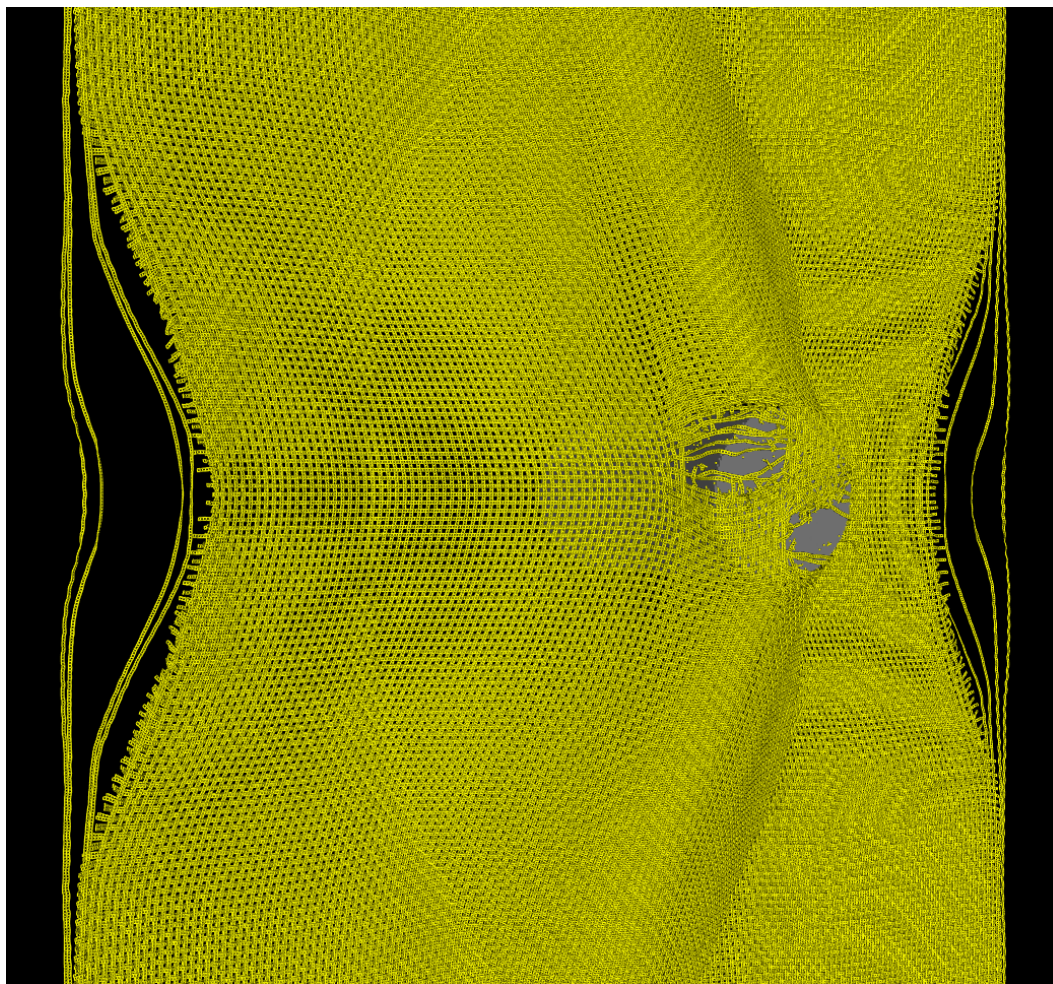


Figure 5.5: Aluminum cylinder impact simulation at 303 m/s on two layers of STF Kevlar with two clamped and two free edges at $73\ \mu\text{sec}$ after impact

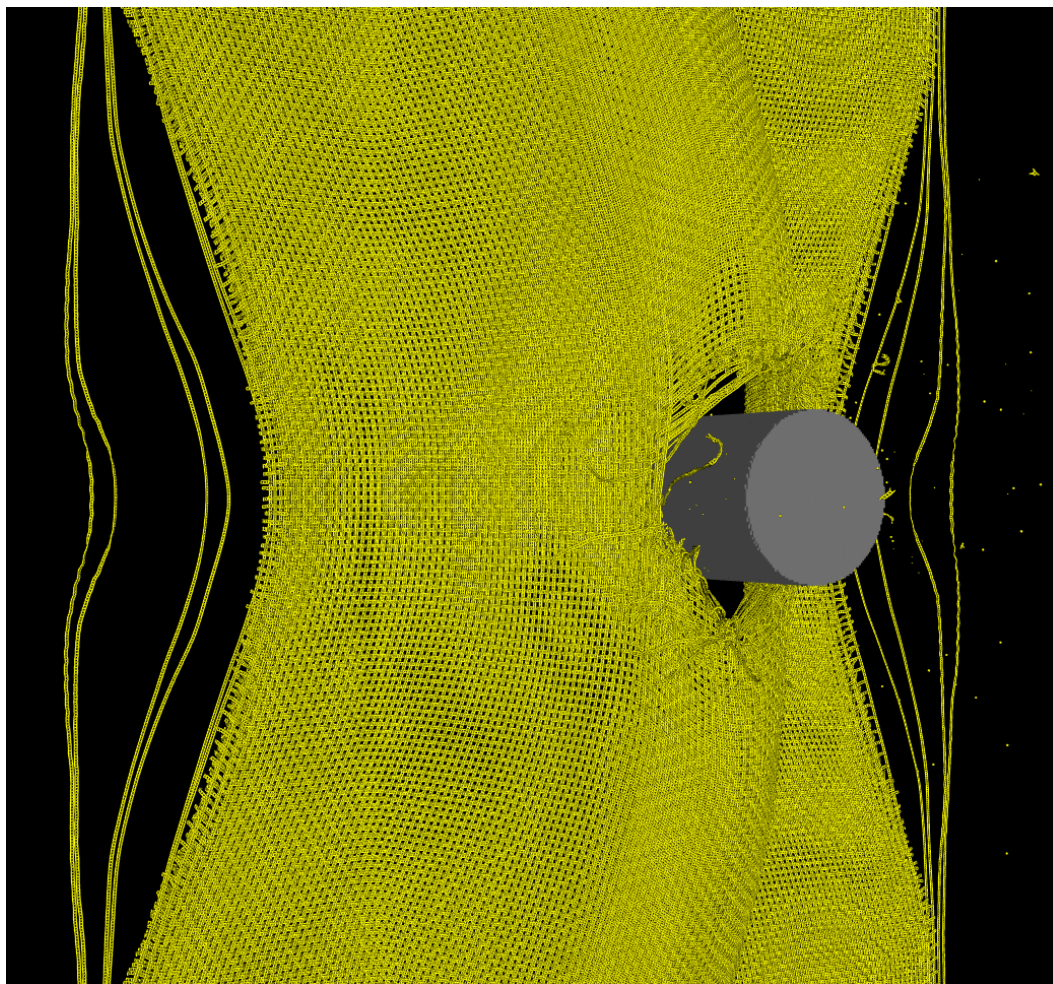


Figure 5.6: Aluminum cylinder impact simulation at 303 m/s on two layers of STF Kevlar with two clamped and two free edges at $138\text{ }\mu\text{sec}$ after impact

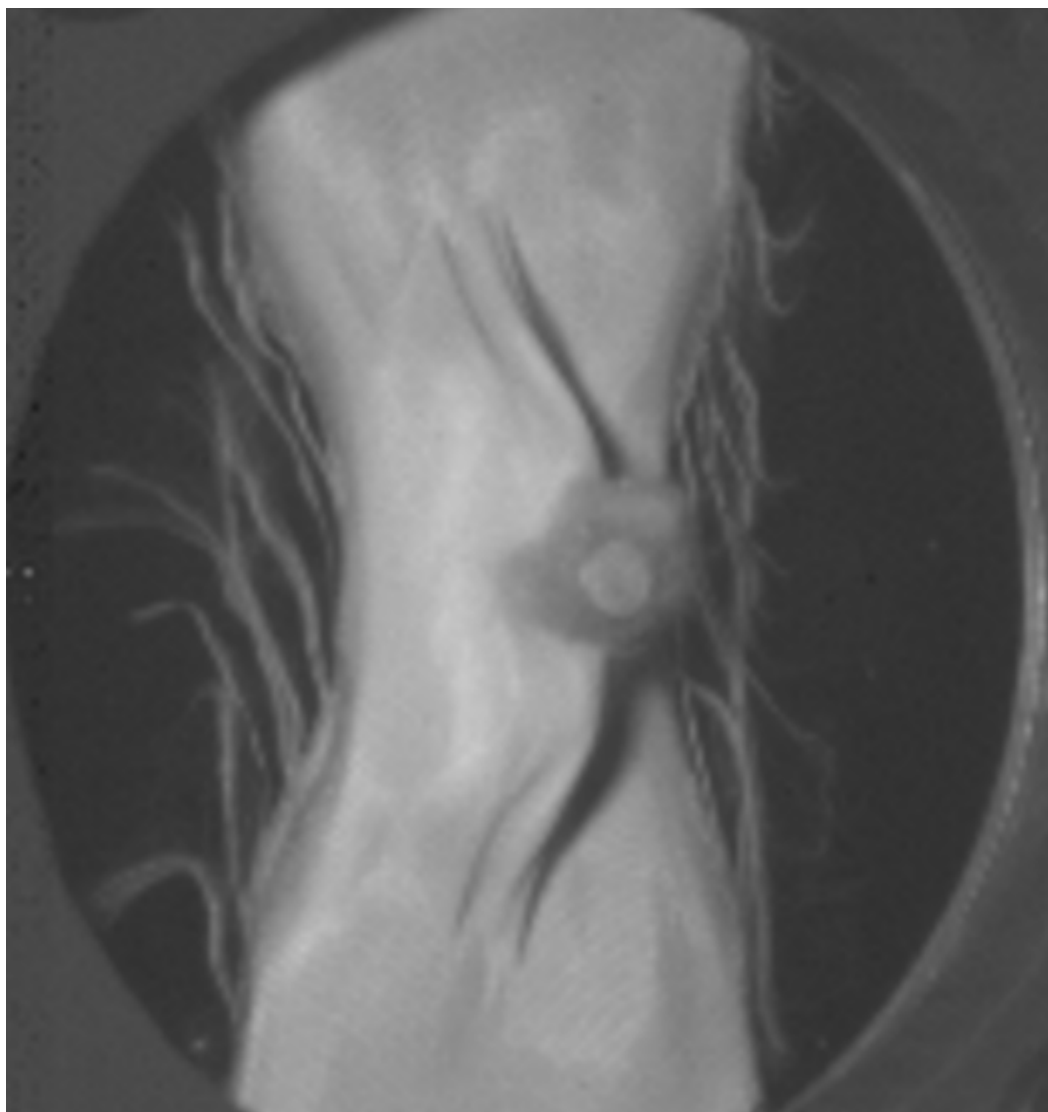


Figure 5.7: Aluminum cylinder impact experiment at 303 m/s on two layers of STF Kevlar with two clamped and two free edges at $125\ \mu\text{sec}$ after impact

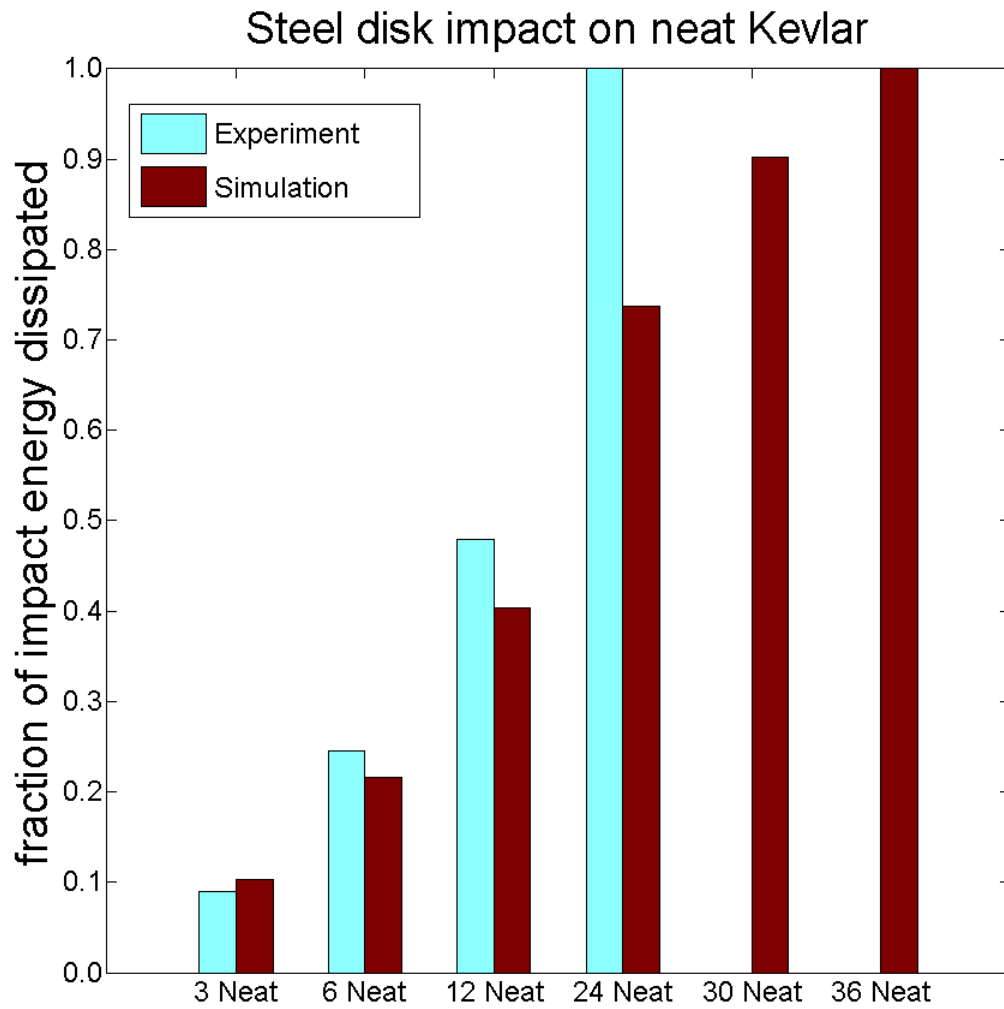


Figure 5.8: Experiment and simulation results: steel disk impacts on neat targets

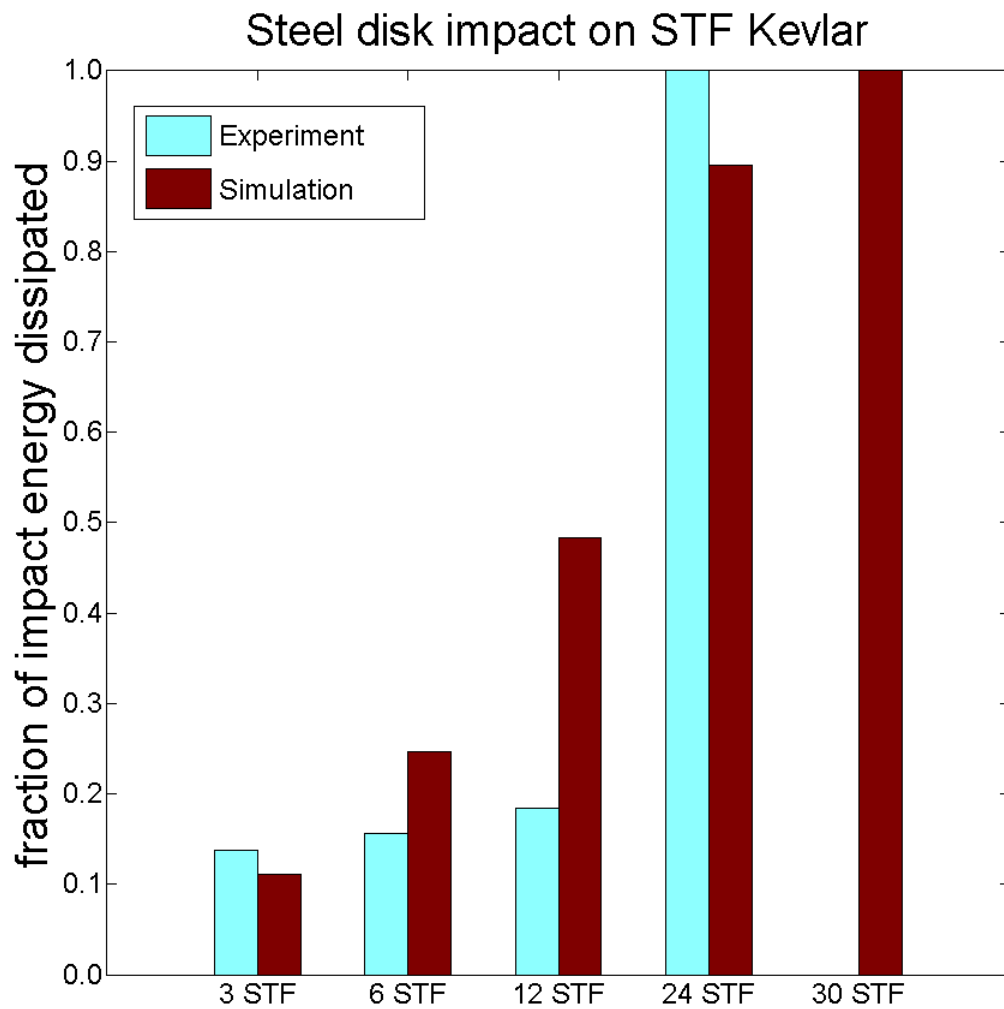


Figure 5.9: Experiment and simulation results: steel disk impacts on STF targets

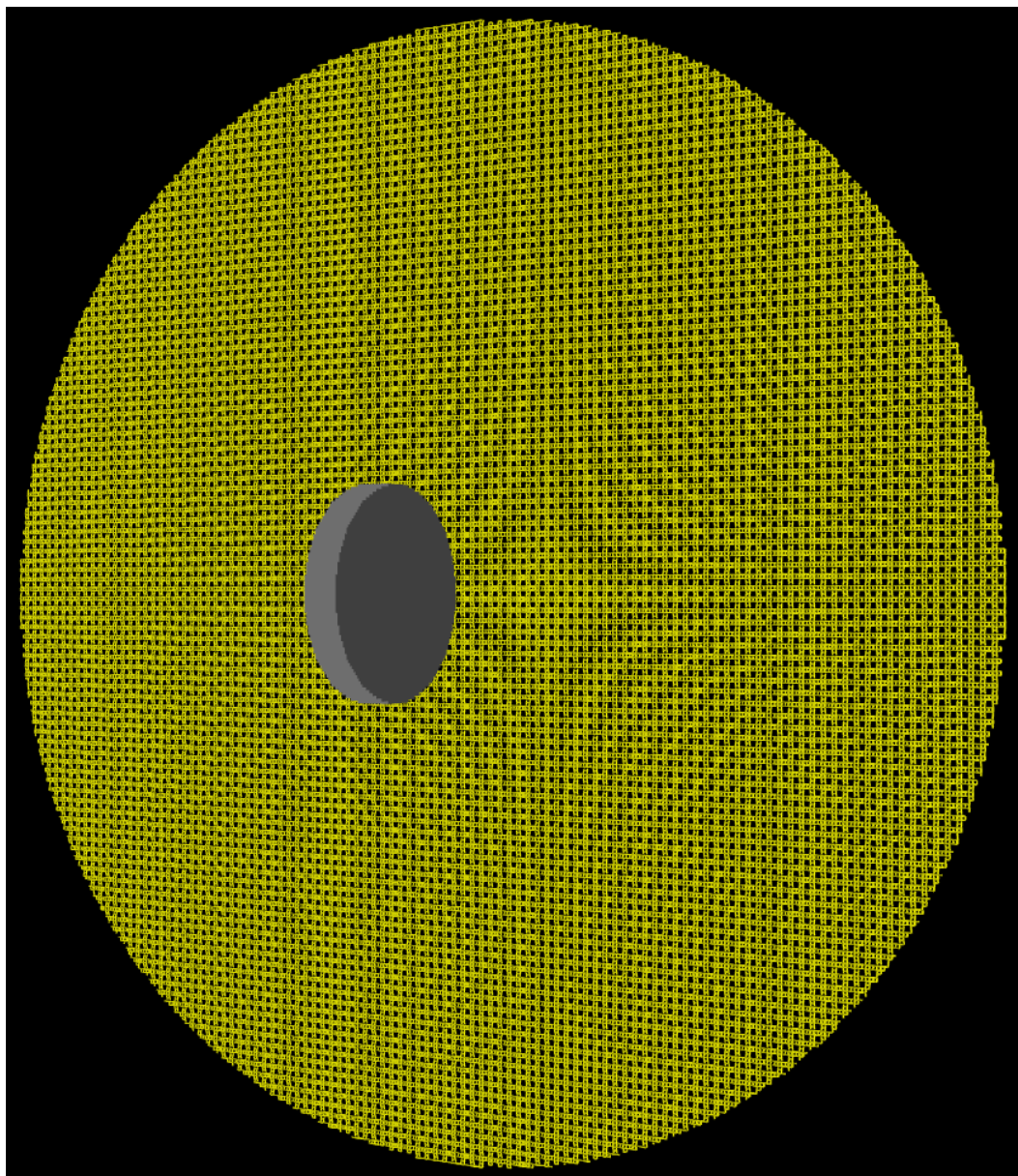


Figure 5.10: Steel disk impact simulation at 296 m/s on three layers of neat Kevlar with clamped edges at $0\ \mu\text{sec}$

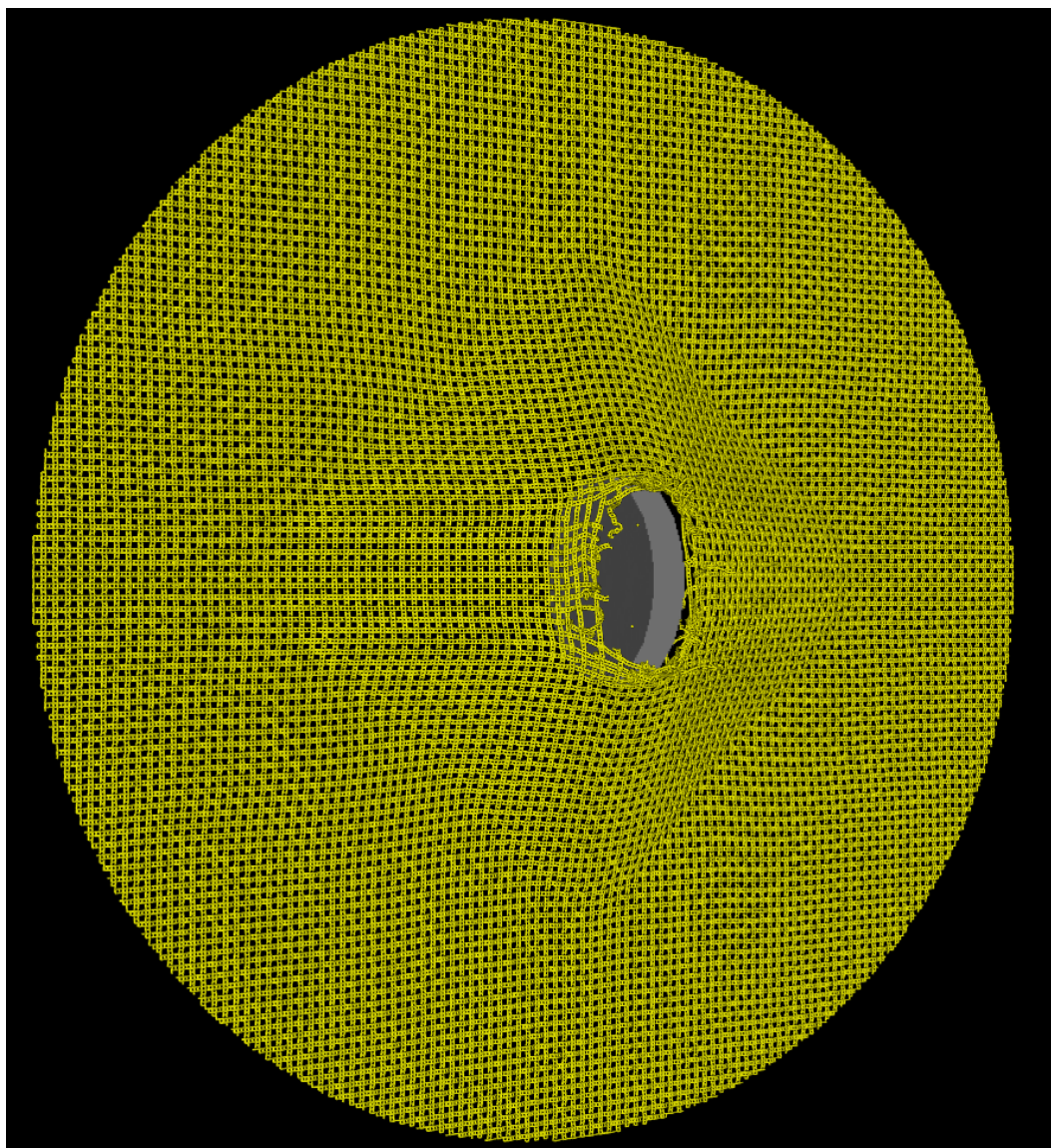


Figure 5.11: Steel disk impact simulation at 296 m/s on three layers of neat Kevlar with clamped edges at $110\text{ }\mu\text{sec}$ after impact

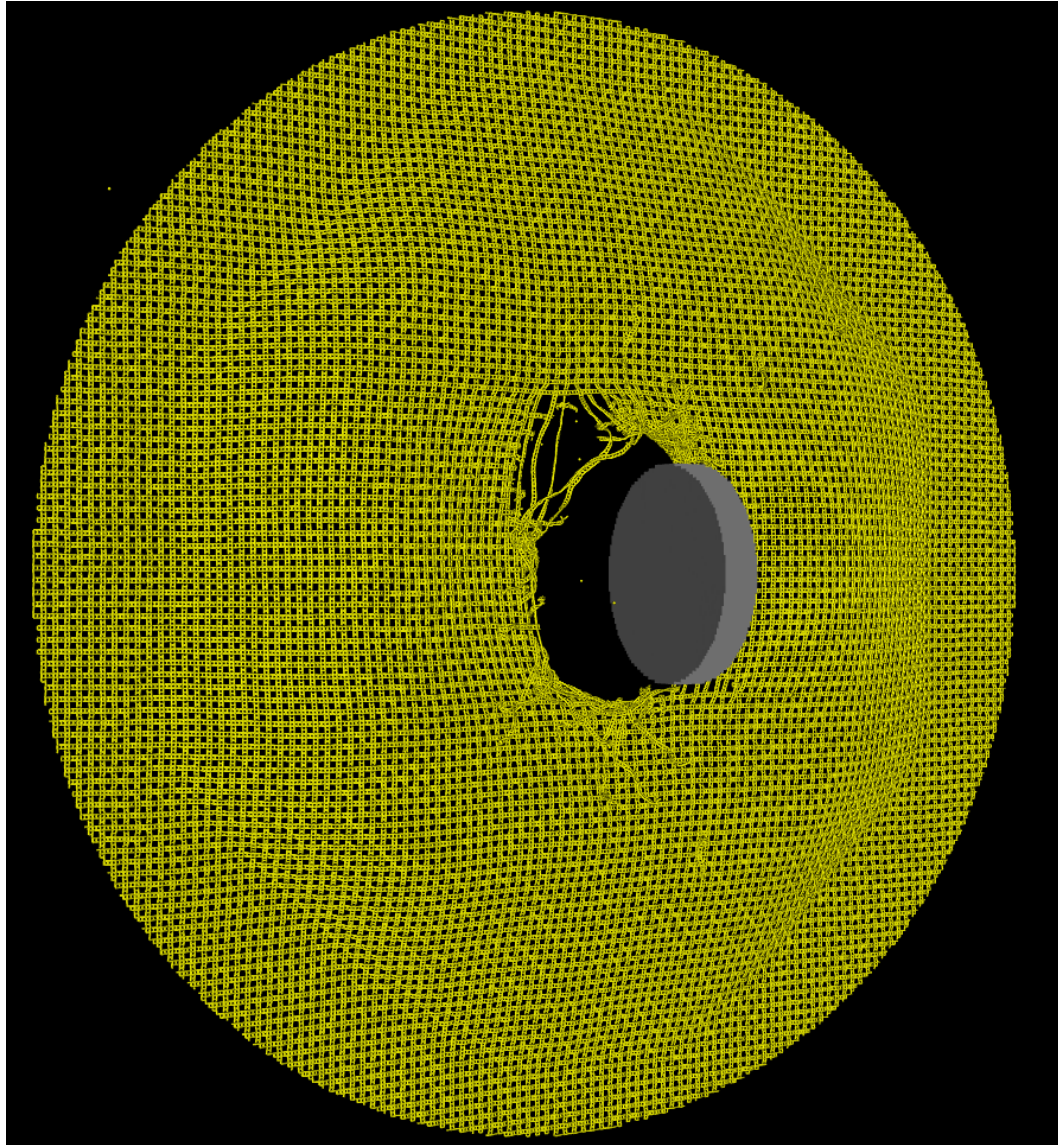


Figure 5.12: Steel disk impact simulation at 296 m/s on three layers of neat Kevlar with clamped edges at $188\ \mu\text{sec}$ after impact

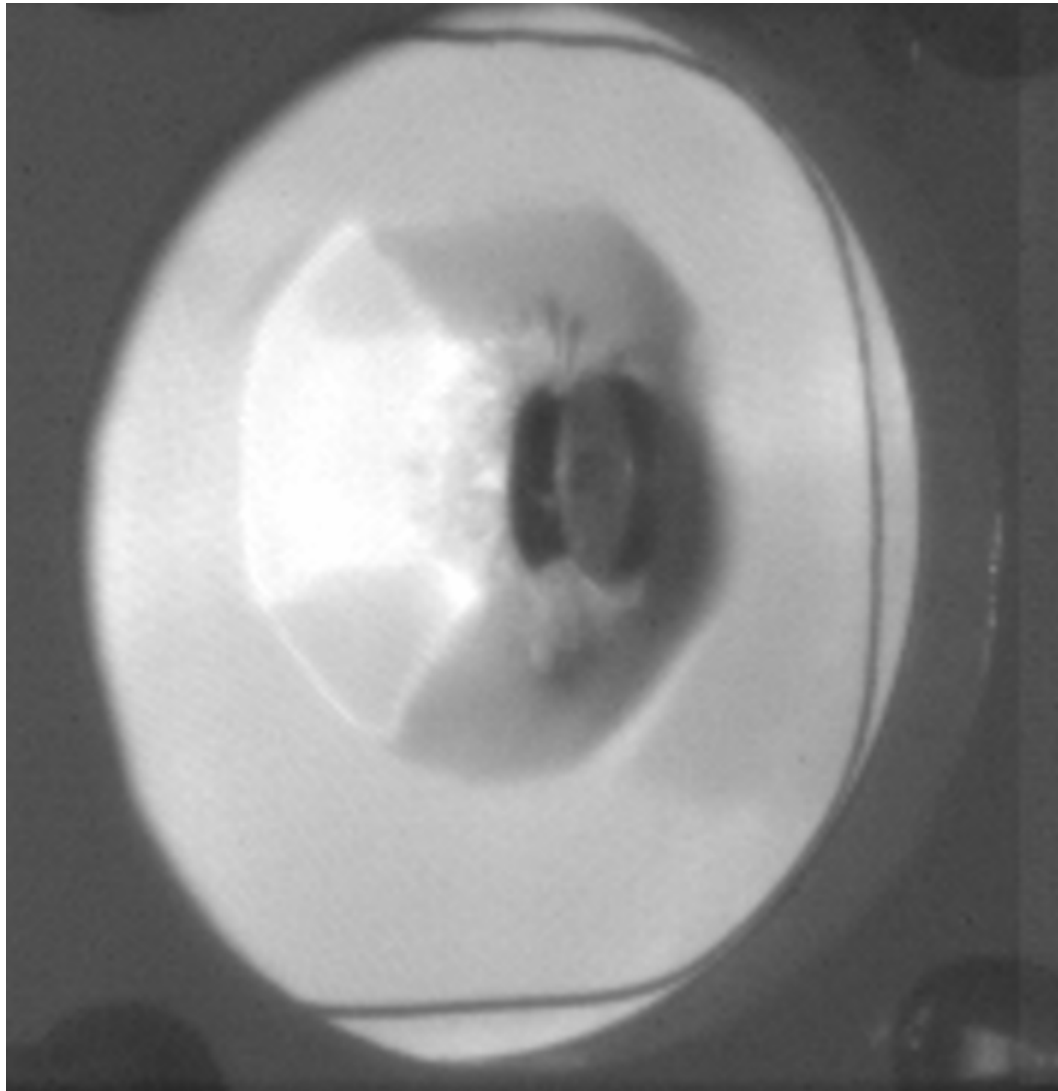


Figure 5.13: Steel disk impact experiment at 296 m/s on three layers of neat Kevlar with clamped edges at $200\ \mu\text{sec}$ after impact

Chapter 6

Conclusion

This dissertation has described the development of a computational hybrid particle-element yarn level model of Kevlar for three dimensional impact simulations of multilayer protection systems. Contributions in numerical modeling include a new yarn level model of ellipsoid particles and bar elements to model the flexible yarns and a velocity dependent friction model to simulate yarn interactions. Advancements in material modeling include a strain rate dependent model for the Kevlar, a Bingham shear stress model for STF effects, and a new mixture equation of state for the STF Kevlar that captured the thermodynamic properties of the constituents. This dissertation also provides new data for FSP impacts on Kevlar with different boundary conditions, residual velocity correlations for the FSP impacts, new data for different projectile impacts on STF and neat Kevlar with different boundary conditions, and the development of a new target fixture for targets with two fixed and two free edges. This chapter presents a summary of the dissertation and recommendations for future work.

Experiments in which fragment simulating projectiles impacted differing layers of neat Kevlar were performed to gain performance data and for

validation of future simulations. Target fixtures allowed testing of targets with two fixed and two free edges as well as all clamped edges. Next, the experimental results provided information to generate an equation for the residual velocity that was applicable to both experimental boundary conditions. This correlation represented the experimental data well over the tested range of impact velocities and was used for validation of future simulations. Future experiments, simulation, and validation work can benefit from these experiments.

Next, impact experiments were performed to compare the performance of neat and STF Kevlar. Aluminum cylinders and steel disks were used as projectiles over a narrow range of velocities. Aluminum cylinder impacts included targets with all clamped edges and with two clamped and two free edges. The steel disk impacts were only on targets with all clamped edges. In general, the neat Kevlar was able to reduce the projectile velocity better than the STF Kevlar with all clamped edges. In the aluminum cylinder impacts on two clamped and two free edges, the STF Kevlar performed quite similarly to the neat Kevlar. In no case was the ballistic performance of STF Kevlar better than the neat Kevlar on a per unit mass basis. A comparison of boundary condition effects showed that targets with unconstrained edges have better ballistic performance. Results of the experiments also suggest that STF Kevlar may not be well-suited for some impact engineering applications. These experiments provided a new database on different projectile geometries for STF impact testing. This data can assist future modeling and simulation

work.

Extending a hybrid particle element method, a new yarn level particle-bar element model and a rate dependent strength model were developed for use in the simulation of FSP impacts on Kevlar targets. Ellipsoidal particles and bar elements were used to model the flexible yarn rather than hex elements. The particle geometry was calculated from actual yarn parameters to provide a woven architecture to simulate the yarn interactions. Next, a strain rate material model was developed to correlate the measured ballistic performance. Simulation results showed that strain rate effects in Kevlar were significant in the FSP impact problem. The current work validated the numerical model, accurately predicting the Kevlar response under the given load conditions and within a reasonable time with current computational resources.

Finally, the hybrid particle-bar element method was further extended by introducing a material mixture model to account for the composition of STF Kevlar. A Bingham shear stress was used to model the STF effects as well as a velocity dependent friction to model the particle interactions. Simulation results showed that the model can provide accurate results for neat Kevlar when the projectile geometry differs. However, the model overpredicted the performance of STF Kevlar, especially with increasing target layers. Boundary conditions play a significant role when the impact velocity of the projectile is low. The model did not allow fabric slip at the boundaries which was present in the experiments. Additionally, a seventh order polynomial Mie-Gruneisen equation of state for silica was presented. Last, modeling multiple layers of

Kevlar as a single layer was presented to compare computational time and accuracy.

Additional research is suggested to improve material models for terminal ballistic applications: 1) higher resolution models at the sub yarn level should be developed to capture the yarn physics and investigate assumptions in the numerical model and geometry of the yarn, 2) more mechanical property testing of STF Kevlar is required, especially at high strain rates, to support development and validation of material models for STF Kevlar, 3) additional experiments to investigate equation of state properties of STF Kevlar are necessary to validate assumptions made in the material model, 4) further impact testing should be performed over a wider range of impact velocities, using different target geometries and boundary conditions to validate the model over a larger region of interest, and 5) additional modeling work on boundary conditions.

Appendices

Appendix A

Residual Velocity Correlation for the FSP Impact Experiments

From Chapter 2, the residual velocity relationship for the FSP data is

$$V_r = V_i \left(1 - e^{-\beta(\frac{V_i}{\alpha} - 1)} - \frac{V_0}{V_i} \right) \quad (\text{A.1})$$

Since $V_r = 0$ at $V_i = V_{50}$, an expression for β can be found by substituting and rearranging the previous equation

$$\beta = -\frac{\ln \left(1 - \frac{V_0}{V_{50}} \right)}{\left(\frac{V_{50}}{\alpha} - 1 \right)} \quad (\text{A.2})$$

To calculate an expression for α , substitute Equation A.2 into A.1 and let λ represent the following term

$$\lambda = \frac{\ln \left(1 - \frac{V_r}{V_i} - \frac{V_0}{V_i} \right)}{\ln \left(1 - \frac{V_0}{V_{50}} \right)} \quad (\text{A.3})$$

Substitution yields the expression for α

$$\alpha = \frac{\lambda V_{50} - V_i}{\lambda - 1} \quad (\text{A.4})$$

Equation A.4 can be used to find an average value for α for the experimental set of data and substituted into Equation A.2 to calculate β .

Appendix B

Strain Rate Dependent Strength Model

From Figure B.1, the intersection of the two lines represents a point where the dynamic failure strain ϵ_f is equal to two functions. One line describes the strain as a function of strain rate (Equation B.1) and the other line defines the strain as a function of the initial failure strain and variable η (Equation B.2). Assume constant slope η and constant strain rate $\dot{\epsilon}$ from Figure B.1

$$\epsilon_f = \dot{\epsilon} t_f \quad (\text{B.1})$$

$$\epsilon_f = \epsilon_{f0} + \eta t_f \quad (\text{B.2})$$

Setting the two equations equal to find the time of failure, t_f yields

$$t_f = \frac{\epsilon_{f0}}{(\dot{\epsilon} - \eta)} \quad (\text{B.3})$$

Substituting t_f back into Equation B.1 results in the following relationship

$$\frac{\epsilon_f}{\epsilon_{f0}} = \frac{\dot{\epsilon}}{\dot{\epsilon} - \eta} = \frac{1}{1 - \frac{\eta}{\dot{\epsilon}}} \quad (\text{B.4})$$

From a series of dynamic uniaxial tension tests from Dooraki [28], the dynamic failure strains were obtained. The rate change in dynamic failure

strain over the test data is represented by γ and is determined experimentally. This relationship is represented in Figure B.2. Relating the ratio of the failure strain to the static failure strain in terms of γ and $\dot{\epsilon}$ yields the following relationship

$$\frac{\epsilon_f}{\epsilon_{f0}} = 1 + \gamma \dot{\epsilon} \quad (\text{B.5})$$

Setting Equations B.4 and B.5 equal gives the following

$$1 + \gamma \dot{\epsilon} = \frac{1}{1 - \frac{\eta}{\dot{\epsilon}}} \quad (\text{B.6})$$

Solving this equation for η yields

$$\eta = \frac{\gamma \dot{\epsilon}^2}{1 + \gamma \dot{\epsilon}} \quad (\text{B.7})$$

Substituting η back into Equation B.2 for the failure strain rate results in $\dot{\epsilon}_f$, the failure strain rate evolution relation

$$\dot{\epsilon}_f = \left[\frac{\gamma \dot{\epsilon}}{1 + \gamma \dot{\epsilon}} \right] \langle \dot{\epsilon} \rangle \quad (\text{B.8})$$

The bracket function $\langle x \rangle$ denotes

$$\langle x \rangle = x \hat{u}(x) \quad (\text{B.9})$$

where \hat{u} is the unit step function, since the strain rate acts in tension only.

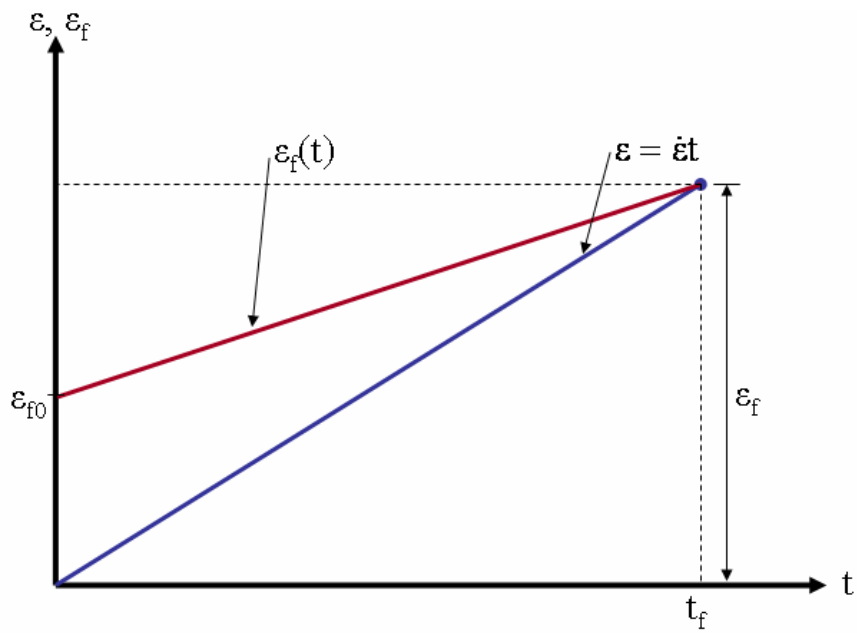


Figure B.1: Strain and failure strain versus time for a constant strain rate test

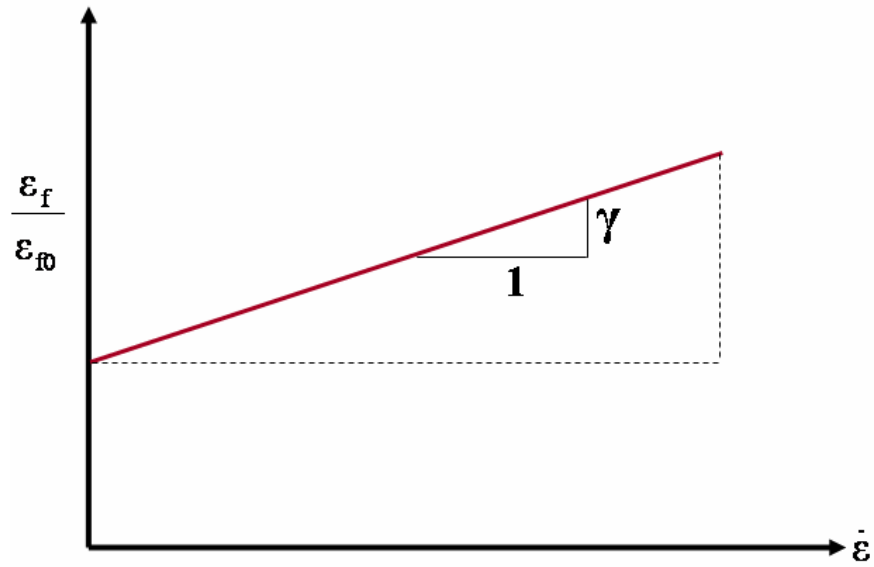


Figure B.2: Normalized failure strain versus strain rate for a constant strain rate test

Bibliography

- [1] Carbowax polyethylene glycol 200 Form no. 118-01251-0905-KMG. Dow Chemicals.
- [2] Projectile, calibers .22, .30, .50, and 20mm fragment simulating. Mil-P-46593A, 1962.
- [3] Textile test methods textiles-woven fabrics- construction- methods of analysis-part 3: Determination of crimp of yarn in fabric. ISO 7211-3, 1984.
- [4] Standard terminology relating to textiles. ASTM D 123-03, 2003.
- [5] Standard test methods for yarn crimp and yarn take-up in woven fabrics. ASTM D 3883-04, 2004.
- [6] PEGs and MPEGs Form no. 119-01260-0306 AMS. Dow Chemicals, March 2006.
- [7] Accuratus Corporation. Fused Silica, SiO₂, 2007. <http://www.accuratus.com/fused.html>.
- [8] T.J. Ahrens and M.L. Johnson. *Mineral Physics and Crystallography. A Handbook of Physical Constants*, chapter 10: Shock Wave Data for Minerals. American Geophysical Union, 1995. pp. 143-184.

- [9] R. Barauskas and A. Abraitienė. Computational analysis of impact of a bullet against the multilayer fabrics in LS-DYNA. *International Journal of Impact Engineering*, 34:1286–1305, 2007.
- [10] T. Belytschko, Y. Krongauz, D. Organ, M. Fleming, and P. Krysl. Meshless methods: an overview and recent developments. *Computer Methods in Applied Mechanics and Engineering*, 139:3–47, 1996.
- [11] G. Ben-Dor, A. Dubinsky, and T. Elperin. On the Lambert-Jonas approximation for ballistic impact. *Mechanics Research Communications*, 29:137–139, 2002.
- [12] H.H. Billon. A model for ballistic impact on soft armour. Technical Report DSTO-TR-0730, Aeronautical and Maritime Research Laboratory, Melbourne, Australia, October 1998.
- [13] H.H. Billon and D.J. Robinson. Models for the ballistic impact of fabric armour. *International Journal of Impact Engineering*, 25:411–422, 2001.
- [14] G. Blankenhorn, K. Schweizerhof, and H. Finckh. Improved numerical investigations of a projectile impact on a textile structure. In *Drop Test / Impact I*, pages G–I–07–14, Ulm, Germany, May 2003. 4th European LS-DYNA Users Conference.
- [15] J.P. Borg, D.J. Chapman, K. Tsembeles, W.G. Proud, and J.R. Cougar. Dynamic compaction of porous silica powder. *Journal of Applied Physics*, 98:1–5, 2005.

- [16] B.J. Briscoe and F. Motamedi. The ballistic impact characteristics of aramid fabrics: the influence of interface friction. *Wear*, 158:229–247, 1992.
- [17] K. Carney, M. Pereira, D. Revilock, and P. Matheny. Jet engine fan blade containment using two alternate geometries. In *Aerospace / Fluid-Structure*, pages I–I–01–10, Ulm, Germany, May 2003. 4th European LS-DYNA Users Conference.
- [18] B.A. Cheeseman and T.A. Bogetti. Ballistic impact into fabric and compliant composite laminates. *Composite Structures*, 61:161–173, 2003.
- [19] B.A. Cheeseman et. al. From filaments to fabric packs - simulating the performance of textile protection systems. Proceedings of the Army Science Conference, 2006.
- [20] M. Cheng, W. Chen, and T. Weerasooriya. Experimental investigation of the transverse mechanical properties of a single Kevlar KM2 fiber. *International Journal of Solids and Structures*, 41:6215–6232, 2004.
- [21] R.P. Chhabra and J.F. Richardson. *Non-Newtonian Flow in the Process Industries*. Butterworth-Heineman, Woburn, MA, 1999.
- [22] L.L. Clements. *Handbook of Composites*, chapter 10 Organic Fibers. Chapman and Hall, London, UK, 1998. 202-241.
- [23] C.R. Cork and P.W. Foster. The ballistic performance of narrow fabrics. *International Journal of Impact Engineering*, 34:495–508, 2007.

- [24] C. Cornwell and D. Richie. Final project technical report: Advanced body armor utilizing nanotechnology. Technical Report DAAD05-01-C-0033, Programming Environment and Training (PET) Program High Performance Computing Modernization Program Office (HPCMPO), July 2004.
- [25] P.M. Cunniff and J. Ting. Development of a numerical model to characterize the ballistic behavior of fabrics. Proceedings of the 18th International Symposium on Ballistics, San Antonio, TX, November 1999.
- [26] G.J. Czarnecki. Estimation of the V50 using semi-empirical (1-point) procedures. *Composites Part B*, 29B:321–329, 1998.
- [27] M.J. Decker, R.G. Egres, E.D. Wetzel, and N.J. Wagner. Low velocity ballistic properties of shear thickening fluid (STF) - fabric composites. Proceedings of the 22nd International Symposium on Ballistics, Vancouver, BC, November 2005.
- [28] B.F. Dooraki, J.A. Nemese, and M. Bolduc. Study of parameters affecting the strength of yarns. *Journal of Physics IV France*, 134:1183–1188, 2006.
- [29] Y. Duan, M. Keefe, T.A. Bogetti, and B. Cheeseman. Modeling the role of friction during ballistic impact of a high strength plain weave fabric. *Composite Structures*, 68:331–337, 2005.

- [30] Y. Duan, M. Keefe, T.A. Bogetti, B.A. Cheeseman, and B. Powers. A numerical investigation of the influence of friction on energy absorption by a high-strength fabric subjected to ballistic impact. *International Journal of Impact Engineering*, 32:1299–1312, 2006.
- [31] Y. Duan, M. Keefe, T.A. Bogetti, and B. Powers. Finite element modeling of transverse impact on a ballistic fabric. *International Journal of Mechanical Sciences*, 48:33–43, 2006.
- [32] Y. Duan, M. Keefe, E.D. Wetzel, T.A. Bogetti, B. Powers, J.E. Kirkwood, and K.M. Kirkwood. Effects of friction on the ballistic performance of a high-strength fabric structure. *WIT Transactions on Engineering Sciences*, 49:1–12, 2005.
- [33] DuPont. Kevlar brand fiber. MSDS Safety Information, November 1999.
- [34] R.G. Egres Jr., M.J. Decker, C.J. Halbach, Y.S. Lee, J.E. Kirkwood, K.M. Kirkwood, and N.J. Wagner. Stab resistance of shear thickening fluid (STF) Kevlar composites for body armor applications. Proceedings for the 24th Army Science Conference, Orlando, FL, December 2005.
- [35] General Electric Aircraft Engines. Smart fan containment system. Technical Report NASA CR2005-213969, National Aeronautics and Space Administration, Washington, DC, November 2005.

- [36] E.P. Fahrenthold and Y.K. Park. Simulation of hypervelocity impact on aluminum-nextel-kevlar orbital debris shields. *International Journal of Impact Engineering*, 29:227–235, 2003.
- [37] C. Frankenberger and W. Emmerling. Improving commercial aircraft survivability. *Aircraft Survivability*, pages 6–9, Spring 2005.
- [38] D.J. Grosch. Fragment impact testing of kevlar panels. Technical report, Southwest Research Institute, May 2006.
- [39] D.J. Grosch. SwRI project no. 18054.01.020, .22 caliber fsp impact studies. Technical Report 18054.01.020, Southwest Research Institute, April 2006.
- [40] D.J. Grosch. SwRI project no. 18071.02.001, .22 caliber fsp impact studies. Technical Report 18071.02.001, Southwest Research Institute, November 2006.
- [41] D.J. Grosch. SwRI project no. 18.18054.01.042, fragment impact testing of kevlar panels. Technical Report 18.18054.01.042, Southwest Research Institute, December 2006.
- [42] J.O. Hallquist. *Theoretical Manual for DYNA3D*. Lawrence Livermore National Laboratory, Livermore, CA, 1983.
- [43] D.E. Hare and R.A. Managan. CALE EOS form 2 fits for high pressure fused silica hugoniot data. Technical Report UCRL-TR-217957, Lawrence Livermore National Laboratory, January 2006.

- [44] Hexcel Corporation. Email discussion of yarn crimp in style 706 fabric.
- [45] Hexcel Schwebel. 706 aramid and high performance fabrics product data, 2006. <http://www.hexcel.com/NR/rdonlyres/7DA2C888-CC39-43F7-A071-24CEEB8DD9EC/0/706.pdf>.
- [46] B.A. Horban and E.P. Fahrenthold. Hamilton's equations for impact simulations with perforation and fragmentation. *Journal of Dynamic Systems, Measurement, and Control*, 127:617–622, 2005.
- [47] I. Ivanov and A. Tabiei. Loosely woven fabric model with viscoelastic crimped fibres for ballistic impact simulations. *International Journal for Numerical Methods in Engineering*, 61:1565–1583, 2004.
- [48] P. Jearanaisilawong. Investigation of deformation and failure mechanisms in woven and nonwoven fabrics under quasi static loading conditions. Master's thesis, Massachusetts Institute of Technology, Cambridge, MA, September 2004.
- [49] G.R. Johnson, S.R. Beissel, and P.M. Cunniff. A computational model for fabrics subjected to ballistic impact. Proceedings of the 18th International Symposium on Ballistics, San Antonio, TX, November 1999.
- [50] G.R. Johnson and R.A. Stryk. Conversion of 3D distorted elements into meshless particles during dynamic deformation. *International Journal of Impact Engineering*, 28:947–966, 2003.

- [51] L. Karaoglan, A.K. Noor, and Y.H. Kim. Frictional contact/impact response of textile composite structures. *Composite Structures*, 37:269–280, 1997.
- [52] M.J. King, P. Jearanaisilawong, and S. Socrate. A continuum constitutive model for the mechanical behavior of woven fabrics. *International Journal of Solids and Structures*, 42:3867–3896, 2005.
- [53] K.M. Kirkwood, J.E. Kirkwood, Y.S. Lee, R.G. Egres, E.D. Wetzel, and N.J. Wagner. Yarn pull-out as a mechanism for dissipation of ballistic impact energy in Kevlar KM-2 fabric, Part I: Quasi-static characterization of yarn pull-out. Technical Report ARL-CR-537, Army Research Lab, Aberdeen Proving Ground, MD, May 2004.
- [54] K.M. Kirkwood, J.E. Kirkwood, Y.S. Lee, R.G. Egres, E.D. Wetzel, and N.J. Wagner. Yarn pull-out as a mechanism for dissipation of ballistic impact energy in Kevlar KM-2 fabric, Part II: Prediction of ballistic performance. Technical Report ARL-CR-538, Army Research Lab, Aberdeen Proving Ground, MD, May 2004.
- [55] J.P. Lambert and G.H. Jonas. Towards standardization in terminal ballistics testing: velocity representation. Technical Report BRL R 1852, USA Ballistic Research Laboratories, Aberdeen Proving Ground, MD, January 1976.
- [56] D.D. Le. Evaluation of lightweight material concepts for aircraft tur-

- bine engine rotor failure protection. Technical Report DOT/FAA/AR-96/110, Office of Aviation Research, Washington, DC, July 1997.
- [57] A. Leal, J.M. Deitzel, A. Chatterjee, A. Abu-Obaid, J.W. Gillespie, C. Hoppel, and P.M. Cunniff. Mechanical properties and surface characteristics of novel high-performance organic fibers. In L.J. Cohen, C. Ong, and C. Arendt, editors, *48th International SAMPE Symposium and Exhibition*, pages 793–803, Long Beach, CA, May 2003. SAMPE.
- [58] S.L. Lee. *Reference Book for Composites Technology*, volume 1. Technomic Publishing Co., Lancaster, PA, 1989.
- [59] Y.S. Lee and N.J. Wagner. Dynamic properties of shear thickening colloidal suspension. *Rheological Acta*, 42:199–208, 2003.
- [60] Y.S. Lee, E.D. Wetzel, and N.J. Wagner. Advanced body armor utilizing shear thickening fluids. Proceeding of 23rd Army Science Conference, Orlando, FL, December 2002.
- [61] Y.S. Lee, E.D. Wetzel, and N.J. Wagner. The ballistic impact characteristics of kevlar woven fabrics impregnated with a colloidal shear thickening fluid. *Journal of Materials Science*, 38:2825–2833, 2003.
- [62] D.R. Lide. *Handbook of Chemistry and Physics*. CRC Press, Boca Raton, Florida, 81st edition, 2001.

- [63] C.T. Lim, V.P. Shim, and Y.H. Ng. Finite-element modeling of the ballistic impact of fabric armor. *International Journal of Impact Engineering*, 28:13–31, 2003.
- [64] M.R. Lindeburg. *Mechanical Engineering Reference Manual*. Professional Publications, Inc., Belmont, CA, 11 edition, 2001.
- [65] B.J. Maranzano and N.J. Wagner. The effects of interparticle interactions and particle size on reversible shear thickening: Hard-sphere colloidal dispersions. *Journal of Rheology*, 45:1205–1222, 2001.
- [66] S. Marsh. *LASL Shock Hugoniot Data*. University of California Press, Berkeley, California, 1980.
- [67] M.A. Martinez, C. Navarro, R. Cortes, and J. Rodriguez. Friction and wear behaviour of Kevlar fabrics. *Journal of Materials Science*, 28:1305–1311, 1993.
- [68] J.M. McGlaun, S.L. Thompson, and M.G. Elrick. CTH: A three dimensional shock wave physics code. *International Journal of Impact Engineering*, 10:351–360, 1990.
- [69] T.J. Mulkern and M.N. Raftenberg. Kevlar KM2 yarn and fabric strength under quasi-static tension. Technical Report ARL-TR-2865, Army Research Lab, Aberdeen Proving Ground, MD, October 2002.
- [70] B. Nadler and D.J. Steigmann. A model for frictional slip in woven fabrics. *C.R. Mecanique*, 331:797–804, 2003.

- [71] N.K. Naik, P. Shrirao, and B.C.K. Reddy. Ballistic impact behaviour of woven fabric composites: Parametric studies. *Materials Science and Engineering A*, 412:104–116, 2005.
- [72] C.H. Nam et. al. CTH: Ballistic and rheological properties of STFs reinforced by short discontinuous fibers. SAMPE, Long Beach, CA, May 2005.
- [73] R. Nennstiel. Prediction of the remaining velocity of some handgun bullets perforating thin metal sheets. *Forensic Science International*, 102:121–132, 1999.
- [74] W.F. Noh. Errors for calculations of strong shocks using artificial viscosity and an artificial heat flux. *Journal of Computational Physics*, 72:78–120, 1978.
- [75] On Rope 1. Cinch 2 Inch, 2007. Product ID: DJ1400 <http://www.onrope1.com/store/index.php?p=product&id=149&parent=4>.
- [76] D. Palmieri. Simulation of shaped charge projectiles normal impact on the columbus advanced shields. Technical Report EWP-2173, European Space Agency, Noordwijk, The Netherlands, 2006.
- [77] B. Parga-landa and F. Hernandez-Olivares. An analytical model to predict impact behaviour of soft armours. *International Journal of Impact Engineering*, 16:455–466, 1995.

- [78] Y.K. Park and E.P. Fahrenthold. A kernel free particle finite-element method for hypervelocity impact simulation. *International Journal for Numerical Methods in Engineering*, 63:737–759, 2005.
- [79] Y.K. Park and E.P. Fahrenthold. Simulation of hypervelocity impact effects on reinforced carbon-carbon. *Journal of Spacecraft and Rockets*, 43:200–206, 2006.
- [80] J. Pepin. Fiber-reinforced structures for turbine engine rotor fragment containment. Technical Report DOT/FAA/AR-99/6, Office of Aviation Research, Washington, DC, September 1999.
- [81] J.M. Pereira and D.M. Revilock. Explicit finite element modeling of multilayer composite fabric for gas turbine engine containment systems part 2: Ballistic impact testing. Technical Report DOT/FAA/AR-04/40,P2, Office of Aviation Research, Washington, DC, November 2004.
- [82] D. Peric and S. Slijepcevic. Computational modelling of viscoplastic fluids based on a stabilised finite element method. *Engineering Computations*, 18:577–591, 2001.
- [83] S.L. Phoenix and P.K. Porwal. A new membrane model for the ballistic impact response and V50 performance of multi-ply fibrous systems. *International Journal of Solids and Structures*, 40:6723–6765, 2003.
- [84] Plastics International. Noryl PPO, 2007. <http://www.plasticsintl.com/datasheets/419943590Noryl.pdf>.

- [85] P.K. Porwal and S.L. Phoenix. Modeling system effects in ballistic impact into multi-layered fibrous materials for soft body armor. *International Journal of Fracture*, 135:217–249, 2005.
- [86] D.S. Pritchard. A study of a steel right circular cylinder (RCC) striking 23 plies of KM2 fabric using the LS-DYNA lagrangian hydrocode. Technical Report ARL-TR-2673, Army Research Lab, Aberdeen Proving Ground, MD, February 2002.
- [87] M.N. Raftenberg. Modeling thoracic blunt trauma towards a finite element based design methodology for body armor. Technical Report ADA433234, US Army Research Lab, Aberdeen Proving Ground, MD, December 2004.
- [88] M.N. Raftenberg and T.J. Mulkern. Quasi-static uniaxial tension characteristics of plain-woven Kevlar KM2 fabric. Technical Report ARL-TR-2891, Army Research Lab, Aberdeen Proving Ground, MD, December 2002.
- [89] M.N. Raftenberg, M.J. Scheidler, and P. Moy. Transverse compression response of a multi ply kevlar vest. Technical Report ARL-TR-3343, Army Research Lab, Aberdeen Proving Ground, MD, September 2004.
- [90] S. Rebouillat. Surface treated aramid fibers and a process for making them. U.S. Patent No. 5,520,705, May 1996. Assignee: E.I. Du Pont de Nemours and Company.

- [91] S. Rebouillat. Tribological properties of woven para-aramid fabrics and their constituent yarns. *Journal of Materials Science*, 33:3293–3301, 1998.
- [92] G.D. Roberts, D.M. Revilock, W.K. Binienda, W.Z. Nie, S.B. Mackenzie, and K.B. Todd. Impact testing and analysis of composites for aircraft engine fan cases. *Journal of Aerospace Engineering*, 15(3):104–110, July 2002.
- [93] T.V. Sagar, P. Potluri, and J.W. Hearle. Mesoscale modelling of interlaced fibre assemblies using energy method. *Computational Materials Science*, 28:49–62, 2003.
- [94] J. Sharda, C. Deenadayalu, B. Mobasher, and S.D. Rajan. Modeling of multilayer composite fabrics for gas turbine engine containment systems. *Journal of Aerospace Engineering*, 19(1):38–45, January 2006.
- [95] V.P. Shim, C.T. Lim, and K.J. Foo. Dynamic mechanical properties of fabric armour. *International Journal of Impact Engineering*, 25:1–15, 2001.
- [96] V.P. Shim, V.B. Tan, and T.E. Tay. Modelling deformation and damage characteristics of woven fabric under small projectile impact. *International Journal of Impact Engineering*, 16:585–605, 1995.
- [97] R. Shivarama and E.P. Fahrenthold. An ellipsoidal particle finite-element method for hypervelocity impact simulation. *International*

Journal for Numerical Methods in Engineering, 59:737–753, 2004.

- [98] R.A. Shivarama. *Hamiltons equations with Euler parameters for hybrid particle-finite element simulation of hypervelocity impact*. PhD thesis, University of Texas at Austin, Austin, TX, August 2002.
- [99] D.A. Shockey, D.C. Erlich, and J.W. Simons. Full scale tests of lightweight fragment barriers on commercial aircraft. Technical Report DOT/FAA/AR-99/71, Office of Aviation Research, Washington, DC, November 1999.
- [100] D.A. Shockey, D.C. Erlich, and J.W. Simons. Lightweight fragment barriers for commercial aircraft. In *18th International Symposium on Ballistics*, pages 1192–1199, November 1999.
- [101] D.A. Shockey, D.C. Erlich, and J.W. Simons. Improved barriers to turbine engine fragments: Interim report III. Technical Report DOT/FAA/AR-99/8,III, Office of Aviation Research, Washington, DC, May 2001.
- [102] D.A. Shockey, J.H. Giovanola, J.W. Simons, D.C. Erlich, R.W. Klopp, and S.R. Skaggs. Advanced armor technology: Application potential for engine fragment barriers for commercial aircraft. Technical Report DOT/FAA/AR-97/53, Office of Aviation Research, Washington, DC, September 1997.
- [103] S.A. Silling. *CTH Reference Manual: Johnson-Holmquist Ceramic Model*. Sandia National Laboratories, 1992. SAND92-0576.

- [104] M.A. Silva, C. Cisma-siu, and C.G. Chiorean. Numerical simulation of ballistic impact on composite laminates. *International Journal of Impact Engineering*, 31:289–306, 2005.
- [105] D.J. Steinberg. Equation of state and strength properties of selected materials. Technical Report UCRL-MA-106439, Lawrence Livermore National Laboratory, February 1996.
- [106] R.F. Stellingwerf and C.A. Wingate. Impact modeling with smooth particle hydrodynamics. *International Journal of Impact Engineering*, 14:707–718, 1993.
- [107] V. Tan, T. Tay, and W. Teo. Strengthening fabric armour with silica colloidal suspensions. *International Journal of Solids and Structures*, 42:1561–1576, 2005.
- [108] V.B. Tan and T.W. Ching. Computational simulation of fabric armour subjected to ballistic impacts. *International Journal of Impact Engineering*, 32:1737–1751, 2006.
- [109] V.B. Tan, V.P. Shim, and X. Zeng. Modelling crimp in woven fabrics subjected to ballistic impact. *International Journal of Impact Engineering*, 32:561–574, 2005.
- [110] Pure Tech. Material safety data sheet. MSDS Safety Information, March 1997. Brewster, New York.

- [111] U.S. Congress. Police body armor standards and testing: Vol i. Technical Report OTA-ISC-534, U.S. Congress, Office of Technology Assessment, Washington, DC: U.S. Government Printing Office, August 1992.
- [112] Y. Wang and Y.M. Xia. The effects of strain rate on the mechanical behaviour of kevlar fiber bundles an experimental and theoretical study. *Composites Part A*, 29A:1411–1415, 1998.
- [113] Y. Wang and Y.M. Xia. Experimental and theoretical study on the strain rate and temperature dependence of mechanical behaviour of kevlar fibre. *Composites Part A*, 30:1251–1257, 1999.
- [114] E.D. Wetzel, Y.S. Lee, R.G. Egres, K.M. Kirkwood, J.E. Kirkwood, and N.J. Wagner. The effect of rheological parameters on the ballistic properties of shear thickening fluid (STF)-kevlar composites. *Proceedings from Materials Processing and Design: Modeling, Simulation and Applications*, American Institute of Physics, 2004.
- [115] H.H. Yang. *Kevlar Aramid Fiber*. John Wiley and Sons, New York, NY, 1993.
- [116] H.H. Yang. *Comprehensive Composite Materials, Volume 1, Fiber Reinforcements and General Theory of Composites*, chapter 1.07 Aramid Fibers. Elsevier Science, New York, NY, 2000. 199-229.
- [117] X.S. Zeng, V.P. Shim, and V.B. Tan. Influence of boundary conditions

- on the ballistic performance of high-strength fabric targets. *International Journal of Impact Engineering*, 32:631–642, 2005.
- [118] X.S. Zeng, V.B. Tan, and V.P. Shim. Modelling interyarn friction in woven fabric armour. *International Journal for Numerical Methods in Engineering*, 66:1309–1330, 2006.
- [119] G. Zhou, X. Sun, and Y. Wang. Multi-chain digital element analysis in textile mechanics. *Composites Science and Technology*, 64:239–244, 2004.
- [120] T.I. Zohdi and D. Powell. Multiscale construction and large-scale simulation of structural fabric undergoing ballistic impact. *Computer Methods in Applied Mechanics and Engineering*, 195:94–109, 2006.
- [121] J.A. Zukas. *High Velocity Impact Dynamics*. John Wiley and Sons, Inc., New York, 1990.
- [122] J.A. Zukas. *Introduction to Hydrocodes*, volume 49 of *Studies in Applied Mechanics*. Elsevier, Amsterdam, 2004.

Vita

Robert James Rabb was born on 8 September 1966, the son of Donald and Tram Rabb. He graduated from Caprock High School in Amarillo, Texas in 1984. He pursued his undergraduate education at the United States Military Academy where he received a Bachelor's of Science degree in Mechanical Engineering and was commissioned as an engineer officer in the United States Army in 1988. He was stationed in Colorado Springs, Colorado, and Germany. Upon returning from Germany, he attended the University of Texas at Austin and earned a Master of Science in Mechanical Engineering in 1998. He taught Mechanical Engineering to cadets at the United States Military Academy and was subsequently stationed at Leavenworth, Kansas, and in Missouri where he obtained his Professional Engineer License. In August 2004, he reentered the Graduate School of the University of Texas at Austin on the Army's Advanced Civil Schooling program. He is currently a Lieutenant Colonel in the United States Army.

Permanent address: 8A Thayer Road
West Point, New York 10997

This dissertation was typeset with L^AT_EX[†] by the author.

[†]L^AT_EX is a document preparation system developed by Leslie Lamport as a special version of Donald Knuth's T_EX Program.